SYNTHESIS AND APPLICATIONS OF TWO-DIMENSIONAL ZEOLITES TO CATALYSIS AND MEMBRANE SEPARATIONS

A Dissertation
Presented to
The Academic Faculty

by

Akshay Korde

In Partial Fulfillment
of the Requirements for the Degree
Doctor of Philosophy in the
School of Chemical and Biomolecular Engineering

Georgia Institute of Technology
August 2020

SYNTHESIS AND APPLICATIONS OF TWO-DIMENSIONAL ZEOLITES TO CATALYSIS AND MEMBRANE SEPARATIONS

Approved by:

Dr. Christopher W. Jones, Advisor
School of Chemical and Biomolecular Engineering
Georgia Institute of Technology

Dr. Sankar Nair, Co-Advisor
School of Chemical and Biomolecular Engineering
Georgia Institute of Technology

Dr. Ryan P. Lively
School of Chemical and Biomolecular Engineering
Georgia Institute of Technology

Dr. Nian Liu
School of Chemical and Biomolecular Engineering
Georgia Institute of Technology

Dr. Angus J. Wilkinson
School of Chemistry and Biochemistry
Georgia Institute of Technology

Date Approved: April 30, 2020

To my parents

ACKNOWLEDGEMENTS

As my PhD comes to an end, I cannot help but realize that a big part of my graduate school experience would not be possible without the help and support of people around me. Firstly, I would like to thank my advisors, Dr. Christopher W. Jones and Dr. Sankar Nair. In all honesty, words are not enough to convey my gratitude to them. Throughout my PhD, they have shown a lot of faith in me and have always encouraged me to explore my ideas with complete freedom. They have been my hardest critiques as well as my biggest champions and this has pushed me to do my best. My awe of their intelligence, scientific acumen, dedication to work and communication skills has continued to grow over the years. Through their patient guidance, I've learnt vital lessons in conducting creative research, being rigorous in my work and communicating it in a clear way. They have played a pivotal role in shaping me as a researcher and as a professional. It has been a privilege to work under their guidance.

I would also like to thank my thesis committee – Dr. Ryan P. Lively, Dr. Nian Liu and Dr. Angus J. Wilkinson, for their valuable inputs and comments on my work. My collaborators at Georgia Tech – Byunghyun Min and Omar Knio, at Penn State – Dr. Xueyi Zhang and Xinyang Yin and at Stockholm University – Elina Kapaca, Dr. Tom Willhammar and Dr. Xiaodong Zou – have been indispensable in solving the structure of the zeolite nanotubes (Chapter 4) and I am indebted to them for their time and expertise.

The privilege of being a part of two research groups meant that I was in the company of several excellent researchers. Both, the Jones and the Nair groups, have among the best and brightest students, and intellectual discussions with them as well their feedback

and suggestions are acknowledged. In the Jones group, I would like to thank all the past and present members, including and not limited to – Dr. Simon Pang, Dr. Michele Sarazen, Dr. Li-Chen Lee, Dr. Hyuk Taek Kwon, Dr. Caroline Hoyt, Dr. Shilpa Mahamulkar, Dr. Kristina Golub, Dr. Taylor Sulmonetti, Dr. Chunjae Yoo, Dr. Lalit Darunte, Dr. Nathan Ellebracht, Dr. Jason Lee, Dr. Achintya Sujan, Dr. Dharam Raj Kumar, Dr. Cornelia Rosu, Dr. Qandeel Almas, Dr. Claudia Okonkwo, Byunghyun Min, Sangjae Park, Nima Ronaghi, Jacob Cleveland and Maxim Bukhovko. In the Nair group, I would like to thank Dr. Wun-gwi Kim, Dr. Kiwon Eum, Dr. Yadong Chiang, Dr. Shaowei Yang, Dr. Souryadeep Bhattacharyya, Dr. Krishna Jayachandrababu, Dr. Yeonhye Kwon, Dr. Chen Ma, Zhongzhen Wang, Wanwen Liang, Arvind Ganesan and Qiang Fu. All the members in both, the Jones group and the Nair group, have been extremely helpful and I got to learn a lot from each of them. Dr. Wun-gwi Kim was the first person who taught me to synthesize zeolites and that has formed the foundation of my thesis work. Byunghyun Min, my collaborator, and the best zeolite membrane scientist I know of, has been a source of tremendous support, knowledge and expertise for my work. His work ethic and ability to crank out results is something I really aspire to learn. He has been ever ready to help me with my problems, and this thesis would not be what it is without his input. Dr. Lalit Darunte, by virtue of being my roommate during the initial years, had the added responsibility of acting as my mentor – something that I will forever be indebted to him for. I'll also cherish discussing science and bouncing off ideas with Dr. Chunjae Yoo, Dr. Nathan Ellebracht, Nima Ronaghi and Jacob Cleveland. I was also fortunate to have a smart and hardworking undergrad like Thomas (Ziyuan) Wang working alongside and helping out with my research. The group lunches and coffee breaks were fun times that helped me

to unwind and relax. I have thoroughly enjoyed my time working in these research groups. I leave with a heavy heart and a ton of beautiful memories.

My five years in Atlanta would have been half as fun if not for the ChBE Indian gang. The numerous dinners, movies, birthday celebrations and board game nights have helped me enjoy my time and given me something to look forward to on weekends. For this and more, I am deeply indebted to Dr. Lalit Darunte, Dr. Pradnya Samant, Dr. Jaya Arya, Dr. Rohan Awati, Dr. Sireesha Aluri, Dr. Mayank Agrawal, Dr. Qandeel Almas, Dr. Achintya Sujan, Trisha Sen, Simple Kumar, Gamze Eris, Nikhil Raj, Arvind Ganesan, Udita Ringania, Pavithra Narayanan, Geetanjali Pendyala, Kavita Matange, Shivesh Choudhary, Dhrumil Shah, Jagriti Sahoo, Shubham Jamdade Roshan Shetty and Vaibhav Joshi. Road trips and vacations with Trisha Sen and Simple Kumar will be fondly remembered. I especially want to thank Trisha Sen for standing by me always, supporting me and providing stability in my life.

Finally, I would like to thank my parents for giving me this opportunity to come to Georgia Tech and complete my PhD. They have supported all my endeavors, even when it meant that they would have to stay alone and away from their only son, while he pursued his dreams of a PhD. They have sacrificed a lot of their own happiness, so that I could pursue mine. I am eternally grateful for their unconditional love and everything that they have done for me. It is really my parents, who deserve the success of this PhD.

TABLE OF CONTENTS

LIST OF TABLES

LIST OF FIGURES

SUMMARY

Zeolites have proven themselves as attractive materials for catalysis and separation applications due to their ordered microporous structure and presence of strong acid sites. These materials can crystallize in several topologies and compositions that can be used to tune their properties to suit a particular application. However, due to their microporous nature, these materials impose mass transfer limitations, especially on large molecules, that reduce their catalytic activity. Two-dimensional zeolite nanosheets with single unit-cell thickness and high aspect ratio help to overcome this limitation by reducing the diffusion path length and increasing the external surface area that provides better access to catalytic sites in when using large molecules. These nanosheets can also be exfoliated and processed into highly oriented, ultra-thin membranes that can retain the molecular sieving ability of the corresponding bulk 3D zeolite. However, only 10 or so frameworks have been synthesized so far in the 2D morphology and even for the existing 2D zeolite nanosheets, the structure-property relationships have not been fully studied. The work described here aims to develop structure-property relationships for some of the existing zeolite nanosheets by using them in catalytic and membrane separation applications while developing generalized synthesis methodologies to expand the library of zeolites crystallized with a single unit-cell thickness.

The first objective of the thesis was to study the effect of Si/Al ratio on the catalytic activity of 2D MFI nanosheets. The nanosheets with varying Si/Al ratios were characterized in detail and their catalytic performance was compared using the liquid phase Friedel-Crafts alkylation of mesitylene with benzyl alcohol & the self-etherification of

benzyl alcohol that occurs in parallel, both of which are catalyzed by Brønsted acid sites. The turnover frequency (TOF) of the catalysts is found to decrease with decreasing Si/Al ratio, with the etherification reaction being the main contributor to this trend. When the same reaction is carried out in the presence of a bulky poison, 2,6 di-*tert*-butylpyridine (DTBP), to selectively deactivate the external acid sites, only the etherification reaction of benzyl alcohol takes place in the micropores of the 2D MFI catalyst and the effectiveness factor is found to decrease with decreasing Si/Al ratio. Thus, increasing the density of acid sites in the micropores by decreasing the Si/Al ratio makes it more difficult for the reactant molecules to access them, as demonstrated by the decrease in TOF and the effectiveness factor.

In the next objective, exfoliated AEL nanosheets, with one-dimensional pores running through the plane of the nanosheets, were used to form an intermediate layer on the shell side of α-alumina hollow fiber for forming a poly(amide) (PA) film via interfacial polymerization (IP) between a diamine in an aqueous phase and an acid chloride in an organic phase. PA membranes have been widely used for the desalination of brackish water and seawater. The thin AEL molecular sieve nanosheet layer likely acts as a reservoir to store the diamine molecules, while allowing for its controlled release during the IP reaction. The composite AEL nanosheet-poly(amide) membrane exhibited a high water flux and NaCl rejection as well as displayed long-term stability in pervaporative desalination.

Lastly, new organic structure directing agents (OSDAs) were synthesized and screened to crystallize new zeolites with single unit-cell crystal thickness in a one-pot, bottom-up manner. This has resulted in the crystallization of a novel microporous zeolitic nanotube, using a bolaform OSDA with a biphenyl group in the hydrophobic center and

hydrophilic quinuclidinium groups at the ends, separated by a C_{10} carbon chain. The growth mechanism of the nanotubes was studied through time-resolved crystallization of the material that revealed the formation of a mesostructure very early on in the synthesis due to the micellar assembly of the OSDA. The SDA most likely forms a cylindrical or rod-like micellar assembly, with the biphenyl groups of the SDA molecules interacting with each through π-π interactions, while the quinuclidinum groups direct the crystallization of the microporous zeolitic walls of the nanotube.

In summary, this thesis will help to advance the field of separations and catalysis by uncovering structure property relations of existing 2D zeolites while developing a new zeolite morphology. All these materials may be advantageous over their conventional 3D zeolite counterparts.

CHAPTER 1. INTRODUCTION

1.1 Zeolites and their Applications

Zeolites are ordered microporous crystalline materials with recurring TO_4 tetrahedral units, where T is either Si or Al and adjacent tetrahedral units are connected by oxygen atoms.[1,2] Zeolites were originally discovered as naturally occurring minerals by the Swedish mineralogist Cronstedt in 1756. The first synthetic zeolite was made almost 200 years later by Barrer[3] in 1948 using a hydrothermal synthesis method that is now the conventional means of synthesizing these materials. Zeolites can crystallize in various frameworks having pores of different sizes and connectivity, and as such, they are also referred to as 'molecular sieves'. The International Zeolite Association (IZA) has recognized 248 unique frameworks that have been synthesized.[4] In addition, there are over 2.7 million hypothetical zeolite framework structures that have been predicted theoretically.[5]

While the name 'zeolite' is used in the strict sense for only aluminosilicate materials, molecular sieves with T atoms other than silicon and aluminum have also been synthesized by hydrothermal synthesis. Many times these are also referred to as zeolites. The inclusion of heteroatoms such as boron and germanium has also allowed synthesis of several frameworks that could not be synthesized as aluminosilicates.[6,7] Aluminophosphates are a similar class of molecular sieves that are comprised of alternating AlO_2^- and PO_2^+ tetrahedra, leading to a charge neutral framework.[1,8] This variety in the structure and composition of zeolites and zeolite-like molecular sieves endows them with properties favorable for applications such as catalysis, ion exchange and separations.

Zeolites are widely used in the petrochemical industry as catalysts because of the presence of strong acid sites and the shape selectivity imparted by the ordered porous structure.[9] Catalytic cracking, [10] alkylation[11] and isomerization[12] are some of the important categories of reactions catalyzed by zeolites on an industrial scale. Due to recent increase in the demand for sustainable chemicals, zeolites have also received significant attention in the catalytic conversion of biomass derived species.[13] The molecular sieving ability imparted by the pore structure of zeolites also makes them useful for separation applications that are often achieved by fabricating zeolites into membranes. Zeolite membranes generally separate molecules based on their size, with smaller molecules permeating faster than larger ones,[14] and have been shown to be effective in several separations of industrial importance such as H_2/CO_2,[15] linear/branched isomers,[16] xylene separations[17] etc.

While zeolites and other molecular sieves have several potential applications, they also possess certain limitations. Their microporous structure excludes large/bulky molecules from the internal surface of the zeolite. Thus, in the case of catalytic applications, such molecules can only be converted on the external surface of the zeolite and this leads to a reduction in the catalytic activity since a small fraction of active sites are exposed on the external surface.[18] This demands an increase in the accessible surface area of zeolites so that bulky molecules can be catalytically converted as well.

1.2 Hierarchical Zeolites

One method to provide a larger accessible surface area in zeolites is to introduce mesopores. Zeolitic materials possessing both micropores and mesopores are referred to as

hierarchical zeolites, as shown in Figure 1.1. The presence of mesopores reduces the steric limitations for diffusion of bulky molecules and improves the intracrystalline diffusion in general. The faster diffusion to and from the catalytic centers also helps to avoid secondary reactions and coke formation, although some reduction in shape-selective effects is often observed.[19] Hierarchical zeolites are often synthesized by introducing mesopores in conventional zeolites through processes such as dealumination[20] or desilication.[21] However, these processes lead to the loss of framework atoms, thus reducing the mass of the zeolite and offering little control over the composition of the resulting material. Other methods such as dual templating using surfactants and hard-templating using polymeric spheres are also known to yield hierarchical zeolites.[19] Irrespective of the method used for their synthesis, hierarchical zeolites have generally shown higher activity in catalytic conversions of bulky reactants and longer catalyst lifetimes.[22]

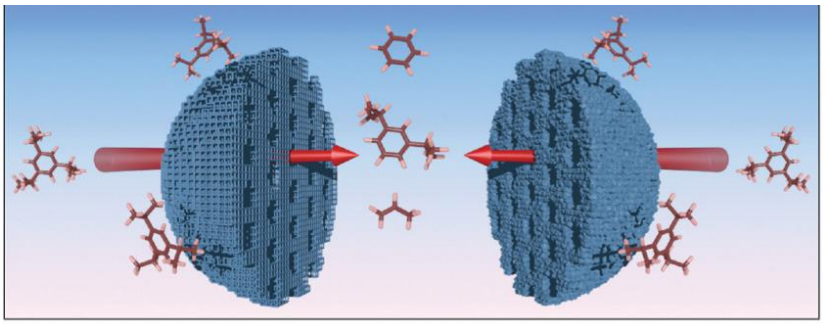

Figure 1.1. Secondary mesopore system to facilitate access to active sites[18]

1.3 Zeolite Nanosheets

Another method to reduce the diffusion path length and increase the external surface area is to reduce the size of the zeolite crystals.[23] Several researchers have successfully synthesized zeolite frameworks as nanocrystals.[24] The higher external surface area

translates to a larger number of active sites accessible to bulky reactant molecules. Notably, Corma et al.[25] were able to synthesize a material with MWW topology that could be exfoliated as single unit-cell thick layers via post-synthetic treatments. This resulted in 2.5 nm thick MWW nanosheets that displayed higher catalytic activity and selectivity towards desired products in the catalytic cracking of large molecules. However, this top-down approach has only been shown to be effective in the case of a few zeolites that have layered precursors.[26,27]

In 2009, Ryoo et al.[28] synthesized single unit cell thick MFI nanosheets with 2 nm thickness along the b-axis in a one-pot synthesis using an appropriately designed organic structure directing agent (OSDA). The OSDA ($C_{22\text{-}6\text{-}6}$) was a diquaternary ammonium surfactant with a long alkyl chain that formed a lamellar micellar assembly in solution. The ammonium groups, separated by a C6 alkyl linkage, acted as effective structure-directing agents for the MFI structure and the hydrophobic tail restricted the growth of the zeolite along the *b*-direction, as shown in Figure 1.2. The resulting sheet-like morphology led to a very high external surface area with a large fraction of active sites exposed on the surface. These MFI nanosheets showed higher catalytic activity as compared to conventional MFI in the conversion of large organic molecules owing to the large number of acid sites on the external surface, while the single unit-cell thickness facilitated faster diffusion and reduced coke deposition, as shown for the methanol to gasoline conversion.

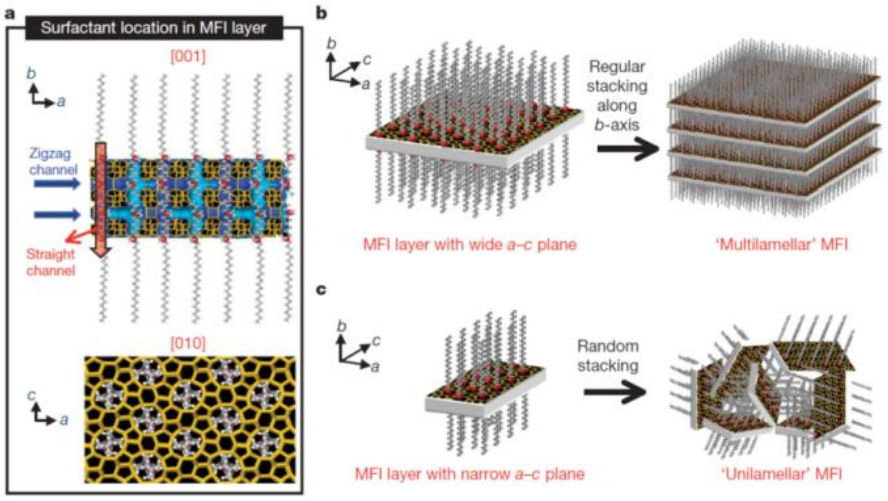

Figure 1.2. Proposed mechanism of crystallization of MFI nanosheets using the C22-6-6 OSDA synthesized by Ryoo et al. [28]

Clearly, the OSDA is the most critical aspect to ensure the crystallization of the zeolite in a nanosheet morphology. Building on the OSDA structure reported by Ryoo et al.,[28] Park et al.[29] synthesized several OSDAs with a long alkyl chain and varied the number of ammonium moieties as well as varied spacer length between them. They found that a minimum of 2 ammonium moieties was required for the crystallization of MFI nanosheets and as the number increased, the thickness of the nanosheets increased, while a minimum spacer length of 3 carbons was needed between them to avoid degradation of the OSDA. A long enough alkyl chain is also needed to impart hydrophobicity and the overall amphiphilic nature of the molecule is then capable of directing MFI nanosheets. Based on these findings, Luo et al.[30] designed a special OSDA by modifying tetramethyladamantammonium hydroxide (TMAdOH) that is commonly used in conventional MWW synthesis, and successfully synthesized MIT-1, a material with MWW framework and having nanosheet morphology, in a bottom-up manner. The OSDA, shown in Figure 1.3, had a sufficiently long alkyl chain (C_{16}) to restrict the growth of the MWW

framework in the third dimension and two ammonium moieties spaced by 4 or more carbons. The adamantane headgroup of the OSDA acted as an effective structure directing agent to crystallize the MWW framework while the long hydrophobic carbon chain effectively retarded the crystal growth along the third dimension.

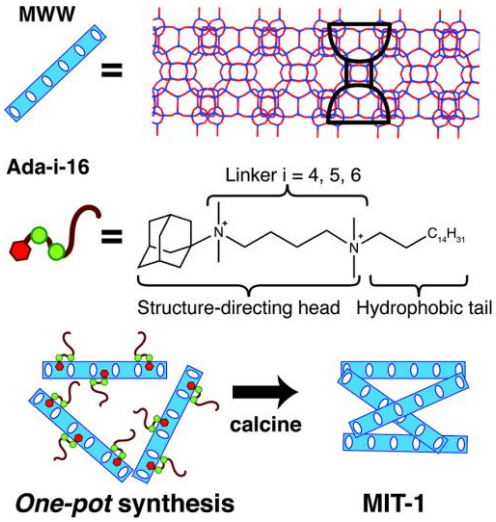

Figure 1.3. Schematic representation of the OSDA and structure of MIT-1[30]

The ability of the OSDA to form a lamellar micellar assembly is critical to the crystallization of multilamellar zeolitic nanosheets. Che et al.[31] were able to synthesize amphiphilic OSDAs with aromatic rings in their hydrophobic part, that could self-assemble through π-stacking of the aromatic rings. The hydrophilic quaternary ammonium groups were able to direct the crystallization of the microporous structure of MFI, while the highly stable hydrophobic layer formed by the aromatic rings was effective in retarding the crystal growth and restricting the zeolite crystals to a nanosheet morphology. Several such molecules were synthesized, and these molecules were able to successfully direct the MFI framework with different mesoporous networks. These works have been reviewed in detail

by Che et al.[32] Thus, there are multiple strategies that can be employed in the crystallization of single-unit cell thick zeolite crystals.

MFI nanosheets especially have received significant attention in catalysis applications. In parallel, they have also been fabricated as ultra-thin membranes that have shown superior performance for butane and xylene isomer separations. Other than MFI, there are very few frameworks reported in the nanosheet morphology, including MWW,[30] *MRE,[33] MTW,[33] *BEA,[33] AFI,[34] ATO[34] and AEL[34]. These zeolite nanosheets have a very high external surface area that ensures a large number of active sites are exposed on the surface. This makes the catalytic centers more accessible and reduces intracrystalline diffusion limitations, which ultimately manifests as a higher reaction rate. Their single unit-cell crystal thickness also helps in the fabrication of ultra-thin membranes for separation applications. Some important details regarding the applications of these 2D zeolite nanosheets are discussed in the following sub-sections.

1.3.1 Catalytic Applications of Zeolite Nanosheets

MFI nanosheets have been shown to increase the rate of catalytic conversion in several reactions as compared to conventional MFI, especially in the case of large reactant molecules, as demonstrated through several test reactions.[28,35] Kim et al.[36] synthesized MFI nanosheets using a seed-assisted method and this catalyst had high activity in the Pechmann condensation of bulky reactants as depicted in Figure 1.4. Luo et al.[30] synthesized MWW nanosheets in a one-pot synthesis and showed high conversion of benzyl alcohol in the Friedel-Crafts alkylation of benzene with benzyl alcohol. SAPO nanosheets with ATO topology synthesized by Seo et al.[34] had high catalytic activity and selectivity towards

branched isomers in the hydroisomerization of *n*-heptane, as well as a reduced rate of catalyst deactivation.

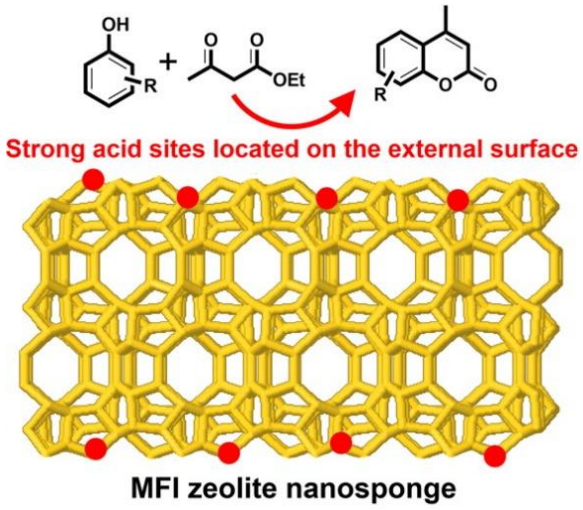

Figure 1.4. Converson of bulky reactants on the external acid sites of MFI nanosponge[36]

MFI nanosheets with other metal atoms included in the framework have also been shown to act as efficient catalysts. Na et al.[37] synthesized MFI nanosheets with Ti atoms isomorphously substituted in the framework. These titanosilicate nanosheets showed high catalytic activity and selectivity in the epoxidation of small as well as bulky olefins. Ren et al.[38] incorporated Sn atoms in the MFI framework and the resulting nanosheets displayed high yields in the conversion of glucose to fructose and lactose to lactulose. Impregnating Pt nanoparticles transformed the MFI nanosheets into bifunctional catalysts that were used for the hydroisomerization of *n*-heptane[39] and *n*-decane.[40] These bifunctional catalysts displayed high selectivity to branched isomers and reduced cracking that was attributed to the short diffusion path. However, the short diffusion path also leads to loss of diffusion selectivity, as in the case of ethylbenzene hydroisomerization where zeolite nanosheets

showed lower selectivity to *p*-xylene but higher activity as compared to conventional zeolites.[33]

1.3.2 Membrane Fabrication using Zeolite Nanosheets

The deployment of conventional zeolite membranes at the industrial scale is mainly inhibited by their high cost of fabrication. One of the ways to circumvent this issue of high cost is to fabricate zeolite membranes that have a higher throughput while maintaining the separation factor at a desired level. This can be achieved by fabricating highly oriented, ultra-thin membranes, which can result in high flux. To achieve these qualities in a zeolite membrane, Varoon et al.[41,42] exfoliated the as-synthesized multilamellar stack of MFI nanosheets using a polymer melt compounding technique. The nanosheet suspension was then vacuum filtered over a suitable porous support, thus depositing the nanosheets in an oriented fashion with the *b*-direction pointing out of the plane of the support due to their high aspect ratio. Secondary growth *via* a mild solvothermal treatment reduced the non-selective gaps between the sheets and the resultant membranes were around 100 nm thick. These ultra-thin membranes displayed high selectivity and permeances for industrially relevant separations such as xylene and butane isomers. Later, Zhang et al.[43] demonstrated a similar fabrication process on polymer substrates and activating the zeolite nanosheets by treating with piranha solution, which may make them applicable for use on an industrial scale. The exfoliation process of the MFI nanosheets is depicted in Figure 1.5. However, without a secondary growth, the membrane had some non-selective pathways that resulted in a reduced selectivity in the case of butane isomers. Jeon et al.[44] fabricated MFI membranes using directly synthesized MFI nanosheets that did not need any exfoliation. While most of the works mentioned so far used a disk type support for fabricating the MFI

membrane, Min et al.[45] extended this methodology to using scalable α-alumina hollow fiber supports to enable potential application at an industrial scale. Membrane separations using zeolite nanosheets have only been demonstrated for MFI nanosheets so far because of the favorable pore structure of MFI and the dearth of other useful frameworks synthesized in the nanosheet morphology.

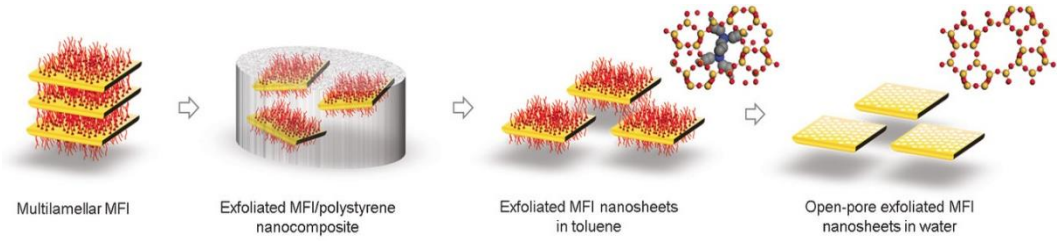

Figure 1.5. Exfoliation process of multilamellar MFI nanosheets[43]

1.4 Thesis Objectives

Two dimensional zeolitic materials with nanosheet morphology have been shown to possess several advantages over conventional zeolites for both catalysis and separation applications, as described in the previous sections. However, only a few zeolitic frameworks have been synthesized in the 2D nanosheet morphology. There exists no generalizable methodology for successfully synthesizing other zeolite frameworks in the two-dimensional form. Even for the existing 8 or so zeolite frameworks accessible as nanosheets, the structure-property relationships are not well understood. Given the context of the foregoing discussion, the overall goals of this thesis work are twofold: (1) Develop the structure-property relationships for existing 2D zeolites with medium-sized (10 membered-ring, 10 MR) pores – specifically MFI and AEL structure types – in the form of catalysts and membranes (2) Extend the synthesis concepts of 2D zeolitic materials,

potentially to further lower-dimension materials, through the design and synthesis of new organic structure-directing agents (OSDAs) and their use in zeolite synthesis reactions. These overall goals are broken down into three objectives, which form the subsequent chapters of this thesis. A brief description and rationale of the specific objectives is outlined in the following subsections.

1.4.1 Effect of Si/Al Ratio on the Catalytic Activity of MFI nanosheets

The Si/Al ratio of zeolites directly impacts their acid site density and has also been shown to impact their catalytic performance in terms of activity and selectivity.[46–48] There is also ample evidence that irrespective of the morphology of the catalyst, the activity per acid site typically reduces with increasing acid site density or equivalently with decreasing Si/Al ratio of the catalyst.[36,49,50] However, this decreasing activity with decreasing Si/Al ratio has not been verified for 2D MFI nanosheets, nor have the reasons for this trend been fully elucidated. For the 2D MFI nanosheets, it is also important to probe the external and internal (located in the micropores) acid sites separately, since there is a significant proportion of external acid sites in the nanosheets. This helps to decouple their activities. These were the main objectives of the work presented in Chapter 2.

MFI nanosheets with varying Si/Al ratio were synthesized via careful control of synthesis conditions and characterized in detail. An appropriate reaction – the Friedel-Crafts alkylation of mesitylene with benzyl alcohol – that allows the deconvolution of the activities of the external and internal acid sites was chosen in this study. The external acid sites could be deactivated by adding 2,6-di-*tert*-butylpyridine and this allows to probe the activity of the internal acid sites selectively. This allowed the analysis of the internal mass

transfer limitations in the micropores of the 2D MFI nanosheet by analyzing the Thiele modulus under different reactions conditions. On the whole, this chapter provides important insights into the Si/Al ratio as a design parameter for 2D MFI catalyst.

1.4.2 AEL nananosheet/Polyamide composite membranes for desalination

As mentioned in section 1.3.2, membranes fabricated using zeolite nanosheets could potentially offset the high cost of these membranes based on their high flux, while maintaining selectivity. Similar to MFI nanosheets, Seo et al.[34] reported the synthesis of three different frameworks (AEL, AFI and ATO) of 2D aluminophosphate nanosheets using specially designed multi-amine OSDAs with long alkyl chains. All frameworks synthesized by these researchers have a one-dimensional pore system running perpendicular to the plane of the nanosheets, with AEL having 10 MRs and AFI and ATO having 12 MRs. Of these frameworks, AEL has an elliptical pore that is 4 Å x 6.5 Å in size and this could make it especially attractive for molecular sieving applications, while the thin crystal thickness can allow for faster diffusion of small molecules. These properties make it particularly interesting to study membranes containing AEL nanosheets.

While a purely zeolitic AEL membrane can be applied to several molecular-sieving applications, zeolite-polymer hybrid membranes could have potentially interesting applications as well. Poly(amide)-based membranes fabricated using interfacial polymerization between a diamine and an acid chloride are of particular interest because of their applicability to desalination of water, even at an industrial scale.[51,52] Another advantage of these poly(amide) membranes is that they can incorporate microporous fillers as well, which help to enhance the flux of these membranes while maintaining high salt

rejections.[53–55] Recently, poly(amide)-based membranes have also been fabricated on microporous α-alumina hollow fiber supports, and this helps to improve the scalability of these membranes while also making them more robust to harsh temperature and pressure conditions.[56–58] This requires a smoothing layer to be applied on surface of the bare alumina hollow fiber to improve the interaction between the support and the polymer film. The use of such a smoothing layer, in the form of porous materials, on polymeric as well as alumina supports, has yielded tremendous improvement in the permeance of the poly(amide) membranes because of the ability of these layers to act as a reservoir for the diamine molecules and enable their controlled release during the interfacial polymerization reaction.[59–62]

Given this background, the aim of the work presented in chapter 3 is to fabricate a AEL nanosheet/poly(amide) composite membrane on the outer surface (shell side) of α-alumina hollow fibers as a support. The ceramic hollow fibers were chosen as the support because of their scalability, high packing density and low cost of production. The exfoliation of multilamellar AEL nanosheets was carried out in a manner similar to that of MFI nanosheets.[41] These exfoliated nanosheets were then deposited on the shell side of the alumina hollow fibers, creating a smooth surface for the poly(amide) film formation and acting as a storage layer for the diamine. The resultant AEL nanosheet/poly(amide) composite membrane was then tested for the pervaporative desalination of water.

1.4.3 Synthesis of one-dimensional microporous zeolitic material

It is very clear at this point that zeolites with single unit-cell crystal thickness have pushed the boundaries of the performance of zeolites in both catalysis and membrane

separation applications. However, the complex hydrothermal synthesis of zeolites makes it difficult to predict the influence of the several variables involved and this is especially true for zeolites with single unit-cell crystal thickness because of the micellar assembly that the OSDA needs to form to guide the crystallization. Additionally, so far, only 2D zeolite nanosheets with single unit-cell crystal thickness have been reported and this has not been extended to the synthesis of further, lower dimensional materials.

Che et al.[63] have reported the crystallization of a single unit-cell thick MFI crystal with a pillared structure and having square mesopores. This was achieved through the cylindrical micellar assembly that the OSDA was able to form. The OSDA had aromatic groups with long carbon chains forming the hydrophobic tail and quaternary ammonium groups forming hydrophilic heads. The OSDA could form this cylindrical micellar assembly due to the strong π-π interactions between the aromatic rings. Combining this strategy of π-stacking with the use of suitable quaternary ammonium headgroups as reported by Luo et al.,[30] we synthesized a new OSDA with aromatic rings in the hydrophobic core and quinuclidine groups as the hydrophilic headgroups. This OSDA was able to form a micellar assembly that was able to direct the crystallization of a 1D microporous aluminosilicate nanotube. The details of this work, which has produced an unprecedented structure in zeolite science, are discussed in Chapter 4.

1.5 References

(1) Auerbach, M. S.; Carrado, K. A.; Dutta, P. K. *Handbook of Zeolite Science and Technology*; New York, 2003.

(2) Cundy, C. S.; Cox, P. A. The Hydrothermal Synthesis of Zeolites: History and Development from the Earliest Days to the Present Time. *Chem. Rev.* **2003**, *103* (3), 663–701.

(3) Barrer, R. M. Synthesis of a Zeolitic Mineral with Chabazite-like Sorptive Properties. *J. Chem. Soc.* **1948**, No. 0, 127–132.

(4) http://www.iza-structure.org/databases/.

(5) Deem, M. W.; Pophale, R.; Cheeseman, P. A.; Earl, D. J. Computational Discovery of New Zeolite-like Materials. *J. Phys. Chem. C* **2009**, *113* (51), 21353–21360.

(6) Paillaud, J.-L.; Harbuzaru, B.; Patarin, J.; Bats, N. Extra-Large-Pore Zeolites with Two-Dimensional Channels Formed by 14 and 12 Rings. *Science (80-.).* **2004**, *304* (5673), 990–992.

(7) Elomari, S.; Burton, A.; Medrud, R. C.; Grosse-Kunstleve, R. The Synthesis, Characterization, and Structure Solution of SSZ-56: An Extreme Example of Isomer Specificity in the Structure Direction of Zeolites. *Microporous Mesoporous Mater.* **2009**, *118* (1–3), 325–333.

(8) Davis, M. E.; Lobo, R. F. Zeolite and Molecular Sieve Synthesis. *Chem. Mater.* **1992**, *4* (4), 756–768.

(9) Abate, S.; Barbera, K.; Centi, G.; Lanzafame, P.; Perathoner, S. Disruptive Catalysis by Zeolites. *Catal. Sci. Technol.* **2016**, *6*, 2485–2501.

(10) Venuto, P. B.; Habib, E. T. J. *Fluid Catalytic Cracking with Zeolite Catalysts*; Marcel Dekker, Inc.: New York, 1979.

(11) Venuto, P.B., Hamilton, A., Landis, P.S. and Wise, J. J. Organic Reactions Catalyzed by Crystalline Aluminosilicates I. Alkylation Reactions. *J. Catal.* **1966**, *4*, 81–98.

(12) Skeels, G. W.; Flanigen, E. M. Normal Paraffin Hydrocarbon Isomerization Process Using Activated Zeolite Beta. 5,095,169, 1992.

(13) Ennaert, T.; Van Aelst, J.; Dijkmans, J.; De Clercq, R.; Schutyser, W.; Dusselier, M.; Verboekend, D.; Sels, B. F. Potential and Challenges of Zeolite Chemistry in the Catalytic Conversion of Biomass. *Chem. Soc. Rev.* **2016**, *45* (3), 584–611.

(14) Kosinov, N.; Gascon, J.; Kapteijn, F.; Hensen, E. J. M. Recent Developments in Zeolite Membranes for Gas Separation. *J. Memb. Sci.* **2016**, *499*, 65–79.

(15) Korelskiy, D.; Ye, P.; Fouladvand, S.; Karimi, S.; Sjöberg, E.; Hedlund, J. Efficient Ceramic Zeolite Membranes for CO 2 /H 2 Separation. *J. Mater. Chem. A* **2015**, *3* (23), 12500–12506.

(16) Bayati, B.; Belbasi, Z.; Ejtemaei, M.; Charchi Aghdam, N.; Babaluo, A. A.; Haghighi, M.; Drioli, E. Separation of Pentane Isomers Using MFI Zeolite Membrane. *Sep. Purif. Technol.* **2013**, *106*, 56–62.

(17) Yuan, W.; Lin, Y. S.; Yang, W. Molecular Sieving MFI-Type Zeolite Membranes for Pervaporation Separation of Xylene Isomers. *J. Am. Chem. Soc.* **2004**, *126* (15), 4776–4777.

(18) Mo, K.; Bein, T. Mesoporosity - a New Dimension for Zeolites. *Chem. Soc. Rev.* **2013**, *42*, 3689–3707.

(19) Serrano, D. P.; Escola, J. M.; Pizarro, P. Synthesis Strategies in the Search for Hierarchical Zeolites. *Chem. Soc. Rev.* **2013**, *42* (9), 4004–4035.

(20) Beyerlein, R. A.; Choi-feng, C.; Hall, J. B.; Huggins, B. J.; Ray, G. J. Effect of Steaming on the Defect Structure and Acid Catalysis of Protonated Zeolites. *Top. Catal.* **1997**, *4*, 27–42.

(21) Ogura, M.; Shinomiya, S.; Tateno, J.; Nara, Y.; Kikuchi, E.; Matsukata, M. Formation of Uniform Mesopores in ZSM-5 Zeolite through Treatment in Alkaline Solution. *Chem. Lett.* **2000**, No. 8, 882–883.

(22) Holm, M. S.; Taarning, E.; Egeblad, K.; Christensen, C. H. Catalysis with Hierarchical Zeolites. *Catal. Today* **2011**, *168* (1), 3–16.

(23) Gobin, O. C.; Reitmeier, S. J.; Jentys, A.; Lercher, J. A. Comparison of the Transport of Aromatic Compounds in Small and Large MFI Particles. *J. Phys. Chem. C* **2009**, *113* (47), 20435–20444.

(24) Tosheva, L.; Valtchev, V. P. Nanozeolites: Synthesis, Crystallization Mechanism, and Applications. *Chem. Mater.* **2005**, *17* (10), 2494–2513.

(25) Corma, A.; Fornes, V.; Pergher, S. B.; Maesen, T. L. M.; Buglass, J. G. Delaminated Zeolite Precursors as Selective Acidic Catalysts. *Nature* **1998**, *396* (November), 353–356.

(26) Díaz, U.; Corma, A. Layered Zeolitic Materials: An Approach to Designing Versatile Functional Solids. *Dalton Trans.* **2014**, *43* (27), 10292–10316.

(27) Roth, W. J.; Nachtigall, P.; Morris, R. E.; Jir, C. Two-Dimensional Zeolites : Current Status and Perspectives. *Chem. Rev.* **2014**, *114*, 4807–4837.

(28) Choi, M.; Na, K.; Kim, J.; Sakamoto, Y.; Terasaki, O.; Ryoo, R. Stable Single-Unit-Cell Nanosheets of Zeolite MFI as Active and Long-Lived Catalysts. *Nature* **2009**, *461* (7261), 246–249.

(29) Park, W.; Yu, D.; Na, K.; Jelfs, K. E.; Slater, B.; Sakamoto, Y.; Ryoo, R. Hierarchically Structure-Directing Effect of Multi-Ammonium Surfactants for the Generation of MFI Zeolite Nanosheets. *Chem. Mater.* **2011**, *23* (23), 5131–5137.

(30) Luo, H. Y.; Michaelis, V. K.; Hodges, S.; Griffin, R. G.; Leshkov, Y. R. One - Pot Synthesis of MWW Zeolite Nanosheets Using a Rationally Designed Organic

Structure - Directing Agent. **2015**, 1–24.

(31) Xu, D.; Ma, Y.; Jing, Z.; Han, L.; Singh, B.; Feng, J.; Shen, X.; Cao, F.; Oleynikov, P.; Sun, H.; Terasaki, O.; Che, S. Π-Π Interaction of Aromatic Groups in Amphiphilic Molecules Directing for Single-Crystalline Mesostructured Zeolite Nanosheets. *Nat. Commun.* **2014**, *5* (May), 4262.

(32) Zhang, Y.; Che, S. π–π Interactions Between Aromatic Groups in Amphiphilic Molecules: Directing Hierarchical Growth of Porous Zeolites. *Angew. Chemie - Int. Ed.* **2020**, *59* (1), 50–60.

(33) Marques Mota, F.; Eliášová, P.; Jung, J.; Ryoo, R. Impact of Pore Topology and Crystal Thickness of Nanosponge Zeolites on the Hydroconversion of Ethylbenzene. *Catal. Sci. Technol.* **2016**, *6* (8), 2653–2662.

(34) Seo, Y.; Lee, S.; Jo, C.; Ryoo, R. Microporous Aluminophosphate Nanosheets and Their Nanomorphic Zeolite Analogues Tailored by Hierarchical Structure-Directing Amines. *J. Am. Chem. Soc.* **2013**, *135* (24), 8806–8809.

(35) Jung, J.; Jo, C.; Cho, K.; Ryoo, R. Zeolite Nanosheet of a Single-Pore Thickness Generated by a Zeolite-Structure-Directing Surfactant. *J. Mater. Chem.* **2012**, *22* (11), 4637–4640.

(36) Kim, J. C.; Ryoo, R.; Opanasenko, M. V.; Shamzhy, M. V.; Čejka, J. Mesoporous MFI Zeolite Nanosponge as a High-Performance Catalyst in the Pechmann Condensation Reaction. *ACS Catal.* **2015**, *5* (4), 2596–2604.

(37) Na, K.; Jo, C.; Kim, J.; Ahn, W. S.; Ryoo, R. MFI Titanosilicate Nanosheets with Single-Unit-Cell Thickness as an Oxidation Catalyst Using Peroxides. *ACS Catal.* **2011**, *1* (8), 901–907.

(38) Ren, L.; Guo, Q.; Kumar, P.; Orazov, M.; Xu, D.; Alhassan, S. M.; Mkhoyan, K. A.; Davis, M. E.; Tsapatsis, M. Self-Pillared, Single-Unit-Cell Sn-MFI Zeolite Nanosheets and Their Use for Glucose and Lactose Isomerization. *Angew. Chemie - Int. Ed.* **2015**, *54* (37), 10848–10851.

(39) Kim, J. C.; Kim, W.; Seo, Y.; Kim, J. C.; Ryoo, R.; Verheyen, E.; Jo, C.; Kurttepeli, M.; Vanbutsele, G.; Gobechiya, E.; Kor??nyi, T. I.; Bals, S.; Van Tendeloo, G.; Ryoo, R.; Kirschhock, C. E. A.; Martens, J. A. N-Heptane Hydroisomerization over Pt/MFI Zeolite Nanosheets: Effects of Zeolite Crystal Thickness and Platinum Location. *J. Catal.* **2013**, *300*, 70–80.

(40) Verheyen, E.; Jo, C.; Kurttepeli, M.; Vanbutsele, G.; Gobechiya, E.; Kor??nyi, T. I.; Bals, S.; Van Tendeloo, G.; Ryoo, R.; Kirschhock, C. E. A.; Martens, J. A. Molecular Shape-Selectivity of MFI Zeolite Nanosheets in n-Decane Isomerization and Hydrocracking. *J. Catal.* **2013**, *300*, 70–80.

(41) Kumar Varoon,* Xueyi Zhang,* Bahman Elyassi, Damien D. Brewer, M. G.;

Sandeep Kumar,‡ J. Alex Lee,§ Sudeep Maheshwari,|| Anudha Mittal, C.-Y. S.; Matteo Cococcioni, Lorraine F. Francis, Alon V. McCormick, K. Andre Mkhoyan, M. T. Dispersible Exfoliated Zeolite Nanosheets and Their Application as a Selective Membrane. *Science (80-.).* **2011**, *734* (October), 72–76.

(42) Kumar Varoon Agrawal, Berna Topuz, Zheyu Jiang, Kevin Nguenkam, Bahman Elyassi, Lorraine F. Francis, and M. T. Solution-Processable Exfoliated Zeolite Nanosheets Purified by Density Gradient Centrifugation. *AIChE J.* **2013**, *59* (9), 3458–3467.

(43) Zhang, H.; Xiao, Q.; Guo, X.; Li, N.; Kumar, P.; Rangnekar, N.; Jeon, M. Y.; Al-Thabaiti, S.; Narasimharao, K.; Basahel, S. N.; Topuz, B.; Onorato, F. J.; Macosko, C. W.; Mkhoyan, K. A.; Tsapatsis, M. Open-Pore Two-Dimensional MFI Zeolite Nanosheets for the Fabrication of Hydrocarbon-Isomer-Selective Membranes on Porous Polymer Supports. *Angew. Chemie - Int. Ed.* **2016**, *55* (25), 7184–7187.

(44) Jeon, M. Y.; Kim, D.; Kumar, P.; Lee, P. S.; Rangnekar, N.; Bai, P.; Shete, M.; Elyassi, B.; Lee, H. S.; Narasimharao, K.; Basahel, S. N.; Al-Thabaiti, S.; Xu, W.; Cho, H. J.; Fetisov, E. O.; Thyagarajan, R.; Dejaco, R. F.; Fan, W.; Mkhoyan, K. A.; Siepmann, J. I.; Tsapatsis, M. Ultra-Selective High-Flux Membranes from Directly Synthesized Zeolite Nanosheets. *Nature* **2017**, *543* (7647), 690–694.

(45) Min, B.; Yang, S.; Korde, A.; Kwon, Y. H.; Jones, C. W.; Nair, S. Continuous Zeolite MFI Membranes Fabricated from 2D MFI Nanosheets on Ceramic Hollow Fibers. *Angew. Chemie - Int. Ed.* **2019**, *58* (24), 8201–8205.

(46) Hu, H.; Lyu, J.; Cen, J.; Zhang, Q.; Wang, Q.; Han, W.; Rui, J.; Li, X. The Effect of Si/Al Ratio on the Catalytic Performance of Hierarchical Porous ZSM-5 for Catalyzing Benzene Alkylation with Methanol. *Catal. Sci. Technol.* **2016**, *6* (8), 2647–2652.

(47) Mlinar, A. N.; Zimmerman, P. M.; Celik, F. E.; Head-Gordon, M.; Bell, A. T. Effects of Br??Nsted-Acid Site Proximity on the Oligomerization of Propene in H-MFI. *J. Catal.* **2012**, *288*, 65–73.

(48) Celik, F. E.; Kim, T. J.; Bell, A. T. Effect of Zeolite Framework Type and Si/Al Ratio on Dimethoxymethane Carbonylation. *J. Catal.* **2010**, *270* (1), 185–195.

(49) Wang, Z.; Dornath, P.; Chang, C. C.; Chen, H.; Fan, W. Confined Synthesis of Three-Dimensionally Ordered Mesoporous-Imprinted Zeolites with Tunable Morphology and Si/Al Ratio. *Microporous Mesoporous Mater.* **2013**, *181*, 8–16.

(50) Simone, N.; Carvalho, W. A.; Mandelli, D.; Ryoo, R. Nanostructured MFI-Type Zeolites as Catalysts in Glycerol Etherification with Tert-Butyl Alcohol. *J. Mol. Catal. A Chem.* **2015**, *422*, 115–121.

(51) Cadotte, J. E. US Patent 4,277,344. **1981**, No. 19.

(52) Lau, W. J.; Ismail, A. F.; Misdan, N.; Kassim, M. A. A Recent Progress in Thin Film Composite Membrane: A Review. *Desalination* **2012**, *287*, 190–199.

(53) Jeong, B. H.; Hoek, E. M. V.; Yan, Y.; Subramani, A.; Huang, X.; Hurwitz, G.; Ghosh, A. K.; Jawor, A. Interfacial Polymerization of Thin Film Nanocomposites: A New Concept for Reverse Osmosis Membranes. *J. Memb. Sci.* **2007**, *294* (1–2), 1–7.

(54) Duan, J.; Pan, Y.; Pacheco, F.; Litwiller, E.; Lai, Z.; Pinnau, I. High-Performance Polyamide Thin-Film-Nanocomposite Reverse Osmosis Membranes Containing Hydrophobic Zeolitic Imidazolate Framework-8. *J. Memb. Sci.* **2015**, *476*, 303–310.

(55) Wang, C.; Li, Z.; Chen, J.; Li, Z.; Yin, Y.; Cao, L.; Zhong, Y.; Wu, H. Covalent Organic Framework Modified Polyamide Nanofiltration Membrane with Enhanced Performance for Desalination. *J. Memb. Sci.* **2017**, *523* (July 2016), 273–281.

(56) Maaskant, E.; Wit, P. De; Benes, N. E. Direct Interfacial Polymerization onto Thin Ceramic Hollow Fi Bers. *J. Memb. Sci.* **2018**, *550* (January), 296–301.

(57) Li, Y. X.; Cao, Y.; Wang, M.; Xu, Z. L.; Zhang, H. Z.; Liu, X. W.; Li, Z. Novel High-Flux Polyamide/TiO2 Composite Nanofiltration Membranes on Ceramic Hollow Fibre Substrates. *J. Memb. Sci.* **2018**, *565* (November 2017), 322–330.

(58) Liu, X.; Cao, Y.; Li, Y.; Xu, Z.; Li, Z.; Wang, M.; Ma, X. High-Performance Polyamide / Ceramic Hollow Fi Ber TFC Membranes with TiO 2 Interlayer for Pervaporation Dehydration of Isopropanol Solution. **2019**, *576* (January), 26–35.

(59) Karan, S.; Jiang, Z.; Livingston, A. G. Sub-10 Nm Polyamide Nanofilms with Ultrafast Solvent Transport for Molecular Separation. *Science (80-.).* **2015**, *348* (6241), 1347–1351.

(60) Zhang, Z.; Shi, X.; Wang, R.; Xiao, A.; Wang, Y. Ultra-Permeable Polyamide Membranes Harvested by Covalent Organic Framework Nanofiber Scaffolds: A Two-in-One Strategy. *Chem. Sci.* **2019**, *10* (39), 9077–9083.

(61) Gong, G.; Wang, P.; Zhou, Z.; Hu, Y. New Insights into the Role of an Interlayer for the Fabrication of Highly Selective and Permeable Thin-Film Composite Nanofiltration Membrane. *ACS Appl. Mater. Interfaces* **2019**, *11* (7), 7349–7356.

(62) Wang, Z.; Wang, Z.; Lin, S.; Jin, H.; Gao, S.; Zhu, Y.; Jin, J. Nanoparticle-Templated Nanofiltration Membranes for Ultrahigh Performance Desalination. *Nat. Commun.* **2018**, *9* (1).

(63) Shen, X.; Mao, W.; Ma, Y.; Xu, D.; Wu, P.; Terasaki, O.; Han, L.; Che, S. A Hierarchical MFI Zeolite with a Two-Dimensional Square Mesostructure. *Angew. Chemie - Int. Ed.* **2018**, *57* (3), 724–728.

CHAPTER 2. EFFECT OF SI/AL RATIO ON THE CATALYTIC ACTIVITY OF TWO-DIMENSIONAL MFI NANOSHEETS IN AROMATIC ALKYLATION AND ALCOHOL ETHERIFICATION

This chapter and Appendix A are adapted from the published article 'Korde, A.; Min, B.; Almas, Q.; Chiang, Y.; Nair, S.; Jones, C. W. Effect of Si/Al Ratio on the Catalytic Activity of Two-Dimensional MFI Nanosheets in Aromatic Alkylation and Alcohol Etherification. *ChemCatChem* **2019**, *11* (18), 4548–4557.' with permission from John Wiley and Sons. Byunghyun Min and I were co-first authors on this publication and the synthesis and characterization of all the zeolite materials reported in this chapter was carried out by Byunghyun Min, while I carried out the kinetic studies.

2.1 Introduction

Aluminosilicate zeolites are ordered microporous crystalline materials containing TO_4 tetrahedral units, where T is either Si or Al.[1,2] These materials are widely used as catalysts because of the presence of strong acid sites and the shape-selectivity imparted by the ordered porous structure.[3,4] Catalytic cracking, alkylation, and isomerization are some of the important catalyzed by zeolites on an industrial scale.[5–7] Zeolites have also recently received significant attention in the catalytic conversion of biomass derived species.[8] However, the 3D microporous nature of these materials imposes certain limitations. Zeolites exclude many large/bulky molecules from accessing the internal porosity where the vast majority of active sites reside. Hence, such molecules can only be converted on

the external surface of the zeolite with a low catalytic activity.[9,10] Several methods have therefore been investigated to provide a larger accessible surface area for bulky molecules. One method is to synthesize hierarchical zeolites by introducing mesopores in the microporous zeolitic structure to improve the intracrystalline diffusion rate.[11,12] The faster diffusion to and from the catalytic centers also helps to avoid secondary reactions and coke formation, although some reduction in shape-selective effects is often observed.[13] The introduction of mesopores in conventional zeolites to create hierarchical structures is most often achieved through dealumination[14] or desilication.[15] However, these processes lead to the loss of framework atoms and sometimes, a large number of catalytic sites. Other methods such as dual templating using surfactants and hard-templating using polymeric spheres also yield hierarchical zeolites.[13] Irrespective of the synthesis method used, hierarchical zeolites have generally shown higher activity in catalytic conversions of bulky reactants and longer catalyst lifetimes than their purely microporous analogues.[10–12,16]

A third method to reduce the diffusion path length and increase the concentration of easily accessible sites is to synthesize 2D zeolite nanosheets with a high aspect ratio. Choi et al.[17] synthesized single unit cell thick MFI nanosheets with 2 nm thickness along the b-axis in a one-pot synthesis using an appropriately designed organic structure directing agent (SDA). The SDA was a diquaternary ammonium surfactant with a long alkyl chain that formed a lamellar micellar assembly in solution. The ammonium groups, separated by a C_6 alkyl linkage, act as an effective SDA for the MFI structure while the hydrophobic tail restricted the growth of the zeolite along the *b*-direction. The resulting sheet-like morphology led to a very high external surface area with a large fraction of active sites exposed on the surface. These MFI materials have been shown to increase the rate of

catalytic conversion in several reactions as compared to conventional MFI (especially those involving large reactant molecules), and the pivotal role played by the external acid sites in catalyzing these reactions has been elucidated.[18–21]

The concentration of acid sites in zeolites is typically dictated by their silicon-to-aluminum (Si/Al) ratio. The Si/Al ratio is an important property that can also affect the product selectivity[22] in some reactions, and understanding the effects of varying this parameter is a key aspect of uncovering the structure-catalytic property relations. The effect of the Si/Al ratio on the catalytic activity of zeolites has been studied in great detail for conventional 3D zeolites. As examples, Celik et al.[23] studied the carbonylation of dimethoxymethane over conventional 3D MFI and FAU catalysts with varying Si/Al ratios. These researchers proposed that the charged intermediates experience repulsive Coulombic interactions if adsorbed close to each other, as would be the case for low Si/Al ratio catalysts with a large number of active sites in close proximity. This repulsive interaction would increase the activation energy for the dissociation of the adsorbed intermediates, ultimately leading to a reduced TOF. Mlinaar et al.[24] studied the oligomerization of propene over conventional MFI zeolites with different Si/Al ratios. Through quantum chemical calculations, it was shown that the adsorbed oligomers on nearby active sites impose steric constraints that lead to reduction in the TOF. Wang et al.[25] studied the effect of the Si/Al ratio on the morphology and catalytic activity of three-dimensionally ordered mesoporous-imprinted MFI materials. These researchers found that the apparent reaction rate constant for the self-etherification of benzyl alcohol in mesitylene normalized per acid site increased with increasing Si/Al ratio. Based on the analysis of the Thiele modulus and effectiveness factor for the reaction, they showed that the difference in the apparent rate

constants was mainly a result of the mass transport limitations of the benzyl alcohol molecules to internal acid sites. The effect of Si/Al ratio has also been studied in case of MFI with a nanosponge morphology. Kim et al.[26] studied the Pechmann condensation of pyrogallol and resorcinol with ethyl acetoacetate to understand the effect of the density of acid sites by varying the Si/Al ratio on the catalytic activity of MFI nanosponge. They found that the activity per acid site reduced with increasing density of sites achieved by decreasing the Si/Al ratio. A similar trend was observed by Simone et al.[27] who studied the etherification of glycerol with *tert*-butyl alcohol for 2D MFI nanosheets with different Si/Al ratios. These authors speculated there was a decrease in strength of acid sites as the Al content increased.

However, while these studies report the effect on catalytic activity, they provide limited insight into the reasons for the trends obtained. This is particularly true for the few studies available on 2D MFI nanosheets. In this work, we systematically investigate the effect of the Si/Al ratio on the catalytic activity of 2D MFI nanosheets using the liquid phase Friedel-Crafts alkylation of mesitylene with benzyl alcohol and the self-etherification of benzyl alcohol which occurs in parallel. This paper is organized as follows. First, 2D MFI nanosheets with varying Si/Al ratio were synthesized by careful control of synthesis gel pH and reaction duration. A parametric study of Al, Na, water content and pH reveals that 2D MFI nanosheets can be crystallized over a wide range synthetic window. The structural and textural properties of these materials were characterized using XRD, N_2 physisorption, SEM, TEM and ^{27}Al NMR. The acid sites were characterized using temperature programmed desorption of ammonia and FTIR of adsorbed pyridine. The adsorption isotherm of the key reactant, benzyl alcohol, was measured as well. The

catalytic activity for the 2D MFI nanosheets with varying Si/Al ratio was studied with and without the addition of a bulky poison, 2,6 di-*tert*-butylpyridine (DTBP) and the results are explained based on the physical properties of the catalysts.

2.2 Experimental Methods

2.2.1 Synthesis of SDA

The SDA $[C_{22}H_{45}\text{-}N(CH_3)_2\text{-}C_6H_{12}\text{-}N(CH_3)_2\text{-}C_6H_{13}]Br_2$ ($C_{22}\text{-}6\text{-}6$) was synthesized as described by Choi et al.[17] Briefly, 31.2 g of 1-bromodocosane (TCI, 98%) and 137.6 g of N,N,N',N'-tetramethyl-1,6-hexanediamine (Sigma-Aldrich, 99%) was dissolved in 800 mL of a acetonitrile and toluene (1:1 vol/vol) mixture, which was then heated at 343 K for 24 h. The reaction mixture was cooled and the precipitated product ($C_{22}\text{-}6\text{-}0$) was filtered and washed with diethyl ether. Next, this product was dissolved in acetonitrile and reacted with 2 molar equivalents of 1-bromohexane (Sigma-Aldrich, 98%) under reflux conditions for 24 h. The resulting product, $C_{22}\text{-}6\text{-}6$, was filtered and washed with diethyl ether.

2.2.2 Synthesis of Catalysts

The 2D MFI nanosheets were synthesized *via* hydrothermal reaction using $[C_{22}H_{45}\text{-}N(CH_3)_2\text{-}C_6H_{12}\text{-}N(CH_3)_2\text{-}C_6H_{13}]Br_2$ ($C_{22}\text{-}6\text{-}6$) as the SDA. First, $C_{22}\text{-}6\text{-}6$ was dissolved in deionized water at room temperature, followed by addition of sodium hydroxide. Next, appropriate amounts of aluminum sulfate were dissolved in the solution to adjust the Si/Al ratios. After complete dissolution, TEOS was added dropwise under vigorous stirring. Appropriate amounts of sulfuric acid were added into the solution to adjust the pH. Further details of synthesis conditions are given in Table 1. The final gel compositions were as

follows: 30 Na_2O / *x* Al_2O_3 / 100 SiO_2 / *y* H_2SO_4 / 8000 H_2O where *x* = 0, 0.33, 0.5, 1, 2 and *y* = 12, 18 (details in table 1). After vigorous stirring at room temperature for 24 h to form a homogeneous gel, the resulting gel was transferred to Teflon-lined autoclaves and heated at 423 K for 5 or 12 days under rotation (40 rpm). The solid product was recovered by centrifugation, washed with deionized water and dried in an oven at 333K. A bulk (3D) MFI sample was synthesized using tetrapropylammonium hydroxide (TPAOH) as the SDA by hydrothermal reaction at 453 K for 1 day. The as-prepared samples were denoted as follows: 2D MFI (*n*) or 3D MFI (*n*) with *n* representing the Si/Al ratio.

Table 2.1. Synthesis gel compositions and synthesis parameters used in this work

Sample	SiO_2	Al_2O_3	Na_2O	SDA[a]	H_2SO_4	H_2O	pH	Temperature (K)	Time (days)	Si/Al (target)	Si/Al[b] (EDS)
2D MFI (∞)	100	0	30	10	18	8000	11.1	423	5	∞	∞
2D MFI (144)	100	0.33	30	10	18	8000	10.8	423	5	150	144
2D MFI (96)	100	0.5	30	10	18	8000	10.5	423	5	100	96
2D MFI (50)	100	1	30	10	18	8000	10.0	423	5	50	50
2D MFI (25)	100	2	30	10	12	8000	10.7	423	12	25	25
3D MFI (21)	100	2	10	20[c]	0	8000	-	453	1	25	21

[a] Structure Directing Agent ($C_{22\text{-}6\text{-}6}$)

[b] Si/Al ratios of the calcined samples determined by EDS. Similar value (Si/Al=21) was measured for 2D MFI (Si/Al=25) sample by ICP-OES

[c] SDA is tetrapropylammonium hydroxide (TPAOH) instead of $C_{22\text{-}6\text{-}6}$

2.2.3 Post-Treatment of Catalysts

All synthesized samples were calcined at 823 K for 4 h (ramping at 2 K/min) in air to activate the pore structure by decomposition of the SDA. The calcined samples were then ion-exchanged to the proton form (H^+) by treatment with 0.1M NH_4NO_3 at 353 K three times, followed by calcination again at 823 K for 4 h in air.

2.2.4 Characterization

Powder X-ray diffraction (XRD) patterns were recorded at room temperature on a PANalytical XPert PRO Alpha-1 diffractometer using Cu Kα radiation in the 2θ range from 5° to 50°. Scanning electron micrograph (SEM) images were obtained using a Hitachi SU8010 SEM microscope operating at 3 kV without a metal coating. Transmission electron micrograph (TEM) images were obtained on a FEI Tecnai F30 at 300 kV. The samples were suspended in ethanol and dispersed over a holey carbon film grid. Elemental analysis (Si/Al ratio) was carried out by energy-dispersive X-ray Spectroscopy (EDX) and inductively coupled plasma emission spectroscopy (ICP-AES) using a Perkin Elmer Optima 3000 DV. The nitrogen physisorption isotherms were measured with a Tristar II 3020 (Micromeritics) at 77 K. Nuclear magnetic resonance (NMR) spectra were recorded on a Bruker Avance III 400 spectrometer. ^{27}Al magic angle spinning (MAS) NMR spectra were measured with fully hydrated samples and operated at 400 MHz using 2.5 mm rotors. All spectra were obtained under same conditions: 5 μs pulse, 1 s relaxation delay, 10 kHz spinning rate, and 4000 acquisitions. The chemical shifts are referenced with respect to 1M aqueous solution of $Al(NO_3)_3$. The acid site densities of the catalysts were evaluated by the temperature programmed desorption of ammonia (NH_3-TPD) using a Micromeritics

AutoChem II automated chemisorption analyzer equipped with a thermal conductivity detector (TCD). A known amount of the zeolite was loaded onto a quartz wool plug in a U-shaped glass tube and heated to 773 K under helium flow and held at that temperature for an hour to activate the sample. It was then cooled to 373 K, after which ammonia in helium was injected and flowed through the tube for 2 h. The temperature was then ramped to 873 K at 10 K/min and the desorbed ammonia was detected using the TCD. The desorption profile was deconvoluted by fitting Gaussian distributions to quantify the acid sites. To evaluate the concentrations of Brønsted and Lewis acid sites, FTIR spectroscopy of adsorbed pyridine was performed on a Thermo Scientific Nicolet 8700 spectrometer. The powder samples were pressed into a 1 cm size self-supporting pellet and activated at 873 K for 6 h in a sealed cell. Pyridine adsorption was carried out at 423 K for 20 min followed by desorption at different evacuation temperatures and the FTIR spectra were recorded. Single-component benzyl alcohol adsorption isotherms were obtained using a dynamic vapor sorption instrument (DVS, Surface Measurement Systems) at 50 ^{o}C.

2.2.5 Catalytic Activity Measurements

The liquid phase alkylation of mesitylene with benzyl alcohol was carried out in a similar manner as reported by Zhang et al.[28] The desired amount of catalyst, which had been activated at 823 K for 4 h, was added to a 50 mL two-neck flask. 15 mL of mesitylene and 0.25 mL of dodecane (internal standard) were sequentially added and the reaction mixture was heated at 343 K for 30 minutes before 0.25 mL of benzyl alcohol was added. The reaction mixture was stirred with a 1'' stir bar at >500 rpm to eliminate external mass transfer limitations. Samples (0.1 mL) were periodically collected and filtered using a 0.45 μm syringe filter to remove the catalyst particles before being analyzed using a Shimadzu

GC-2010 gas chromatograph equipped with a Rtx-5 column and a flame ionized detector (FID). The reaction progress was tracked based on the conversion of benzyl alcohol. The reaction with each catalyst sample was carried out 3 times to ensure reproducibility and the average value of conversion (based on benzyl alcohol consumption) for each time point has been reported.

The poisoning experiments with DTBP were carried out under the same reaction conditions as mentioned earlier except that a 5-molar excess of DTBP compared to the total number of acid sites employed in the reaction was used.[28] Typically, the activated catalyst, DTBP, mesitylene and dodecane were added in sequence. This mixture was then maintained at the reaction conditions for 2.5 hours before the addition of benzyl alcohol to ensure that the acid sites present on the external surface of the 2D MFI nanosheets had sufficient time to interact with the DTBP. Samples were periodically collected as described previously and analyzed using a GC

For the catalytic reactions of benzene with benzyl alcohol, 2.33 mmol of benzyl alcohol, 46.5 mmol of benzene and 0.68 mmol of dodecane (internal standard) was added to a 25 mL two-neck flask containing the desired amount of catalyst, such that molar ratio of benzyl alcohol to acid sites was 240. The flask was fitted with a condenser and the reaction was run at 353 K in an oil bath. Samples were withdrawn at the desired time intervals and analyzed using a Shimadzu GC-2010 gas chromatograph equipped with a Rtx-5 column and a flame ionized detector (FID). The reaction progress was tracked based on the conversion of benzyl alcohol. The reaction with each sample was carried out 3 times to ensure reproducibility and the average value of conversion (based on benzyl alcohol consumption) for each time point has been reported. The conversion values from the first

two hours were used to calculate the initial TOF since the conversion was linear with time in this interval. The mass balance was within 95% for each time point. The DTBP poisoning experiments were carried out under the same reaction conditions as mentioned earlier except that a 5-molar excess of DTBP compared to the total number of acid sites employed in the reaction was used.[29,30] Typically, the catalyst, benzene and dodecane were added followed by the desired amount of DTBP. This mixture was then maintained at the reaction conditions before the addition of benzyl alcohol to ensure that the acid sites present on the external surface of the 2D MFI nanosheets had sufficient time to interact with the DTBP.

2.3 Results and Discussion

2.3.1 Synthesis parametric study and structural properties of 2D MFI catalysts

A parametric study of Al, Na, water content and pH was investigated to explore the synthesis space of the 2D MFI using $C_{22\text{-}6\text{-}6}$ SDA. Table A.1 and Figure A.1 (Appendix A) show the resulting products at different gel compositions and different hydrothermal conditions. At Si/Al ratios below 10, competing pure/mixed phases appear. Although 2D layered MFI was formed at Si/Al ratio of 5, it was in the form of a 3D GIS/ANA-2D MFI composite. Therefore, we explored more synthesis conditions in Si/Al ratios above 15 to form pure 2D MFI. Pure 2D MFI was crystallized at Si/Al ratios above 25. When the Si/Al ratios decrease below 25, the resulting materials were partially amorphous and proved difficult to completely crystallize. Therefore, the synthesis duration, pH and water content were adjusted to find the optimal synthesis conditions for 2D MFI (Si/Al ratio < 25). When the syntheses were conducted in the pH range from 10-11, along with an appropriate water

content (H_2O/Si = 80) and increased synthesis time (12 days), pure 2D layered MFI was obtained with high Al content. Otherwise, amorphous phase, 2D layered-bulk MFI composite and MFI nanocrystals were observed.

Figure 2.1 shows the XRD patterns of the synthesized 2D MFI (25, 50, 96, 144, ∞) and 3D MFI (21) materials. As mentioned earlier, XRD patterns confirmed that 2D MFI was successfully crystallized in a wide range of Si/Al ratios by adjusting the synthesis conditions such as Al content, pH of the synthesis gel and synthesis time. All the 2D MFI catalysts have the characteristic patterns of MFI without significant peak broadening. The 2D MFI materials grow in the a-c plane with only unit-cell thickness in the b-direction. Thus, the crystalline order along the b-direction is lost and as a result, compared to the XRD pattern of 3D MFI (21), the pattern for 2D MFI materials only shows sharp (*h*0*l*) peaks reflected from the a-c planes of MFI.[17]

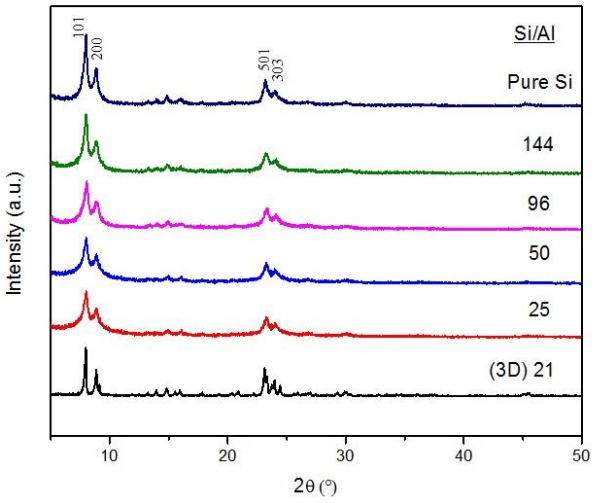

Figure 2.1. Powder XRD patterns for 2D MFI materials with different Si/Al ratios

The structure and morphology of the materials were explored by SEM and TEM, as shown in Figure 2.2. All 2D MFI catalysts showed a hierarchical meso- and microporous structure that consists of multilamellar stacking of nanosheets. All 2D MFI materials exhibit morphologies with intergrown plate-like structures similar to that reported by Choi et al.[17] whereas the 3D MFI (21) shows a more isotropic shape (Figure A.2). SEM and high-resolution transmission electron microscopy (HRTEM) reveal that the 2D MFI nanosheets of unit cell thickness are well-intergrown for all catalysts and multilamellar 2D nanosheets are spaced even after the partial condensation of layers following high-temperature calcination (Figure A.3). Figure 2.2e shows that high Al incorporation led to relatively small particle size with less-intergrown plates, which is more remarkable for the 2D MFI (16) sample as shown in Figure A.4. This is because high Al incorporation into MFI generally retards the crystallization rate and long-range ordering.[29] Although 2D MFI (16) - which has the highest Al content of the materials synthesized in this work - displayed the characteristic PXRD patterns associated with 2D layered MFI, the large amount of Al resulted in relatively low micropore volume (0.07 cm^3/g) and randomly oriented nanosheets, as shown in Figure A.4. Therefore, 2D MFI (16) was excluded for further catalytic experiments. N_2 physisorption isotherms are shown in Figure 2.3 and the corresponding textural properties in Table 2.2. All 2D MFI materials show type IV isotherms with a hysteresis loop corresponding to mesopores. A decreased mesopore size in 2D MFI (25) leads to a shift of the hysteresis to lower relative pressures. The 3D MFI (21) has a type I isotherm characteristic of microporous structures without mesopores. From Table 2.2, all the catalysts have substantially high micropore volumes (> 0.1 cm^3/g). The fractions of mesopore volume ($V_{meso}/V_{total} > 0.76$) and external surface areas (S_{ext}/S_{BET}

> 0.41) for all the 2D MFI materials are substantially higher than for the 3D MFI (21), revealing the hierarchical micro-meso nature of the 2D MFI catalysts.

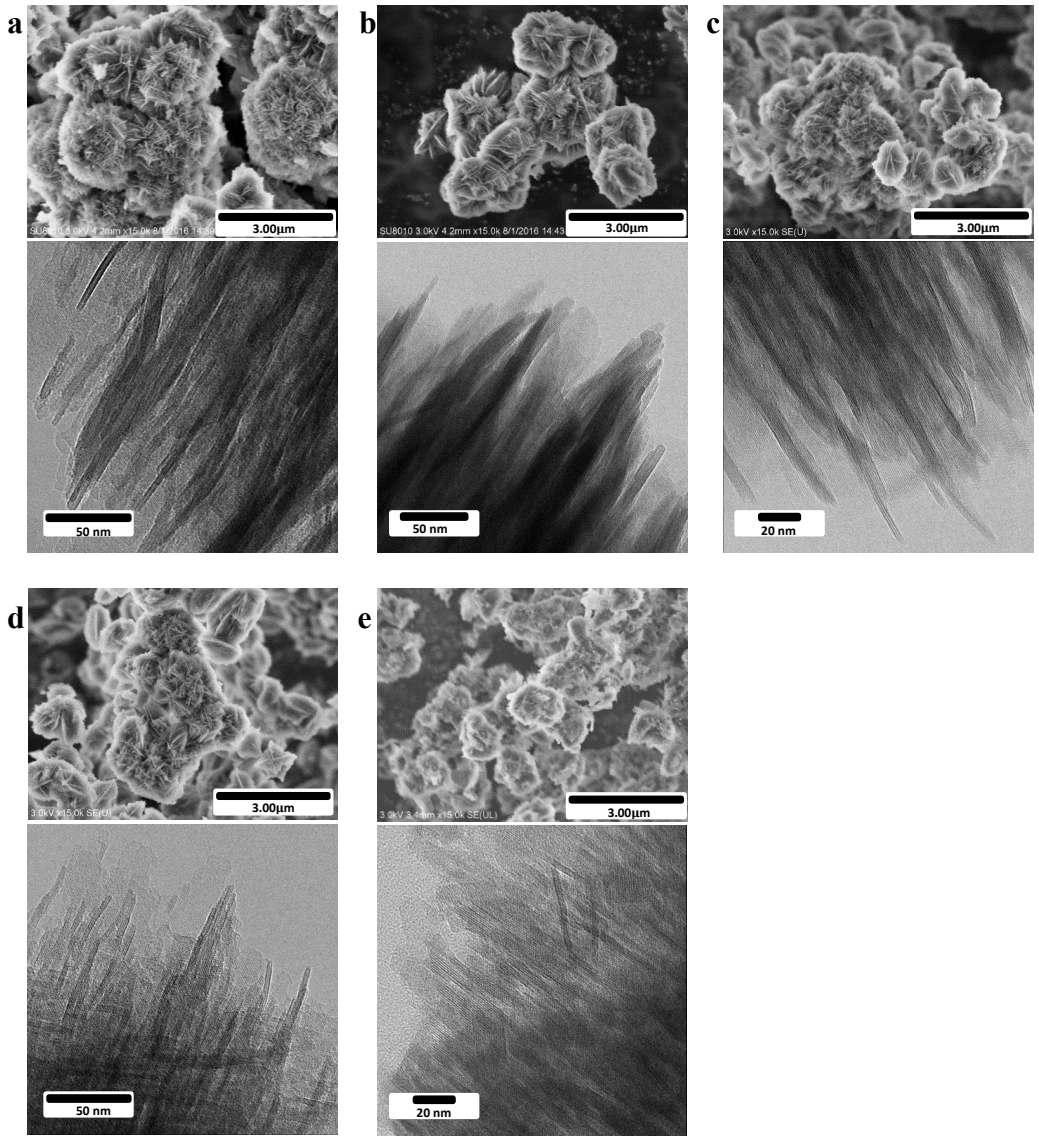

Figure 2.2. SEM and TEM images of 2D MFI materials with Si/Al ratios of (a) ∞, (b) 144, (c) 96, (d) 50 and (e) 25.

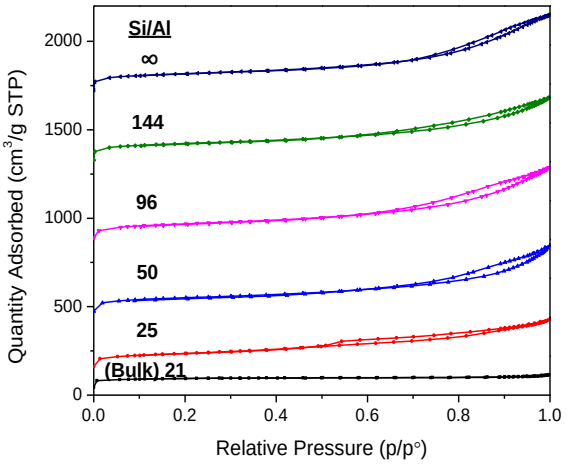

Figure 2.3. N_2 physisorption isotherms of 2D MFI materials with Si/Al ratios of (a) 1, (b) 144, (c) 96, (d) 50, (e) 25 and (f) bulk MFI with Si/Al ratio of 21. The isotherms are vertically offset by equal intervals of 250 cm3/g.

Table 2.2. Textural properties of 2D MFI materials obtained from N_2 physisorption isotherms.

Si/Al	S_{BET}[a] (m^2/g)	S_{micro} (m^2/g)	S_{ext} (m^2/g)	V_{micro}[b] (cm^3/g)	V_{total}[c] (cm^3/g)	V_{meso}[d] (cm^3/g)	V_{meso}/V_{total}	S_{ext}/S_{BET}
∞	518	282	236	0.12	0.69	0.57	0.83	0.46
144	525	310	215	0.13	0.56	0.43	0.77	0.41
96	556	304	252	0.13	0.67	0.54	0.81	0.45
50	518	308	210	0.13	0.58	0.45	0.76	0.41
25	481	238	243	0.1	0.46	0.36	0.78	0.51
21 (Bulk)	347	287	60	0.12	0.17	0.05	0.29	0.17

[a]Determined from the BET method, although the BET method does not strictly apply to microporous solids, the presence of mesoporosity in the samples suggests its use; [b]Determined from t-plot method; [c]Determined from the adsorbed volume at P/P_0=0.97;

[d]Determined by V_{total}-V_{micro}.

Figure 2.4 shows the ^{27}Al NMR spectra for Al incorporated 2D MFI catalysts, giving insight into the bonding environments of the Al sites. The peak at 54 ppm corresponds to tetrahedrally coordinated Al inside the framework, giving rise to Brønsted acid sites, whereas the peak at 0 ppm corresponds to octahedrally coordinated extra-framework Al. The spectra show that Al is mostly located inside the 2D MFI framework, thus revealing that Al in the synthesis gel is successfully incorporated into the catalysts. However, there is some fraction of Al that is not incorporated as demonstrated by the peak at 0 ppm and this is more prominent for the 2D MFI (144) and 2D MFI (96) samples.

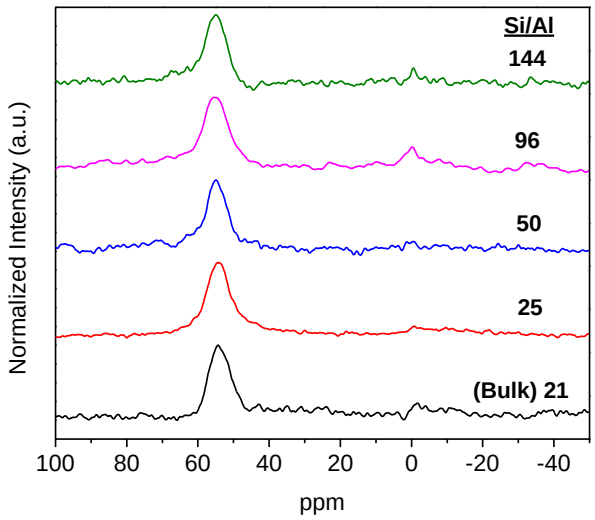

Figure 2.4. ^{27}Al MAS NMR spectra of 2D MFI materials with Si/Al ratios of (a) 144, (b) 96, (c) 50, (d) 25 and (e) bulk MFI with Si/Al ratio of 21.

Ammonia TPD was employed to measure the acid site densities. Each material shows two desorption peaks at around 439 K and 593 K (Figure A.5) corresponding to physisorbed ammonia and ammonia chemisorbed to the acid sites respectively. The latter peak was used to calculate the total acid site density, assuming one ammonia molecule adsorbed per acid site.[31] The desorption profile was deconvoluted by fitting Gaussian

curves and the area corresponding to the second TPD peak was used to calculate the concentration of acid sites. Ammonia TPD is a common technique to quantify the total acid sites but it does not distinguish between Brønsted and Lewis acid sites. This can be accomplished via adsorption of pyridine followed by FTIR spectroscopy. Brønsted and Lewis acid site concentrations are calculated based on the corresponding molar extinction coefficients and integral intensities of the peaks appearing at 1545 cm^{-1} and 1454 cm^{-1} respectively (Figure A.6).[32] The total acid sites estimated using this method matches very well with those obtained using NH_3 TPD, as summarized in Table 2.3. The increase in the proportion of Lewis acid sites for the higher Si/Al ratio catalysts is consistent with the extra-framework Al as described earlier based on the ^{27}Al NMR. As expected, the acid site density increases with decreasing Si/Al ratio or increasing Al content. However, it does vary for the same Si/Al ratio if the morphology is different, as seen in the case of 3D MFI (21) vs 2D MFI (25) and also reported by previous studies.[26,27]

Table 2.3. Acid site densities as measured by NH3 TPD and pyridine adsorption.

Si/Al ratio[a]	Acid site density (μmol/g)[b]	BA_{total} (μmol/g)[c]	LA_{total} (μmol/g)[c]	Total acid site density (μmol/g)[c]
25	243	121	82	203
50	150	67	60	127
96	90	59	45	104
144	61	21	26	47

[a]Measured using EDS; [b]Measured using NH_3 TPD; [c]Measured using FTIR spectroscopy of adsorbed pyridine.

2.3.2 Catalytic activity of 2D MFI nanosheets

The catalytic activity of the 2D MFI catalysts was studied in the liquid phase Friedel-Crafts alkylation of mesitylene with benzyl alcohol. The reactions referred to in Figure 2.5 occur in parallel and lead to the formation of 1,3,5-trimethyl-2-benzylbenzene through the alkylation reaction while the self-etherification of benzyl alcohol produces dibenzyl ether.

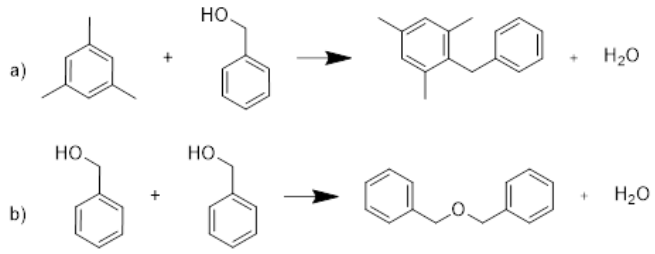

Figure 2.5. Parallel reactions occurring in the system – a) Alkylation of mesitylene with benzyl alcohol & b) Self-etherification of benzyl alcohol

As shown in previous works, the alkylation of mesitylene occurs exclusively on the external surface of the 2D MFI catalysts since the bulky mesitylene cannot diffuse into the micropores while the etherification of benzyl alcohol occurs on the external surface as well as the micropores.[28,33,34] Both of these reactions are catalyzed by the Brønsted acid sites in the catalysts. In each case, sufficient catalyst was added to the reaction to ensure conversions that could be reliably measured. The amount of catalyst added has been shown to not affect their turnover frequencies (TOFs),[34] and hence a direct comparison of the TOFs for the different 2D MFI catalysts is possible. The kinetic data for each of the catalysts are shown in Figures 2.6 and these data were used to calculate their TOF (with respect to the total Brønsted acid sites). The TOF based on the total benzyl alcohol consumption in the two reactions shown in Figure 2.5 for the different 2D MFI catalysts is

plotted in Figure 2.7a (selectivity reported in Table A.2) and it is found to decrease with decreasing Si/Al ratio of the catalyst. Since a decrease in Si/Al ratio corresponds to an increase in the concentration of acid sites, the behavior observed above implies that increasing the density of acid sites with decreasing Si/Al ratio reduces their catalytic activity. These findings are also applicable to the catalytic conversion of benzyl alcohol in benzene. (Figure A.7 & Figure A.8).

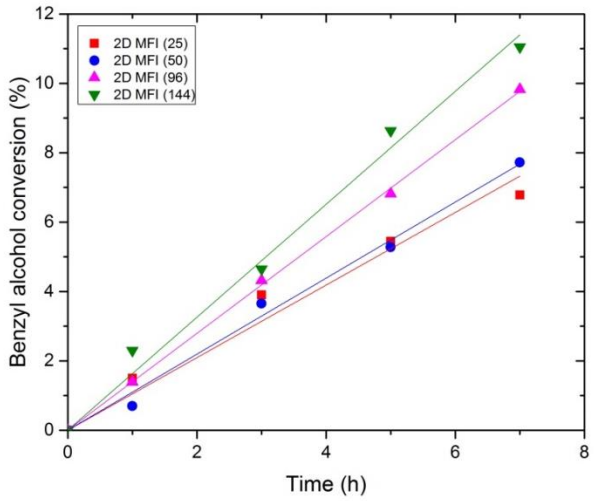

Figure 2.6. Conversion of benzyl alcohol for the mesitylene experiments carried out over 2D MFI (n) catalysts with different Si/Al ratios (n = 25, 50, 96, 144).

Figure 2.7a shows the overall TOFs based on the benzyl alcohol consumed in both the alkylation and self-etherification reactions. It can be deconvoluted into the TOFs for each reaction by calibrating for the dibenzyl ether concentration, as shown in Figure 2.7b. The TOFs for the alkylation reaction show much smaller variation compared to those for the self-etherification reaction, which increases with higher Si/Al ratio of the 2D MFI catalysts. This negligible variation in the TOF of the alkylation reaction is also supported by the work of Zhang et al.[28], where it was demonstrated that the catalytic activity of the

external acid sites towards the alkylation reaction is similar across different MFI morphologies using the same model reaction. This work shows that varying SI/Al ratio over zeolites with the same morphology also does not affect the TOFs of exclusively surface catalyzed reactions. Thus, it was hypothesized that the differences in the TOFs arising from the variation in Si/Al ratio were possibly stemming from the acid sites located inside the micropores since the self-etherification reaction, which is the main contributor to the trend of the TOFs with the Si/Al ratio, is the only one in the system that occurs in the micropores. To test this hypothesis, the role of the micropores is also highlighted by the TOFs for alkylation and self-etherification when the reaction is carried out in benzene (Figure A.9), which is not as bulky as mesitylene and allows both reactions to occur in the micropores. In case of this reaction, the TOF for self-etherification increases strongly with increasing Si/Al ratio while that for the alkylation reaction may increase modestly as well (Figure A.9), providing further evidence that reactions in the micropores are affected by Si/Al ratio. Jones et al.[35] have demonstrated that the Al density does not affect the acid strength in MFI zeolite. To probe the activity of acid sites located in the micropores, the kinetic measurements for the two extreme Si/Al ratio 2D MFI catalysts were repeated with the addition of a bulky poison, 2,6 di-*tert*-butylpyridine (DTBP). This molecule is sufficiently large such that it cannot access the acid sites located in the internal micropores of MFI and selectively poisons the acid sites on the external surface. In this case, the alkylation reaction stops completely while the etherification reaction can continue in the micropores. The conversion of benzyl alcohol with time for both catalysts is shown in Figure 2.8. Based on the kinetic model proposed by Zhang et al.[28], the effectiveness factor was calculated. In these calculations, the fraction of external acid sites was assumed to be

approximately 30% based on the previous works by Ryoo et al.[26,36] on 2D MFI nanosheets. The rate constant for etherification and the corresponding effectiveness factor for the 2D MFI (144) and 2D MFI (25) catalysts are reported in Table 2.4. The effectiveness factor in this case is found to decrease with the decrease in Si/Al ratio. This differs from the observations of Zhang et al.[28], wherein the effectiveness factors for the SPP MFI catalysts with Si/Al ratios of 75 and 253 were reported to be around 0.8. These differences are likely due to the different material used (SPP MFI vs. 2D MFI nanosheets) and the wider range of Si/Al ratios considered in this work.

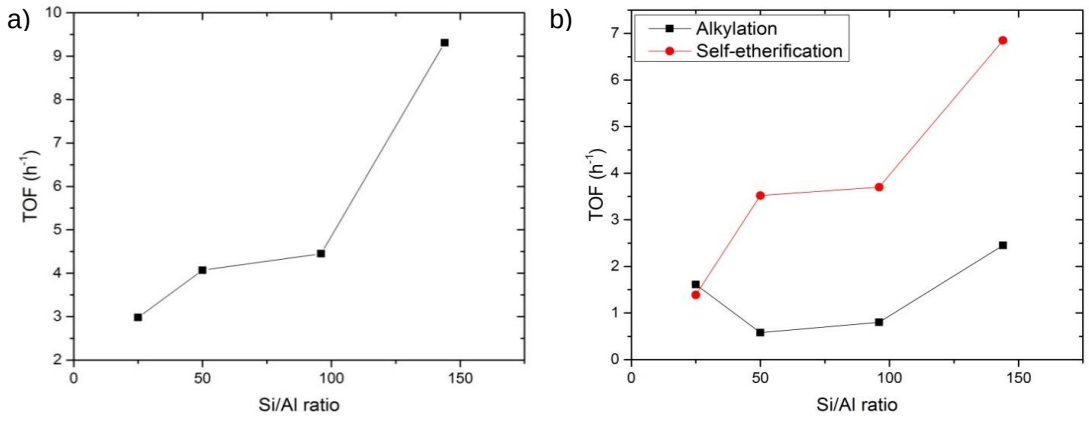

Figure 2.7. (a) TOF based on total benzyl alcohol consumption and (b) TOF for the mesitylene alkylation and self-etherification reactions for the 2D MFI (n) catalysts with different Si/Al ratios (n = 25, 50, 96, 144).

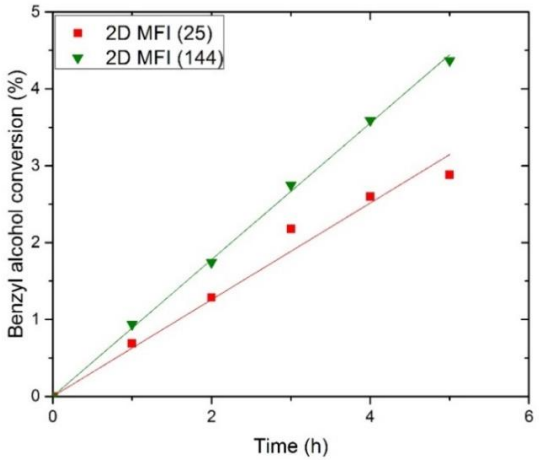

Figure 2.8. Conversion of benzyl alcohol as a function of time for reactions carried out in the presence of DTBP over 2D MFI (25) and 2D MFI (144) catalysts.

The effectiveness factor analysis shows that even though the 2D MFI (25) catalyst has a higher density of acid sites located in the micropores, these acid sites do not show the same activity as those in 2D MFI (144). It must also be noted that even though the value of the effectiveness factor for 2D MFI (144) is obtained to be slightly greater than unity, the numerical values are sensitive to several parameters such as the concentration of acid sites, the isotherm parameters, and other factors, as described in the Supporting Information and should not be taken as being exact. Nevertheless, the key effect observed in Table 2.4 is the substantial (three-fold) increase in effectiveness factor with the increase in Si/Al ratio.

Table 2.4. Reaction rate constants, effectiveness factors & TOF (with and without the addition of DTBP) for the self-etherification of benzyl alcohol with the 2D MFI (25) and 2D MFI (144) catalysts.

Sample	Reaction rate constant (10^{-3} Ls^{-1} [mol H^+]$^{-1}$)	Effectiveness factor	TOF in absence of DTBP (h^{-1})[a]	TOF in presence of DTBP (h^{-1})[b]
2D MFI (25)	0.58	0.53	1.4	2.5
2D MFI (144)	2.04	1.49	6.9	7.3

[a]Normalized to the total number of Brønsted acid sites; [b]Normalized to the Brønsted acid sites in the micropores alone

Based on the measured catalytic activities of the 2D MFI (25) and 2D MFI (144) catalysts with and without the addition of DTBP, it is possible to gain some insight into the role of the internal and external acid sites towards the self-etherification reaction. When DTBP is added to the reaction mixture, only the self-etherification reaction goes on in the micropores and the TOFs for the self-etherification reaction (normalized to the acid sites in the micropores alone) can be calculated. In Table 2.4, these TOF values for the 2D MFI (25) and 2D MFI (144) catalysts are compared to their respective values evaluated in absence of DTBP (reported in Figure 2.7b). The TOFs for the self-etherification reaction in the presence of DTBP are marginally higher for both 2D MFI (25) and 2D MFI (144) catalysts as compared to the case when no DTBP is added. A likely reason is that in the absence of DTBP, alkylation (which occurs on the external acid sites alone) competes with self-etherification and reduces the availability of benzyl alcohol reactant, thereby reducing the TOF for the etherification reaction.

2.3.3 Benzyl alcohol adsorption isotherms

To confirm that the difference in reactivity stems from the micropores, single-component vapor phase adsorption isotherms for benzyl alcohol in the micropore region were measured for the 2D MFI (144) and 2D MFI (25) samples. These measurements were done at 50 ^{o}C to ensure a fast equilibration while at the same time trying to avoid any self-etherification reactions. However, the trends obtained here can be further extrapolated to the reaction temperature as well. The adsorption isotherms are shown in Figure 2.9 and the uptake has been normalized based on the Brønsted acid site density as obtained from FTIR of adsorbed pyridine. It is observed that the uptake of benzyl alcohol per acid site is lower for the 2D MFI (25) catalyst than the 2D MFI (144) catalyst. The reaction studied in this work proceeds through the adsorption of benzyl alcohol on the catalyst surface.[34] Assuming the strength of the acid sites does not change with varying the Si/Al ratio,[37] the higher availability of the reactant molecule (benzyl alcohol) per active site in the micropores for the 2D MFI (144) catalyst is consistent with its higher effectiveness factor in the case of the reaction with the DTBP poisoning and its higher TOF, as compared to the 2D MFI (25) catalyst. This is possibly due to stearic crowding or repulsive interactions between the adsorbed reactant molecules, similar to what has been suggested for other reactions.[23,24] Based on the acid site densities, the 2D MFI (25) and 2D MFI (144) samples are estimated to have ~0.51 and ~0.085 acid sites per nm^3 in the micropores respectively, assuming 70% of the acid sites are in the micropores. Thus, when the molecules of benzyl alcohol react on the acid sites in the micropores, they would be spaced out further in case of the 2D MFI (144) as compared to the 2D MFI (25) catalyst.

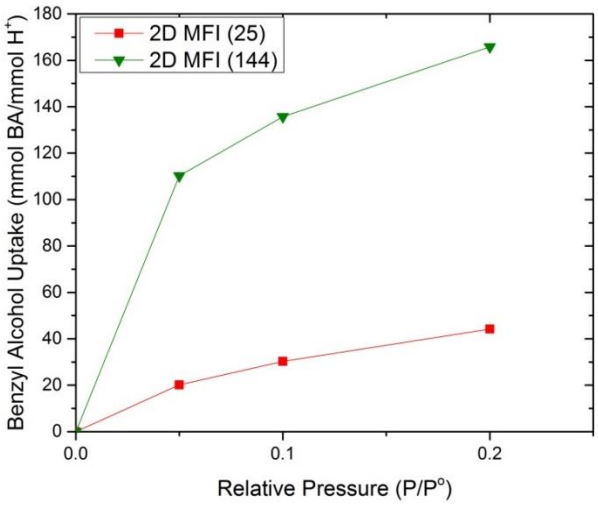

Figure 2.9. Benzyl alcohol adsorption isotherms for the extreme Si/Al ratio 2D MFI catalysts.

2.4 Conclusions

2D MFI nanosheet catalysts with Si/Al ratio varying from 25 to 150 were synthesized by controlling the synthesis conditions. The catalytic activity of these multilamellar 2D MFI nanosheets was investigated using the Friedel-Crafts alkylation of mesitylene with benzyl alcohol and the self-etherification of benzyl alcohol which occurs in parallel. The total acid site density of the catalyst samples increased with decreasing Si/Al ratio, while the overall TOF calculated using the total benzyl alcohol consumption with respect to the total Brønsted acid sites decreased. The deconvolution of the overall TOF showed that the self-etherification of benzyl alcohol and not the alkylation was the main contributor to this trend. Repeating the reaction by poisoning the external acid sites on the 2D MFI (25) and 2D MFI (144) catalysts with a bulky poison, DTBP, stops the alkylation reaction completely, while the etherification of benzyl alcohol still continues to occur in the micropores. The effectiveness factor for the etherification reaction was found to decrease

with decreasing Si/Al ratio. The benzyl alcohol adsorption isotherms for these two extreme Si/Al ratio catalysts show that the uptake per acid site increases with increasing Si/Al ratio and thus there is more reactant availability per active site that can be converted. This is consistent with the increase in the effectiveness factor and TOF with increasing Si/Al ratio for the 2D MFI catalysts. Thus, we have shown that although the density of acid sites can be increased by decreasing the Si/Al ratio of 2D MFI nanosheets, for the case of the self-etherification reaction and benzene alkylation reaction that occur in the micropores, the reactant availability per active site decreases with decreasing Si/Al ratio and this correlates to an increasing TOF with increasing Si/Al ratio.

2.5 References

(1) Auerbach, M. S.; Carrado, K. A.; Dutta, P. K. *Handbook of Zeolite Science and Technology*; New York, 2003.

(2) Cundy, C. S.; Cox, P. A. The Hydrothermal Synthesis of Zeolites: History and Development from the Earliest Days to the Present Time. *Chem. Rev.* **2003**, *103* (3), 663–701.

(3) Corma, A. Inorganic Solid Acids and Their Use in Acid-Catalyzed Hydrocarbon Reactions. *Chem. Rev.* **1995**, *95* (3), 559–614.

(4) Davis, M. E. Ordered Porous Materials for Emerging Applications. *Nature* **2002**, *417* (6891), 813–821.

(5) Venuto, P. B.; Habib, E. T. J. *Fluid Catalytic Cracking with Zeolite Catalysts*; Marcel Dekker, Inc.: New York, 1979.

(6) Venuto, P.B., Hamilton, A., Landis, P.S. and Wise, J. J. Organic Reactions Catalyzed by Crystalline Aluminosilicates I. Alkylation Reactions. *J. Catal.* **1966**, *4*, 81–98.

(7) Skeels, G. W.; Flanigen, E. M. Normal Paraffin Hydrocarbon Isomerization Process Using Activated Zeolite Beta. 5,095,169, 1992.

(8) Ennaert, T.; Van Aelst, J.; Dijkmans, J.; De Clercq, R.; Schutyser, W.; Dusselier, M.; Verboekend, D.; Sels, B. F. Potential and Challenges of Zeolite Chemistry in the Catalytic Conversion of Biomass. *Chem. Soc. Rev.* **2016**, *45* (3), 584–611.

(9) Möller, K.; Bein, T. Mesoporosity--a New Dimension for Zeolites. *Chem. Soc. Rev.* **2013**, *42* (9), 3689–3707.

(10) Bhan, A.; Tsapatsis, M. Zeolites with Nanometer Diffusion Lengths and Implications in Shape Selective Catalysis. *Curr. Opin. Chem. Eng.* **2013**, *2* (3), 320–324.

(11) Na, K.; Somorjai, G. A. Hierarchically Nanoporous Zeolites and Their Heterogeneous Catalysis: Current Status and Future Perspectives. *Catal. Letters* **2015**, *145* (1), 193–213.

(12) Pérez-Ramírez, J.; Christensen, C. H.; Egeblad, K.; Christensen, C. H.; Groen, J. C. Hierarchical Zeolites: Enhanced Utilisation of Microporous Crystals in Catalysis by Advances in Materials Design. *Chem. Soc. Rev.* **2008**, *37* (11), 2530.

(13) Serrano, D. P.; Escola, J. M.; Pizarro, P. Synthesis Strategies in the Search for Hierarchical Zeolites. *Chem. Soc. Rev.* **2013**, *42* (9), 4004–4035.

(14) Beyerlein, R. A.; Choi-feng, C.; Hall, J. B.; Huggins, B. J.; Ray, G. J. Effect of Steaming on the Defect Structure and Acid Catalysis of Protonated Zeolites. *Top. Catal.* **1997**, *4*, 27–42.

(15) Ogura, M.; Shinomiya, S.; Tateno, J.; Nara, Y.; Kikuchi, E.; Matsukata, M. Formation of Uniform Mesopores in ZSM-5 Zeolite through Treatment in Alkaline Solution. *Chem. Lett.* **2000**, No. 8, 882–883.

(16) Holm, M. S.; Taarning, E.; Egeblad, K.; Christensen, C. H. Catalysis with Hierarchical Zeolites. *Catal. Today* **2011**, *168* (1), 3–16.

(17) Choi, M.; Na, K.; Kim, J.; Sakamoto, Y.; Terasaki, O.; Ryoo, R. Stable Single-Unit-Cell Nanosheets of Zeolite MFI as Active and Long-Lived Catalysts. *Nature* **2009**, *461* (7261), 246–249.

(18) Kim, J. C.; Cho, K.; Ryoo, R. High Catalytic Performance of Surfactant-Directed Nanocrystalline Zeolites for Liquid-Phase Friedel-Crafts Alkylation of Benzene Due to External Surfaces. *Appl. Catal. A Gen.* **2014**, *470*, 420–426.

(19) Kim, W.; Kim, J. C.; Kim, J.; Seo, Y.; Ryoo, R. External Surface Catalytic Sites of Surfactant-Tailored Nanomorphic Zeolites for Benzene Isopropylation to Cumene. *ACS Catal.* **2013**, *3* (2), 192–195.

(20) Kim, K.; Ryoo, R.; Jang, H.; Choi, M. Spatial Distribution , Strength , and Dealumination Behavior of Acid Sites in Nanocrystalline MFI Zeolites and Their Catalytic Consequences. *J. Catal.* **2012**, *288*, 115–123.

(21) Kim, J. C.; Kim, T. W.; Kim, Y.; Ryoo, R.; Jeong, S. Y.; Kim, C. U. Mesoporous MFI Zeolites as High Performance Catalysts for Diels-Alder Cycloaddition of Bio-Derived Dimethylfuran and Ethylene to Renewable p-Xylene. *Appl. Catal. B*

Environ. **2017**, *206*, 490–500.

(22) Hu, H.; Lyu, J.; Cen, J.; Zhang, Q.; Wang, Q.; Han, W.; Rui, J.; Li, X. The Effect of Si/Al Ratio on the Catalytic Performance of Hierarchical Porous ZSM-5 for Catalyzing Benzene Alkylation with Methanol. *Catal. Sci. Technol.* **2016**, *6* (8), 2647–2652.

(23) Celik, F. E.; Kim, T. J.; Bell, A. T. Effect of Zeolite Framework Type and Si/Al Ratio on Dimethoxymethane Carbonylation. *J. Catal.* **2010**, *270* (1), 185–195.

(24) Mlinar, A. N.; Zimmerman, P. M.; Celik, F. E.; Head-Gordon, M.; Bell, A. T. Effects of Br??Nsted-Acid Site Proximity on the Oligomerization of Propene in H-MFI. *J. Catal.* **2012**, *288*, 65–73.

(25) Wang, Z.; Dornath, P.; Chang, C. C.; Chen, H.; Fan, W. Confined Synthesis of Three-Dimensionally Ordered Mesoporous-Imprinted Zeolites with Tunable Morphology and Si/Al Ratio. *Microporous Mesoporous Mater.* **2013**, *181*, 8–16.

(26) Kim, J. C.; Ryoo, R.; Opanasenko, M. V.; Shamzhy, M. V.; Čejka, J. Mesoporous MFI Zeolite Nanosponge as a High-Performance Catalyst in the Pechmann Condensation Reaction. *ACS Catal.* **2015**, *5* (4), 2596–2604.

(27) Simone, N.; Carvalho, W. A.; Mandelli, D.; Ryoo, R. Nanostructured MFI-Type Zeolites as Catalysts in Glycerol Etherification with Tert-Butyl Alcohol. *J. Mol. Catal. A Chem.* **2015**, *422*, 115–121.

(28) Zhang, X.; Liu, D.; Xu, D.; Asahina, S.; Cychosz, K. a.; Agrawal, K. V.; Al Wahedi, Y.; Bhan, a.; Al Hashimi, S.; Terasaki, O.; Thommes, M.; Tsapatsis, M. Synthesis of Self-Pillared Zeolite Nanosheets by Repetitive Branching. *Science (80-.).* **2012**, *336* (6089), 1684–1687.

(29) Emdadi, L.; Oh, S. C.; Wu, Y.; Oliaee, S. N.; Diao, Y.; Zhu, G.; Liu, D. The Role of External Acidity of Meso-/Microporous Zeolites in Determining Selectivity for Acid-Catalyzed Reactions of Benzyl Alcohol. *J. Catal.* **2016**, *335*, 165–174.

(30) Kim, W.; Kim, J.; Kim, J.; Seo, Y.; Ryoo, R. External Surface Catalytic Sites of Surfactant-Tailored Nanomorphic Zeolites for Benzene Isopropylation to Cumene. **2013**, 8–11.

(31) Kim, J.; Kim, W.; Seo, Y.; Kim, J. C.; Ryoo, R. N-Heptane Hydroisomerization over Pt/MFI Zeolite Nanosheets: Effects of Zeolite Crystal Thickness and Platinum Location. *J. Catal.* **2013**, *301*, 187–197.

(32) Emeis, C. A. Determination of Integrated Molar Extinction Coefficients for Infrared Absorption Bands of Pyridine Adsorbed on Solid Acid Catalysts. *Journal of Catalysis*. 1993, pp 347–354.

(33) Emdadi, L.; Wu, Y.; Zhu, G.; Chang, C.-C.; Fan, W.; Pham, T.; Lobo, R. F.; Liu, D.

Dual Template Synthesis of Meso- and Microporous MFI Zeolite Nanosheet Assemblies with Tailored Activity in Catalytic Reactions. *Chem. Mater.* **2014**, *26* (3), 1345–1355.

(34) Xu, D.; Abdelrahman, O.; Liu, D.; Dauenhauer, P.; Tsapatsis, M. A Quantitative Study of the Structure – Activity Relationship in Hierarchical Zeolites Using Liquid-Phase Reactions. *AIChE J.* **2019**, *65* (3), 1067–1075.

(35) Jones, A. J.; Carr, R. T.; Zones, S. I.; Iglesia, E. Acid Strength and Solvation in Catalysis by MFI Zeolites and Effects of the Identity , Concentration and Location of Framework Heteroatoms. *J. Catal.* **2014**, *312*, 58–68.

(36) Seo, Y.; Cho, K.; Jung, Y.; Ryoo, R. Characterization of the Surface Acidity of MFI Zeolite Nanosheets by 31 P NMR of Adsorbed Phosphine Oxides and Catalytic Cracking of Decalin. *ACS Catal.* **2013**, *3* (4), 713–720.

(37) Jones, A. J.; Carr, R. T.; Zones, S. I.; Iglesia, E. Acid Strength and Solvation in Catalysis by MFI Zeolites and Effects of the Identity , Concentration and Location of Framework Heteroatoms. *J. Catal.* **2014**, *312*, 58–68.

CHAPTER 3. AEL ZEOLITE NANOSHEET-POLY(AMIDE) NANOCOMPOSITE MEMBRANES ON α-ALUMINA HOLLOW FIBERS WITH ENHANCED PERVAPORATION PROPERTIES

Parts of this chapter are adapted from 'Korde, A.; Min, B.; Ganesan, A.; Yang, S.; Grosz, A.; Jones, C. W; Nair, S. AEL Zeolite Nanosheet-Poly(amide) Nanocomposite Membranes on α-Alumina Hollow Fibers with Enhanced Pervaporation Properties, **(***In Preparation)*'

3.1 Introduction

To address the increasing stress on global potable water supplies, it is essential to develop more energy-efficient and high-throughput desalination processes for both brackish water and seawater.[1,2] Thin-film composite (TFC) membranes composed of a thin poly(amide) (PA) layer have been widely used for reverse osmosis (RO) and nanofiltration (NF)-based desalination of water.[3,4] These PA membranes are fabricated via the interfacial polymerization (IP) of two monomers: a diamine in aqueous phase and an acyl chloride in an organic phase, with the polymerization taking place at the interface of the two phases.[5] However, these membranes suffer from a permeance-selectivity tradeoff that is common for polymeric membranes.[6] To boost the performance of TFC membranes, Jeong et al.[7] demonstrated thin-film nanocomposite (TFN) membranes incorporating NaA zeolite nanoparticles into the PA selective layer. Incorporation of the zeolite nanoparticles helped to improve water permeability while maintaining solute rejection. Several later reports studied the incorporation of a wide range of nanomaterials, such as MOFs,[8] COFs,[9] carbon

nanotubes (CNT),[10] graphene oxide (GO),[11] aluminosilicate nanotubes,[12] cellulose nanocrystals (CNC)[13] and cellulose nanofibers (CNF).[14] In each of these cases, the TFN membranes showed improved water permeability while maintaining a high rejection of the solutes being tested. Most of these hybrid TFN membranes were fabricated by dispersing the nanomaterial of interest in the aqueous diamine solution, followed by IP with an acid chloride in the organic phase during which the polymer encapsulates the nanomaterials as the interfacial film is formed.

More recent reports have taken the approach of modifying the porous polymeric substrates with specific nanomaterials before carrying out the IP reaction. This resulted in ultra-high solvent permeances while maintaining high solute rejections in nanofiltration applications. These composite membranes tend to form a multi-layered morphology and are different from the hybrid morphology described earlier. Karan et al.[15] fabricated ultra-thin PA films on porous supports with a deposited layer of cadmium hydroxide nanostrands. This intermediate layer provided a smoother surface as well as a reservoir that can store the diamine solution and control its release, thus enabling the formation of an ultra-thin and defect-free PA film that demonstrated a high methanol permeance of 52.2 L m^{-2} h^{-1} bar^{-1} while maintaining high rejections of dyes. Following this, Zhu et al.[16] fabricated an ultra-thin PA film via IP on a poly(ether sulfone) (PES) support coated with a poly(dopamine) (PDA) wrapped single-walled carbon nanotube layer, while Wu et al.[17] coated the same support with multi-walled carbon nanotubes. Both membranes displayed high water permeances in the range of 17 – 32 L m^{-2} h^{-1} bar^{-1} with >95% rejections for divalent salts. Other materials such as CNCs,[18] COFs[19] and a tannic acid/Fe^{+3}

nanoscaffolds[20] have also been utilized as an intermediate layer between the support and the PA film to enhance the permeance and overcome the selectivity-permeability tradeoff.

All efforts for substrate modifications using nanomaterials have so far been focused on organic PES supports. As compared to organic supports, inorganic supports such as α-alumina hollow fibers have much higher stability under harsh conditions. They are easily mass-produced and possess a high membrane area per unit volume, thus making them desirable for use as supports for industrial membrane applications. However, direct fabrication of TFC membranes on α-alumina hollow fibers is challenging due to the poor interfacial adhesion characteristics of PA with ceramic surfaces. Shi et al.[21] fabricated a TFC membrane on a α-alumina hollow fibers coated with a PDA or poly(ethyleneimine) (PEI) intermediate layer that showed improved permeation of water in the pervaporation dehydration of isopropyl alcohol (IPA), as compared to TFC membranes on organic supports. Maaskant et al.[22] coated the surface of α-alumina hollow fibers with a layer of γ-alumina nanoparticles to improve the bonding of the PA film to the support. Li et al.[23] and Liu et al.[24] used mesoporous TiO_2 coatings on the alumina hollow fiber surface to the same effect and demonstrated high water permeation and selectivity for nanofiltration based desalination of water and dehydration of IPA, respectively. Thus, the literature suggests that the fabrication of TFC PA membranes on α-alumina hollow fibers will need an intermediate layer that can smooth the surface of the fiber and improve the bonding of the PA film to the support. Another advantage of this intermediate layer has also been suggested to be its storage and release of the diamine in a controlled manner during IP. With the judicious choice of nanomaterial for the smoothing layer for the alumina hollow

fibers, it may also be possible to improve the performance of the resulting TFC membranes even further.

We hypothesized that a thin layer of microporous, high-aspect-ratio nanosheets of zeolite materials may be an ideal intermediate layer for fabricating PA films on α-alumina supports. The high aspect ratio of the nanosheets (1-10 nm thickness and 100-1000 nm in lateral dimension) allows a continuous coating with much greater ease than nanoparticles. The microporous zeolite intermediate layer may considerably improve the water permeance of the overall membrane relative to the mostly nonporous intermediate layer materials that have been used so far. It may also effectively store diamine molecules in the spaces between the zeolite nanosheets prior to IP. Ryoo et al.[25] reported the first instance of crystallization of a multilamellar stack of zeolite MFI nanosheets using an amphiphilic structure-directing agent. Varoon et al.[26] then reported the exfoliation of these MFI nanosheets for the fabrication of ultra-thin MFI membranes for butane and xylene isomer separations. It is important to note that the deposition of MFI nanosheets on various supports created a smooth coating on these supports.[27–30] Similar to multilamellar MFI nanosheets, the synthesis of multilamellar aluminophosphate AEL nanosheets has been reported,[31] though they have been rarely utilized in applications to date. These AEL nanosheets possess the 1D elliptical pores of the AEL framework that are 0.4 nm x 0.65 nm in size and run through the plane of the nanosheet. These AEL nanosheets could be more effective at molecular sieving of water as compared to MFI due to their smaller pore size, while their single unit-cell thickness of 2 nm could help reduce mass transfer limitations, thus enhancing flux. However, the exfoliation of AEL nanosheets has not been reported in literature so far, to the best of our knowledge.

In the above context, the present work is aimed at the fabrication of AEL zeolite nanosheet/PA nanocomposite membranes on the shell side (outer side) of α-alumina hollow fibers. The AEL zeolite nanosheets were exfoliated by a polymer melt blending process[26] and the resulting exfoliated zeolite nanosheets were coated on the shell side of alumina hollow fibers by a vacuum filtration process.[32] The PA film formation was then carried out by an IP process between *m*-phenylenediamine (MPD) and trimesoyl chloride (TMC). The resulting membranes were characterized in detail via XRD, SEM and XPS as well as examined for the pervaporative desalination of brackish water and seawater.

3.2 Experimental Methods

3.2.1 Preparation of α-alumina hollow fibers

The α-Alumina hollow fibers were prepared as reported in our recent work,[32] with the sintering temperature reduced to 1573 K. Similar to the our previous works,[32,33] the composition (wt%) of the spinning dope was 38.0 NMP: 6.8 PES: 54.7 Al_2O_3: 0.5 PVP and the spinning of the hollow fibers was carried out in the in-house apparatus constructed at Georgia Tech. The dope and the bore fluid flow rates were 120 and 80 mL/h respectively, while DI water and tap water were used as the bore fluid and external coagulant fluid respectively. The dope and the water bath were at room temperature and the air gap was 3 cm. The fibers fell freely into the water bath and were collected and soaked in DI water for 3 days (water was changed daily) to exchange the residual solvent, after which they were thoroughly dried. The raw/"green" fibers were then sintered at 873 K for 2 h, followed by ramping to 1573 K for 6 h, with the ramp rate being 5 K/min in both cases. The finished fibers had an OD of 800 μm and wall thickness of 150 μm.

3.2.2 Synthesis of AEL nanosheets

AEL zeolite nanosheets were synthesized as reported by Seo et al.[31] using a surfactant-like amphiphilic tertiary diamine as the structure-directing agent (SDA). For the synthesis of the SDA, 0.01 moles of 1-bromodocosane (TCI America) and 0.1 moles of 1,6-diaminohexane (Sigma-Aldrich) were added to 100 mL of acetonitrile in a 250 mL round-bottom flask. The mixture was stirred at 308 K overnight and the product was precipitated by adding DI water, which was subsequently filtered and washed with plenty of DI water to remove the unreacted diamine. The solid product was dried overnight at room temperature in a fumehood. 2.76 g of this product was added to 12.62 g of 37 wt% fomaldehyde solution in water (EMD Millipore) and 3.85 g of 85 wt% formic acid (Sigma-Aldrich) in a 100 mL round-bottom flask fitted with a condenser. The mixture was stirred at 373 K overnight after which it was cooled down and 10 mL of 7 M aqueous NaOH solution was added to it to neutralize the excess formic acid. The liquid mixture was then transferred to a separating funnel and the product was extracted using 100 mL of diethyl ether. The organic phase (product + ether) was then separated and dried over $MgSO_4$ (Sigma-Aldrich). The diethyl ether was then rotavapped to yield the SDA.

To synthesize the AEL nanosheets, 0.25 g of pseudoboehmite (Catapal Alumina, 75 wt%) was added to 16.27 g of DI water in a 30 mL poly(propylene) bottle with a cap. 0.42 g of 85 wt% phosphoric acid (Sigma-Aldrich) was then added dropwise to the mixture while stirring at 1000 rpm. The mixture was then aged at room temperature while stirring for 8 h followed by the addition of 0.425 g of the SDA. The resulting gel with a composition of 1 Al_2O_3 : 1 P_2O_5 : 500 H_2O : 0.5 SDA was then further aged at room temperature for 2 h followed by hydrothermal treatment at 453 K in a Teflon-lined autoclave tumbling at 60

rpm for 24 h in an oven. The AEL nanosheets were then collected by centrifuging and washing the mixture with DI water 3 times and dried in an oven at 348 K overnight.

3.2.3 Exfoliation of AEL nanosheets

The exfoliation of the multilamellar AEL nanosheets was carried out in a manner similar to that of multilamellar MFI nanosheets reported by Varoon et al.[26] First, 3.84 g of (poly)styrene (Scientific Polymer Products, 45000 MW) was mixed with 0.16 g of as-made AEL nanosheets and added to a twin-screw extruder (HAAKE Minilab). The screw speed was set to 300 rpm and the poly(styrene) – AEL nanosheet mixture was blended sequentially at 393 K for 20 mins, 443 K for 25 mins, 423 K for 30 mins and 493 K for 20 mins. The resulting nanocomposite was then extruded at 423 K. To obtain a suspension of the exfoliated AEL nanosheets that could be used for coating substrates, 0.4 g of the extruded nanocomposite was added to 32 g of toluene in a 50 mL centrifuge tube. The nanocomposite was dissolved by sonication for 1 hour with occasional vortexing to disperse the zeolite nanosheets. The suspension was then centrifuged at 15000 RCF for 20 mins to settle the large, unexfoliated particles. The toluene suspension, except the bottom 10 mL, was then pipetted out and filtered through a 1 μm syringe filter to further purify the suspension and used for coating the alumina hollow fibers.

3.2.4 AEL nanosheet coatings on alumina hollow fibers

The AEL nanosheets were coated on the outer surface of alumina hollow fibers using a setup similar to that used for coating MFI nanosheets in our previous work.[32] One end of a ~9 cm long fiber was sealed with epoxy (3m – DP 100 Translucent) to prevent infiltration of the nanosheet suspension, while the other end was connected to one end of a

PTFE tubing (1/16'') using the same epoxy. The other end of the PTFE tubing was connected to a vacuum pump through Swagelok fittings. This assembly, with the alumina hollow fiber sticking out of the PTFE tubing, was immersed into the exfoliated AEL nanosheet suspension in toluene and vacuum was applied in order to 'filter' the solvent through the macropores of the alumina hollow fiber and deposit the AEL nanosheets on the outer surface. The solvent passing through the fiber was collected in a trap and coating was completed when 20 mL of solvent was collected. The coated fibers were then detached from the PTFE tubing and calcined at 823 K for 6 h with a ramp rate of 2 K/min.

3.2.5 Interfacial polymerization

The PA layer was formed on the AEL nanosheet coated fibers via the IP of *m*-phenylenediamine (MPD) (Sigma-Aldrich) with trimesoyl chloride (TMC) (Sigma-Aldrich). The hollow fiber that was calcined after the AEL nanosheet coating was reattached to the PTFE tubing using epoxy, with one end of the fiber sealed. It was then vertically dipped into a 2 wt% aqueous MPD solution for 5 mins, after which it allowed to dry in ambient conditions for 20 mins. Next, the MPD-soaked fiber was dipped into the TMC solution in hexane (0.3 wt%) for 10 min. The fiber was again dried in ambient conditions for 1 min before being cured in an oven preheated at 343 K for 5 mins. Finally, after 3 hours in ambient conditions, the fibers were washed with 5 mL of methanol and dried overnight in ambient air. These membranes were designated as AEL-TFN. Control samples, with no AEL nanosheet coating (TFC), were prepared in the same manner, except that bare alumina hollow fibers were used for the IP.

3.2.6 Characterization

X-ray diffraction (XRD) patterns were collected on a PANalytical X'Pert Pro MPD diffractometer with CuK_α radiation (45 kV, 40 mA). It was difficult to obtain the XRD pattern of the AEL nanosheet coating on the alumina hollow fibers in the Bragg-Bretano mode due to their curvature. Thus, as an alternative, AEL nanosheets were deposited on a flat alumina disk and these were used to measure the XRD pattern as reported in our previous work.[32] SEM images were obtained on a Hitachi SU-8010 electron microscope operating at 3 kV and 10 μA and the samples were first sputter coated with gold for 45 secs. EDS mapping were done on a Hitachi SU-8230 electron microscope operating at 5 kV and 20 μA. TEM images were obtained on a FEI Tecnai G^2 F30 operating at 300 kV. X-ray photoelectron spectroscopy analysis was conducted on a Thermo K-alpha spectrometer equipped with a Al K_α source.

3.2.7 Pervaporative desalination measurements

The membranes were mounted into home-made modules reported in our previous works[32,34,35] for testing using pervaporative desalination at 298 K. First, 65 mL of aqueous NaCl solution (2 g/L or 36 g/L) was poured into the shell side cavity of the module and the module was sealed. Vacuum (< 50 mTorr) was applied to the bore side to create the driving force for pervaporation. The vapor permeating through the membrane was collected in a trap cooled using liquid nitrogen. The experiment was run for 4 h, where the first 3 h was used to reach a steady state flux, which was determined based on consistent values of flux obtained for 2 consecutive time points (within 5% of each other). The water flux was

calculated based on the mass of permeate collected in the cold traps as shown in the following equation:

$$J = \frac{m}{A\Delta t} \tag{3.1}$$

Where J is the flux in kg/m^{2}h, A is the area of the membrane (1 cm^2), m is the mass of the permeate collected during an operation period of Δt.

The water permeance can be calculated using the flux (J) obtained from Equation 1, by normalizing it based on the pressure driving force as outlined in the following equation:

$$Permeance = \frac{J}{a_W P_{sat,W} - P_P} \tag{3.2}$$

Where a_W is the water activity of the salt solution which was calculated based on the correlation outlined by Miyawaki et al.[36] $P_{sat,W}$ is the saturation pressure of pure water at 298 K and P_P is the permeate side pressure, which is assumed to be zero in our case, due to the application of ultra-high vacuum (<50 mTorr).

The salt rejection is calculated based on the permeate composition using the following equation:

$$Rejection\ (\%) = \frac{C_f - C_p}{C_f} \times 100 \tag{3.3}$$

where C_f and C_p are the salt concentrations of the feed and permeate (condensed in the trap) respectively in g/L. The salt concentrations were calculated based on the

conductivity of the solution measured using a conductivity meter (Hanna Instruments). For the long-term stability experiment, the pervaporation was carried out using the 2 g/L NaCl solution in the same way as described above for 150 h. However, based on the flux of the membrane and the amount of salt solution needed to keep the membrane submerged at all times, the experiment had to be stopped for a short duration every 35 – 36 h to open the membrane module, pipette out the remaining solution and replenish it with fresh salt solution. The experiment would then be resumed with sample collection being done every few hours to measure the flux and rejection.

3.3 Results and Discussion

3.3.1 Synthesis and exfoliation of AEL zeolite nanosheets

The successful synthesis of multilamellar AEL nanosheets was confirmed based on the XRD pattern shown in Figure 3.1, which matches the original report by Seo et al.[31] The XRD pattern for conventional 3D (bulk) AEL is also shown in Figure 3.1 for reference. The reduced intensity of certain peaks in the case of the AEL nanosheets, as compared to conventional AEL, is due to the extreme reduction in the thickness of the crystal along the *c*-direction, which leads to a loss of periodicity along the crystallographic *c*-axis.

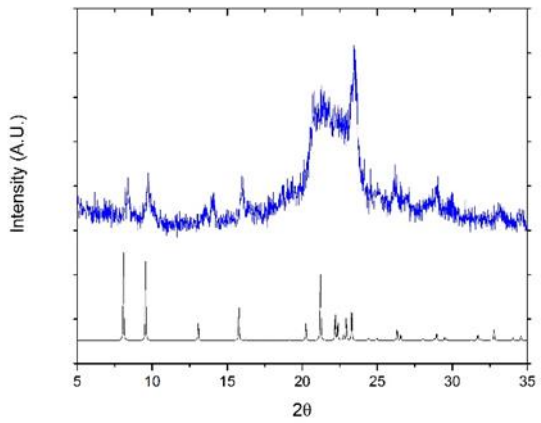

Figure 3.1. XRD pattern of the as-made AEL nanosheets (blue) compared with that of conventional AEL (black)

The exfoliation of the as-made, multilamellar AEL nanosheets was then carried out using the procedure reported for MFI nanosheets by Varoon et al.[26] The TEM images of the exfoliated AEL nanosheet suspension are shown in Figure 3.2. The nanosheets appear well exfoliated and their large aspect ratio is clearly visible (measured lateral dimension of 200-250 nm, expected thickness of 2 nm). There are a few instances where the multilamellar stack of nanosheets are not completely exfoliated as seen in Figure 3.2b. However, these stacks are only 5-10 nanosheet layers thick, which means that the combined thickness is still only 10-20 nm. The pore structure of the AEL framework is also visible (Figure 3.2b) and this is expected since the 10-MR of AEL runs perpendicular to the plane of the nanosheet. This is the first report on the successful exfoliation of aluminophosphate AEL nanosheets to the best of our knowledge. The high aspect ratio and ultra-thin thickness of these exfoliated nanosheets makes them ideal for deposition on a substrate in highly oriented manner.

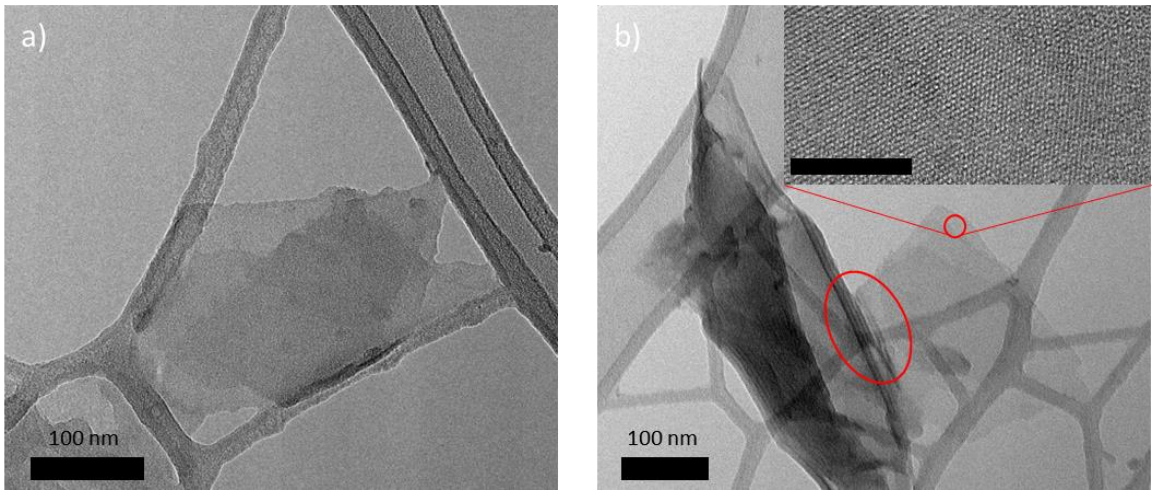

Figure 3.2. a) TEM image of exfoliated AEL nanosheets, b) TEM image showing a partially exfoliated multilamellar stack of AEL nanosheets with 5 nanosheet layers visible in the red ellipse. A magnified image of the exfoliated nanosheet is also shown in the inset with the 1D pores of AEL visible on the nanosheet surface (scale bar in the image is 25 nm)

3.3.2 AEL zeolite nanosheet coating on α-alumina hollow fibers

The exfoliated AEL zeolite nanosheet suspension in toluene was used to vacuum filter the AEL nanosheets on the outer surface of an alumina hollow fiber. The SEM image in Figure 3.3a shows the surface of a bare hollow fiber where the sintered alumina particles are clearly visible. On coating with a 20 mL suspension of exfoliated AEL nanosheets followed by calcination, the surface of the coated fiber looks much smoother with a continuous coating of AEL nanosheets obtained on the surface (Figure 3.3b). The coating was continuous with no bare alumina surface visible and had a uniform thickness of about 300-350 nm (Figure 3.3c). The nanosheets were deposited in a highly oriented manner due to their high aspect ratio and this is confirmed based on the XRD pattern shown in Figure 3.3d, where the (002) peak at 21.2^{o} 2θ is the only peak visible that corresponds to the AEL framework. As a result, the 1D channels of the AEL framework are aligned along the radial direction of the hollow fiber, something which is highly desirable and can facilitate fast

diffusion of molecules. It should be noted that the XRD pattern was obtained by depositing the AEL nanosheets on a flat alumina disk substrate for the ease of analysis, thus overcoming problems associated with measuring x-ray diffraction from a curved fiber surface with a thin coating of AEL sheets on it. Due to the highly oriented deposition of the nanosheets, grazing-angle x-ray measurements (to boost sample signal) are not meaningful either.

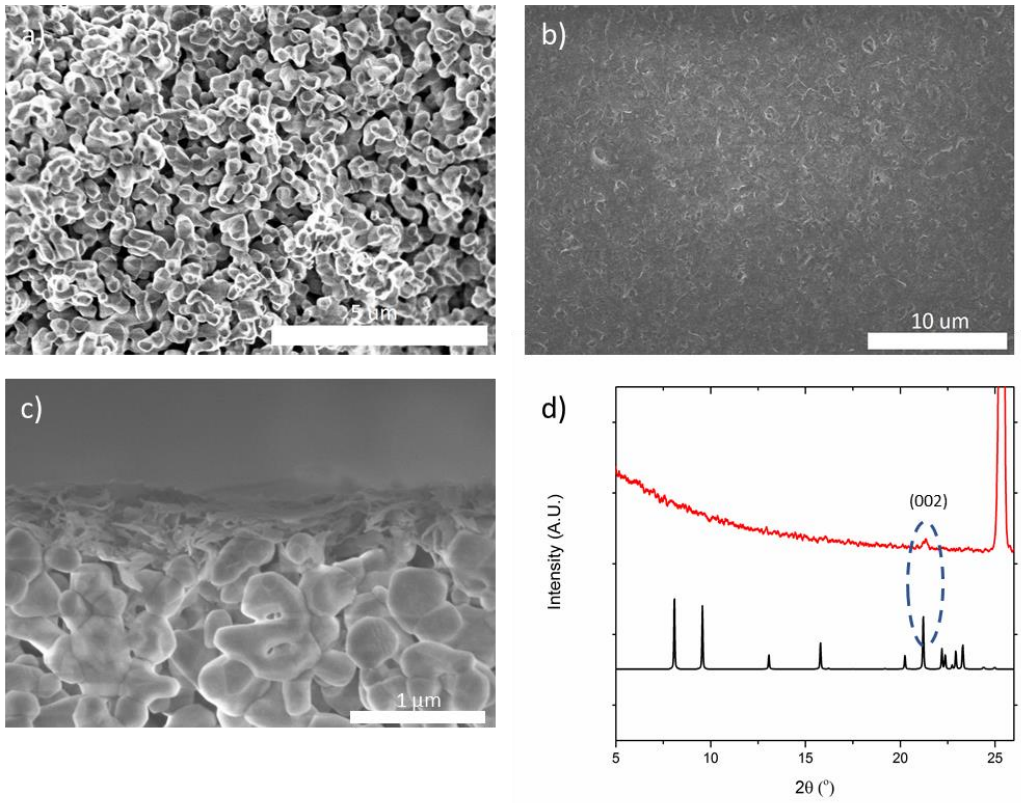

Figure 3.3. SEM images of surface of a bare (a) and AEL nanosheet coated (b) α-alumina hollow fiber; c) Cross-section SEM image of a AEL nanosheet coated fiber; d) XRD pattern of a AEL nanosheet coated alumina disk (top pattern in red) (The alumina peak at 25.59º 2θ has been truncated to show the AEL peak clearly). The XRD pattern of conventional AEL is shown for reference (bottom pattern in black)

3.3.3 Poly(amide) film formation via interfacial polymerization

While the AEL nanosheet coating is continuous, it is still non-selective because of the gaps between the nanosheets. To fill these gaps and to embed the AEL zeolite nanosheets in a polymeric matrix, a PA film was grown via IP. The advantage of the smooth AEL nanosheet coating is that it allows for a continuous PA layer to be formed, as seen in the surface and cross-section SEM images in Figure 3.4a and 3.4b. The surface of the membrane (Figure 3.4a) shows a continuous, defect-free PA layer that is formed over the AEL nanosheet coating, with no AEL nanosheets visible anymore. The need for the nanosheet coating is also apparent from the fact that PA membranes could not be formed on the bare alumina fibers using the same IP process. Based on the analysis of samples made using 3 bare alumina hollow fibers, it was concluded that the PA layer was highly discontinuous with alumina particles visible in the SEM images (Figure B.1). This is not surprising given the previous literature.[21–24]

In previous reports where an intermediate layer was coated onto the substrate before the IP reaction to form the PA film, the PA layer formed exclusively above the nanomaterial layer and did not infiltrate it.[15–17,19,20] The only exception was the case of a CNC intermediate layer[18] in which a clear boundary was not visible between the CNC layer and the PA film. Similarly, there is no clear interface visible between the AEL nanosheet coating and the PA layer in the cross-section of the composite membrane shown in Figure 3.4b. Comparison of Figures 3.3c and 3.4b shows that the composite AEL nanosheet/PA layer (400-500 nm) is thicker than the original nanosheet coating (300-350 nm). Thus, it can be concluded that the PA layer certainly grows on top of the smooth AEL nanosheet coating. To determine whether the PA layer also encapsulates/infiltrates between the AEL

nanosheets, the cross-section of the membrane was analyzed with nitrogen and phosphorus elemental mapping using EDS, as shown in Figure 3.4c. While the elemental mapping signal-to-noise ratio is not ideal due to the low content of nitrogen (from PA) and phosphorus (from AEL) in the thin membrane layer, the strong overlap in nitrogen and phosphorus signals indicates at least a partial infiltration of the polymer layer into the zeolite nanosheet coating layer. Thus, the AEL nanosheet/PA composite membrane can be regarded as a thin-film nanocomposite (TFN) membrane,[7] with the difference that the membrane fabrication did not involve the mixing of the nanomaterial additive into the monomer solution before casting the membrane through IP. The polymer was instead grown with the intention of partially encapsulating the nanomaterial additive (AEL zeolite nanosheets in this case).

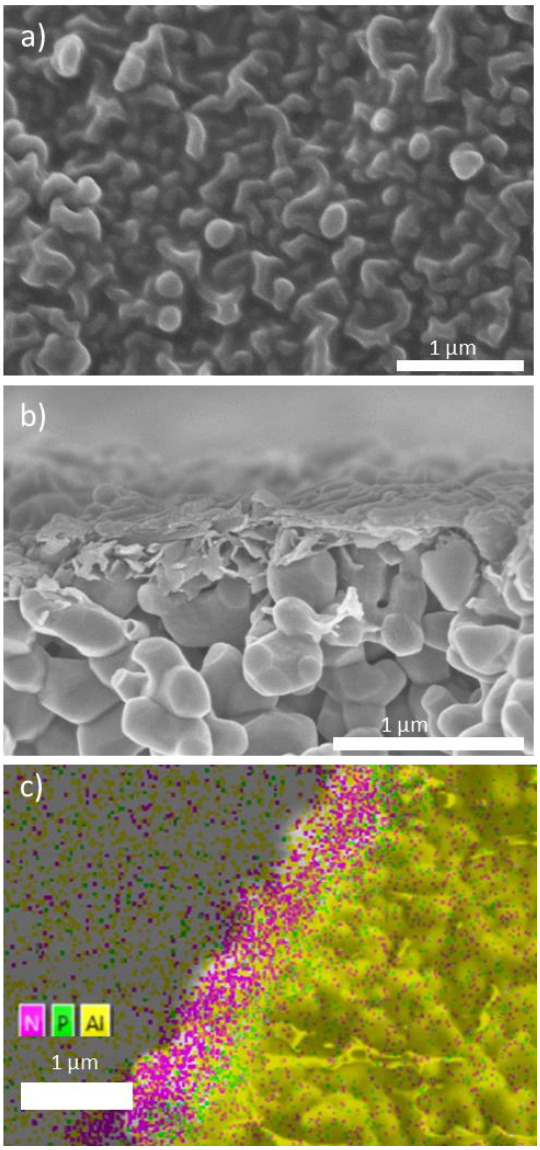

Figure 3.4. SEM images of the surface (a) and cross-section (b) of the AEL nanosheet/PA composite membrane; c) EDS elemental mapping of the cross-section of the AEL nanosheet/PA composite membrane showing overlap of the nitrogen from the PA and phosphorus from the AEL nanosheets

XPS was used to analyze the surface elemental composition of the hollow fibers at each step of the membrane fabrication process. Figure 3.5 shows the XPS spectra obtained for the bare alumina fiber, the fiber coated with AEL nanosheets, and the final AEL nanosheet/PA composite membrane. The bare fiber only shows the Al 2p and O 1s peaks because it is solely α-alumina. After coating the fiber with aluminophosphate AEL

nanosheets, the emergence of the P 2p peak is clearly visible, in addition to the Al 2p and O 1s peaks. Finally, after forming the PA layer, the membrane surface only shows peaks corresponding to C 1s, N 1s and O 1s, indicating complete coverage of the AEL nanosheet coated alumina hollow fiber with the PA layer. Given the low penetration depth of XPS (~5-10 nm), the absence of the Al 2p and P 2p peaks is expected since the PA layer completely covers the AEL nanosheets and the composite layer is thicker than the AEL nanosheet layer, based on the SEM images in Figure 3.4a and Figure 3.4b. XPS analysis also supports the formation of a defective PA layer on a bare alumina hollow fiber since the Al 2p peak is visible in this case (Figure B.2), which comes from exposed alumina particles. Thus, we verified that a bare alumina hollow fiber does not form a continuous PA film after the IP process.

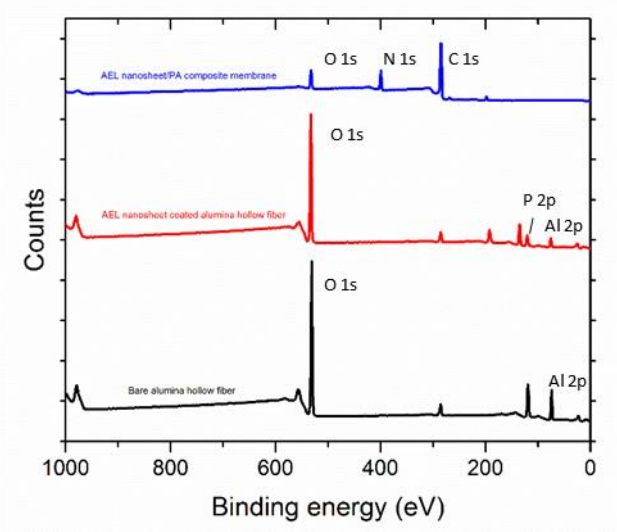

Figure 3.5. XPS survey scans of the bare alumina hollow fiber (black), the AEL nanosheet coated alumina hollow fiber (red) and the AEL nanosheet/PA composite membrane (blue)

Based on the above analyses, a mechanism for the PA film formation on the AEL nanosheet coated hollow fiber is proposed in Figure 3.6. Not only does the AEL nanosheet

coating provide a smooth surface for the PA layer to form, it also acts as a reservoir for the MPD molecules and enables their controlled release during the IP process. Consequently, the AEL nanosheets are partially encapsulated in the PA layer when the reaction between MPD and TMC occurs. This proposed mechanism is also consistent with previous works that involved the deposition of an intermediate layer to reduce the effective pore size of the support layer and act as a storage layer for the diamine molecules while ensuring their controlled release during the IP.[15–18,20,37,38]

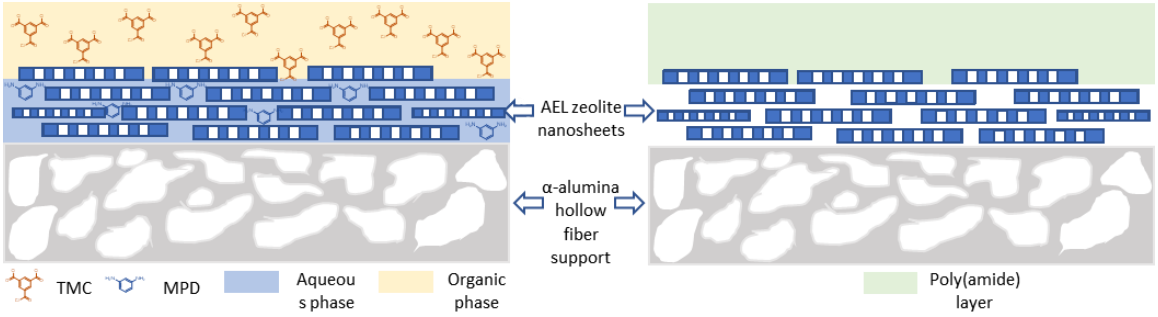

Figure 3.6. Illustration of the proposed mechanism of AEL nanosheet/PA composite membrane formation. After dip-coating in the aqueous phase, the AEL nanosheets act as a reservoir to hold the diamine molecules. Upon dip-coating in the organic phase, the acid chloride molecules start reacting at the interface with the diamine molecules held within the AEL nanosheet layer (left figure). Ultimately, this leads to the formation of the PA layer which ends up partially encapsulating the AEL nanosheet coating (PA layer (green) incorporating some AEL nanosheets in the right figure).

3.3.4 Pervaporative desalination using AEL nanosheet/PA composite membranes

The permeation and separation properties of the AEL nanosheet/PA composite membrane were studied using the example of pervaporative desalination of water at 298 K using two different feed concentrations of NaCl (2 g/L and 36 g/L). The corresponding water fluxes and salt rejections in Figure 3.7 show that the membrane maintains high salt rejection (>99.9%) at both salt concentrations while the water flux drops from 4.27 L.m^{-}

^{2}.h^{-1} to 3.3 L.m^{-2}.h^{-1} as the salt concentration increases from 2 g/L to 36 g/L. Given the high salt rejections, it can be concluded that the AEL nanosheet/PA composite membranes are defect-free. The reduction in water flux with increasing salt concentration is expected since the driving force for water permeation decreases due to the decrease in the activity of water with increasing salt concentration and is consistent with earlier works.[39,40]

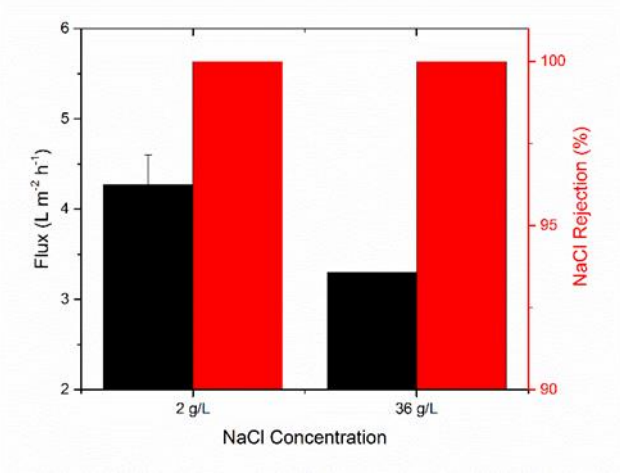

Figure 3.7. Water flux and NaCl rejection for the AEL nanosheet/PA composite membrane at NaCl concentrations of 2 g/L (brackish water) and 36 g/L (seawater).

The enhanced water permeation due to the incorporation of the AEL nanosheets is evident from a comparison of the permeances of the present AEL nanosheet/PA nanocomposite membrane compared with PA-based membranes reported in literature (Table 3.1). The comparisons were made only with reports that introduced an intermediate layer between the support and the PA film, since the permeances reported in these works were the highest. It is clear that the presence of a nanomaterial intermediate layer, AEL nanosheets in this case, leads to a dramatic improvement in the water permeance. An important difference is that the membrane fabricated in this work was tested via pervaporation whereas the other membranes reported earlier were tested via nanofiltration.

This can lead to a significant difference in the salt rejection values (with PV typically yielding much higher rejections due to non-volatility of the salt). However, the permeance values (calculated by dividing the fluxes with the appropriate driving forces) should be comparable across the different permeation methods. In the case of NF, the driving force is the transmembrane pressure differentials, whereas in PV the driving force is defined by Equation 3.2.

Table 3.1. Comparison of the AEL nanosheet/PA nanocomposite membrane with other PA membranes reported in the literature. All results were reported at 298 K/room temperature.

PA monomers	Intermediate layer	Support	Salt solution concentration	Method & conditions	Water permeance (L m^{-2} h^{-1} bar^{-1})	Salt Rejection (%)
PIP + TMC[16]	PDA wrapped SWCNT	PES MF	1 g/L Na_2SO_4	NF, 6 bar, 298 K	32	95.9
PIP + TMC[17]	MWCNT	PES MF	1 g/L Na_2SO_4	NF, 6 bar, 298 K	17.6	95
PIP+TMC[18]	CNC	PES MF	1 g/L Na_2SO_4	NF, 6 bar, 298 K	34	97
PIP+TMC[19]	COF	PES	1 g/L Na_2SO_4	NF, 4 bar, 298 K	31.3	95
PIP + TMC[20]	Tannic acid/Fe^{+3} scaffold	PSF	1 g/L Na_2SO_4	NF, 3.5 bar, 298 K	19.6	95
PEI + TMC[23]	TiO_2	α-alumina hollow fibers	2 g/L $MgCl_2$	NF, 4 bar, 298 K	26.4	95.5
MPD + TMC (This work)	Exfoliated AEL nanosheets	α-alumina hollow fibers	2 g/L NaCl	PV, 298 K	135	>99.99

PES MF – Polyethersulfone microfiltration support; NF – Nanofiltration, PV - Pervaporation

Several factors may be responsible for the high water permeances observed in this work. First, the concept of using an intermediate layer to improve the permeance has been effectively used in this work, especially because the AEL nanosheet interlayer is microporous in nature. The single unit-cell thickness of the exfoliated nanosheets likely further improves the water flux by reducing the diffusion path length. Secondly, the increase in the roughness of the PA film surface likely also led to the improvement in water

permeance due to a higher effective surface area being available for permeation.[41,42] Wang et al.[42] were able to leverage both of these factors in fabricating PA membranes on a PES support with a PDA coated SWCNT intermediate layer. To increase the surface roughness of the PA film to achieve a higher effective surface area, they added ZIF-8 nanoparticles as a sacrificial template that roughened the PA film growing over it and could be removed once the PA film was completely formed. The surface of the AEL nanosheet/PA composite membrane is also quite rough, as seen from the SEM images of the surface at two different magnifications (Figure B.3 and B.4). Lastly, the use of alumina hollow fibers as a substrate for the PA membrane can lead to improved water fluxes in desalination of water because of the high hydrophilicity of alumina.[23]All of these factors act in tandem in this work, leading to the AEL nanosheet/PA composite membrane having an exceptional water permeance of 135 L m^{-2} h^{-1} bar^{-1} (calculated based on the flux for 2 g/L NaCl solution), while maintaining almost complete rejection of the salt. This permeance is 4-9 times higher than prior reports noted in Table 3.1. Recent work by Cao et al.[43] using MFI zeolite nanosheet coatings followed by further crystallization of MFI zeolite between the nanosheets led to the formation of a ultra-thin MFI membrane (<500 nm thickness). This membrane has demonstrated a high flux of 10.4 L m^{-2} h^{-1}(permeance 22 L m^{-2} h^{-1} bar^{-1}), and salt rejections of >99.5% in pervaporative desalination of high-salinity brines (3 wt% NaCl). However, the resulting all-inorganic membranes required an additional high-temperature MFI crystallization step at 190°C to consolidate the membrane, which is not required in the present work.

The on-stream stability of the AEL nanosheet/PA composite membrane was tested by continuous operation of one of the membrane samples for 150 hours with a feed

concentration of 2 g/L NaCl. Because the pervaporation experiment is carried out in a 'batch' mode, wherein 65 mL of salt solution is filled in the shell side cavity of the module used to mount the hollow fiber membrane, the experiment is briefly paused and the feed is replenished at regular intervals (~36 h) to ensure the membrane remains immersed in the feed solution. The result of this modified long-term stability experiment is plotted in Figure 3.8, which shows that the membrane maintains a stable water flux of 4.5 L m^{-2} h^{-1} and a salt rejection of >99.9%. Every time the module is replenished with fresh salt solution, there is a small transient phase, but the system quickly stabilizes. After the experiment, the permeate side (bore side) of the membrane was flushed with 10 mL of DI water and the conductivity of the resultant solution was measured to calculate the amount of salt precicipated on the permeate-side surface during the experiment. It was found that 1.5 mg of salt had passed through the membrane, which is negligible given the duration of the experiment and the amount of permeate collected. However, none of this salt was entrained with the permeating water, given that the permeate was always found to be free of measurable quantities of salt. This result further confirms that the AEL nanosheet/PA nanocomposite membrane is of high quality and defect-free, while delivering high water fluxes and salt rejections.

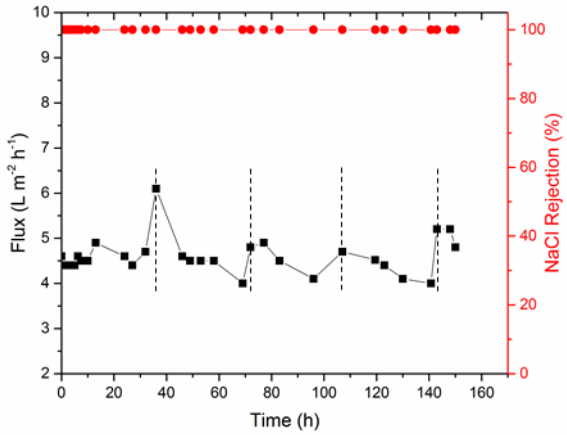

Figure 3.8. On-stream stability of the AEL nanosheet/PA composite membrane tested via pervaporative desalination of 2 g/L NaCl solution at 298 K. The vertical dashed lines indicate the points where the experiment was briefly paused to replenish the salt solution in the testing module.

3.4 Conclusions

Multilamellar AEL nanosheets were successfully exfoliated for the first time using polymer melt blending, and the exfoliated nanosheets were then coated on to the shell side of alumina hollow fibers using a simple vacuum coating process. The AEL nanosheets are deposited in a highly oriented manner and formed a smooth, 300-350 nm thin coating. IP was then carried out to form a PA membrane layer that (at least partially) infiltrated and encapsulated the AEL nanosheet layer, to yield a total composite membrane thickness < 550 nm. We suggest that the AEL coating acts as a reservoir to store the diamine molecules and allow their controlled release during the IP reaction. This AEL nanosheet/PA composite membrane showed high water fluxes of 4.5 L m^{-2} h^{-1} for brackish water (2 g/L NaCl) and 3.3 L m^{-2} h^{-1} for seawater (36 g/L NaCl) with a NaCl rejection of >99.99% in the pervaporative desalination of water. The membrane was also stable during continuous operation for 150 h with no detectable drop in water flux or salt rejection. These results

provide a significant improvement in the water permeances for desalination applications compared to the state-of-the-art PA membranes. This provides a strong motivation to expand the investigation of zeolite nanosheets in the fabrication and application of scalable and high-performance nanocomposite membranes for desalination.

3.5 References

(1) Sholl, D. S.; Lively, R. P. Seven Chemical Separations to Change the World. *Nature* **2016**, *532* (435), 6–9.

(2) Elimelech, M.; Phillip, W. A. The Future of Seawater Desalination: Energy, Technology, and the Environment. *Science (80-.).* **2011**, *333* (6043), 712–717.

(3) Cadotte, J. E. US Patent 4,277,344. **1981**, No. 19.

(4) Lau, W. J.; Ismail, A. F.; Misdan, N.; Kassim, M. A. A Recent Progress in Thin Film Composite Membrane: A Review. *Desalination* **2012**, *287*, 190–199.

(5) Morgan, P. W. Interfacial Polycondensation. 11. Fundamentals of Polymer Formation. *J. Polym. Sci.* **1959**, *327* (September 1958).

(6) Yang, Z.; Guo, H.; Tang, C. Y. The Upper Bound of Thin-Film Composite (TFC) Polyamide Membranes for Desalination. *J. Membr. Sci.* **2019**, *590* (June), 117297.

(7) Jeong, B. H.; Hoek, E. M. V.; Yan, Y.; Subramani, A.; Huang, X.; Hurwitz, G.; Ghosh, A. K.; Jawor, A. Interfacial Polymerization of Thin Film Nanocomposites: A New Concept for Reverse Osmosis Membranes. *J. Membr. Sci.* **2007**, *294* (1–2), 1–7.

(8) Duan, J.; Pan, Y.; Pacheco, F.; Litwiller, E.; Lai, Z.; Pinnau, I. High-Performance Polyamide Thin-Film-Nanocomposite Reverse Osmosis Membranes Containing Hydrophobic Zeolitic Imidazolate Framework-8. *J. Membr. Sci.* **2015**, *476*, 303–310.

(9) Wang, C.; Li, Z.; Chen, J.; Li, Z.; Yin, Y.; Cao, L.; Zhong, Y.; Wu, H. Covalent Organic Framework Modified Polyamide Nanofiltration Membrane with Enhanced Performance for Desalination. *J. Membr. Sci.* **2017**, *523* (July 2016), 273–281.

(10) Kim, H. J.; Choi, K.; Baek, Y.; Kim, D. G.; Shim, J.; Yoon, J.; Lee, J. C. High-Performance Reverse Osmosis CNT/Polyamide Nanocomposite Membrane by Controlled Interfacial Interactions. *ACS Appl. Mater. Interfaces* **2014**, *6* (4), 2819–2829.

(11) Yin, J.; Zhu, G.; Deng, B. Graphene Oxide (GO) Enhanced Polyamide (PA) Thin-Film Nanocomposite (TFN) Membrane for Water Purification. *Desalination* **2016**, *379*, 93–101.

(12) Baroña, G. N. B.; Lim, J.; Choi, M.; Jung, B. Interfacial Polymerization of Polyamide-Aluminosilicate SWNT Nanocomposite Membranes for Reverse Osmosis. *Desalination* **2013**, *325*, 138–147.

(13) Bai, L.; Liu, Y.; Bossa, N.; Ding, A.; Ren, N.; Li, G.; Liang, H.; Wiesner, M. R. Incorporation of Cellulose Nanocrystals (CNCs) into the Polyamide Layer of Thin-Film Composite (TFC) Nanofiltration Membranes for Enhanced Separation Performance and Antifouling Properties. *Environ. Sci. Technol.* **2018**, *52* (19), 11178–11187.

(14) Liu, S.; Low, Z. X.; Hegab, H. M.; Xie, Z.; Ou, R.; Yang, G.; Simon, G. P.; Zhang, X.; Zhang, L.; Wang, H. Enhancement of Desalination Performance of Thin-Film Nanocomposite Membrane by Cellulose Nanofibers. *J. Membr. Sci.* **2019**, *592* (May).

(15) Karan, S.; Jiang, Z.; Livingston, A. G. Sub-10 Nm Polyamide Nanofilms with Ultrafast Solvent Transport for Molecular Separation. *Science (80-.).* **2015**, *348* (6241), 1347–1351.

(16) Zhu, Y.; Xie, W.; Gao, S.; Zhang, F.; Zhang, W.; Liu, Z.; Jin, J. Single-Walled Carbon Nanotube Film Supported Nanofiltration Membrane with a Nearly 10 Nm Thick Polyamide Selective Layer for High-Flux and High-Rejection Desalination. *Small* **2016**, *12* (36), 5034–5041.

(17) Wu, M. B.; Lv, Y.; Yang, H. C.; Liu, L. F.; Zhang, X.; Xu, Z. K. Thin Film Composite Membranes Combining Carbon Nanotube Intermediate Layer and Microfiltration Support for High Nanofiltration Performances. *J. Membr. Sci.* **2016**, *515*, 238–244.

(18) Wang, J. J.; Yang, H. C.; Wu, M. B.; Zhang, X.; Xu, Z. K. Nanofiltration Membranes with Cellulose Nanocrystals as an Interlayer for Unprecedented Performance. *J. Mater. Chem. A* **2017**, *5* (31), 16289–16295.

(19) Zhang, Z.; Shi, X.; Wang, R.; Xiao, A.; Wang, Y. Ultra-Permeable Polyamide Membranes Harvested by Covalent Organic Framework Nanofiber Scaffolds: A Two-in-One Strategy. *Chem. Sci.* **2019**, *10* (39), 9077–9083.

(20) Yang, Z.; Zhou, Z. W.; Guo, H.; Yao, Z.; Ma, X. H.; Song, X.; Feng, S. P.; Tang, C. Y. Tannic Acid/Fe3+ Nanoscaffold for Interfacial Polymerization: Toward Enhanced Nanofiltration Performance. *Environ. Sci. Technol.* **2018**, *52* (16), 9341–9349.

(21) Shi, G. M.; Chung, T. S. Thin Film Composite Membranes on Ceramic for Pervaporation Dehydration of Isopropanol. *J. Membr. Sci.* **2013**, *448*, 34–43.

(22) Maaskant, E.; Wit, P. De; Benes, N. E. Direct Interfacial Polymerization onto Thin Ceramic Hollow Fi Bers. *J. Membr. Sci.* **2018**, *550* (January), 296–301.

(23) Li, Y. X.; Cao, Y.; Wang, M.; Xu, Z. L.; Zhang, H. Z.; Liu, X. W.; Li, Z. Novel High-Flux Polyamide/TiO2 Composite Nanofiltration Membranes on Ceramic Hollow Fibre Substrates. *J. Membr. Sci.* **2018**, *565* (November 2017), 322–330.

(24) Liu, X.; Cao, Y.; Li, Y.; Xu, Z.; Li, Z.; Wang, M.; Ma, X. High-Performance Polyamide / Ceramic Hollow Fiber TFC Membranes with TiO2 Interlayer for Pervaporation Dehydration of Isopropanol Solution. *J. Membr. Sci.* **2019**, *576* (January), 26–35.

(25) Choi, M.; Na, K.; Kim, J.; Sakamoto, Y.; Terasaki, O.; Ryoo, R. Stable Single-Unit-Cell Nanosheets of Zeolite MFI as Active and Long-Lived Catalysts. *Nature* **2009**, *461* (7261), 246–249.

(26) Kumar Varoon,* Xueyi Zhang,* Bahman Elyassi, Damien D. Brewer, M. G.; Sandeep Kumar,‡ J. Alex Lee,§ Sudeep Maheshwari,|| Anudha Mittal, C.-Y. S.; Matteo Cococcioni, Lorraine F. Francis, Alon V. McCormick, K. Andre Mkhoyan, M. T. Dispersible Exfoliated Zeolite Nanosheets and Their Application as a Selective Membrane. *Science (80-.).* **2011**, *734* (October), 72–76.

(27) Agrawal, K. V.; Topuz, B.; Cao, T.; Pham, T.; Nguyen, T. H.; Sauer, N.; Rangnekar, N.; Zhang, H.; Narasimharao, K.; Basahel, S. N.; Francis, L. F.; Macosko, C. W.; Al-thabaiti, S.; Tsapatsis, M.; Yoon, K. B. Oriented MFI Membranes by Gel-Less Secondary Growth of Sub-100 Nm MFI-Nanosheet Seed Layers. **2015**, 3243–3249.

(28) Kumar Varoon Agrawal, Berna Topuz, Zheyu Jiang, Kevin Nguenkam, Bahman Elyassi, Lorraine F. Francis, and M. T. Solution-Processable Exfoliated Zeolite Nanosheets Purified by Density Gradient Centrifugation. *AIChE J.* **2013**, *59* (9), 3458–3467.

(29) Rangnekar, N.; Shete, M.; Agrawal, K. V.; Topuz, B.; Kumar, P.; Guo, Q.; Ismail, I.; Alyoubi, A.; Basahel, S.; Narasimharao, K.; Macosko, C. W.;

Mkhoyan, K. A.; Al-Thabaiti, S.; Stottrup, B.; Tsapatsis, M. 2D Zeolite Coatings: Langmuir-Schaefer Deposition of 3 Nm Thick MFI Zeolite Nanosheets. *Angew. Chemie - Int. Ed.* **2015**, *54* (22), 6571–6575.

(30) Zhang, H.; Xiao, Q.; Guo, X.; Li, N.; Kumar, P.; Rangnekar, N.; Jeon, Y.; Al-thabaiti, S.; Narasimharao, K.; Basahel, S. N.; Topuz, B.; Onorato, F. J.; Macosko, C. W.; Mkhoyan, K. A.; Tsapatsis, M. Open-Pore Two-Dimensional MFI Zeolite Nanosheets for the Fabri- Cation of Hydrocarbon-Isomer-Selective Membranes on Porous Poly- Mer Supports. **2016**, 1–5.

(31) Seo, Y.; Lee, S.; Jo, C.; Ryoo, R. Microporous Aluminophosphate Nanosheets and Their Nanomorphic Zeolite Analogues Tailored by Hierarchical Structure-Directing Amines. *J. Am. Chem. Soc.* **2013**, *135* (24), 8806–8809.

(32) Min, B.; Yang, S.; Korde, A.; Kwon, Y. H.; Jones, C. W.; Nair, S. Continuous Zeolite MFI Membranes Fabricated from 2D MFI Nanosheets on Ceramic Hollow Fibers. *Angew. Chemie - Int. Ed.* **2019**, *58* (24), 8201–8205.

(33) Yang, S.; Kwon, Y. H.; Koh, D. Y.; Min, B.; Liu, Y.; Nair, S. Highly Selective SSZ-13 Zeolite Hollow Fiber Membranes by Ultraviolet Activation at Near-Ambient Temperature. *ChemNanoMat* **2019**, *5* (1), 61–67.

(34) Brown, A. J.; Brunelli, N. A.; Eum, K.; Rashidi, F.; Johnson, J. R.; Koros, W. J.; Jones, C. W.; Nair, S. Interfacial Microfluidic Processing of Metal-Organic Framework Hollow Fiber Membranes. *Science (80-.).* **2014**, *345* (6192), 72–75.

(35) Eum, K.; Ma, C.; Koh, D. Y.; Rashidi, F.; Li, Z.; Jones, C. W.; Lively, R. P.; Nair, S. Zeolitic Imidazolate Framework Membranes Supported on Macroporous Carbon Hollow Fibers by Fluidic Processing Techniques. *Adv. Mater. Interfaces* **2017**, *4* (12), 1–6.

(36) Miyawaki, O.; Saito, A.; Matsuo, T.; Nakamura, K. Activity and Activity Coefficient of Water in Aqueous Solutions and Their Relationships with Solution Structure Parameters. *Biosci. Biotechnol. Biochem.* **1997**, *61* (3), 466–469.

(37) Gong, G.; Wang, P.; Zhou, Z.; Hu, Y. New Insights into the Role of an Interlayer for the Fabrication of Highly Selective and Permeable Thin-Film Composite Nanofiltration Membrane. *ACS Appl. Mater. Interfaces* **2019**, *11* (7), 7349–7356.

(38) Zhou, Z.; Hu, Y.; Boo, C.; Liu, Z.; Li, J.; Deng, L.; An, X. High-Performance Thin-Film Composite Membrane with an Ultrathin Spray-Coated Carbon Nanotube Interlayer. *Environ. Sci. Technol. Lett.* **2018**, *5* (5), 243–248.

(39) Liang, B.; Li, Q.; Cao, B.; Li, P. Water Permeance, Permeability and Desalination Properties of the Sulfonic Acid Functionalized Composite Pervaporation Membranes. *Desalination* **2018**, *433* (January), 132–140.

(40) Wu, D.; Gao, A.; Zhao, H.; Feng, X. Pervaporative Desalination of High-Salinity Water. *Chem. Eng. Res. Des.* **2018**, *136*, 154–164.

(41) Tan, Z.; Chen, S.; Peng, X.; Zhang, L.; Gao, C. Polyamide Membranes with Nanoscale Turing Structures for Water Purification. *Science (80-.).* **2018**, *360* (6388), 518 LP – 521.

(42) Wang, Z.; Wang, Z.; Lin, S.; Jin, H.; Gao, S.; Zhu, Y.; Jin, J. Nanoparticle-Templated Nanofiltration Membranes for Ultrahigh Performance Desalination. *Nat. Commun.* **2018**, *9* (1).

(43) Cao, Z.; Zeng, S.; Xu, Z.; Arvanitis, A.; Yang, S.; Gu, X.; Dong, J. Ultrathin ZSM-5 Zeolite Nanosheet Laminated Membrane for High-Flux Desalination of Concentrated Brines. *Sci. Adv.* **2018**, *4* (11), 1–11.

CHAPTER 4. SYNTHESIS AND CHARACTERIZATION OF SINGLE-WALLED NANOTUBES WITH ZEOLITIC WALLS

TEM imaging for the data presented in this chapter was done by Byunghyun Min.

4.1 Introduction

Zeolites have been widely used in the petrochemical industry as size- and shape-selective catalysts and adsorbents, because of their ordered microporous structure.[1–3] In recent years, there has been large interest in the synthesis of hierarchical zeolites that include mesoporosity in addition to the micropores.[4–6] Such materials include either 2D zeolite nanosheets that are pillared to create interlayer mesoporous spaces, or bulk zeolite particles in which mesoporosity is generated by different techniques. The interconnected nature of the micropores and mesopores allows diffusion of bulky molecules to the zeolite interior, creates surface sites with different adsorptive and catalytic environments than in the bulk crystals. In the earliest approaches for hierarchical zeolite synthesis, conventional bulk zeolite crystals are subjected to post-synthetic treatments such as desilication[7] and dealumination[8] that etch away parts of the zeolite crystal and create mesopores, thus creating "hierarchical 3D zeolites". While these top-down techniques are economical and scalable, they lead to the loss of framework atoms and zeolite crystallinity.[9] In more recent approaches, new structure directing agents (SDAs) are used to create the combined microporous-mesoporous architecture of the hierarchical zeolites.[10–16] Such strategies result in the formation of "hierarchical 2D zeolites" wherein the microporosity is in the form of 2D zeolite nanosheets.

While the latter approach has shown much potential to create new hierarchical zeolitic materials, synthesizing combined microporous-mesoporous zeolite systems is quite challenging due to the complex interactions between the zeolite precursors and the organic structure directing agents (SDAs) in hydrothermal environments.[6,17] Choi et al.[11] synthesized a multilamellar, mesostructured MFI zeolite nanosheet with a single unit-cell crystal thickness. This was achieved using a diquaternary ammonium surfactant as a structure directing agent (SDA) that could form a micellar assembly in solution due to its amphiphilic nature. The quaternary ammonium groups directed the crystallization of the MFI framework whereas the long alkyl chain disrupt the crystal growth in the third dimension, yielding MFI nanosheets. A rational design of the SDA by Luo et al.[18] enabled the crystallization of multilamellar MWW nanosheets in a one-pot, bottom-up manner. The SDA consisted of the conventional templating species for crystallizing MWW zeolite (N,N,N trimethyladamantylammonium hydroxide) and a long alkyl hydrophobic chain, the two being connected by a quaternary ammonium linker. The hypothesis was that the hydrophilic headgroup of the SDA directed the crystallization of the zeolite framework whereas the hydrophobic part retarded the growth of the crystal along the third dimension. On the other hand, Che et al.[12,19–23] exploited π-stacking of surfactant molecules containing aromatic groups in their hydrophobic portion, to template lamellar MFI zeolites with different hierarchical structures. The π-stacking of the aromatic groups enables the self-assembly of the SDA molecules into stable hydrophobic lamellae that allow 2D zeolite formation on their surfaces but block crystal growth in the perpendicular direction. While these specially designed SDAs allow the crystallization of ultra-thin zeolite sheets, the morphology of the material can change after calcination (to remove the SDA). In cases

where the zeolite crystallizes as a multilamellar stack of nanosheets, the mesoporous structure collapses and the individual nanosheets undergo partial condensation after calcination.[11,12,22,24] Maintaining the mesoporous structure after the calcination of the SDA is quite challenging and there are only a few successful cases.[14,15,20]

In this work, we report the first synthesis and structural characterization of a "one-dimensional (1D) hierarchical zeolite", in particular, the synthesis of single-walled nanotubes that have a zeolitic microporous wall enclosing a single central mesoporous channel. To synthesize such materials, we speculated that long-chain SDAs containing aromatic (□-stacking) groups at their centers could also be capable of templating the central mesoporous channel, with the analogy that many conventional surfactants are capable of stacking into lamellar as well as rod-like micelles under different conditions. Furthermore, we speculated that the attachment of SDA head-groups to the central groups using sufficiently long and flexible alkyl chain connectors would allow formation of a cylindrical zeolitic wall enclosing the central channel. Accordingly, we synthesized a new bolaform SDA, BCPh10Qui (Figure 4.1), which is capable of π-stacking due to presence of central biphenyl rings and has hydrophilic quinuclidinium headgroups at either end linked to the biphenyl groups by C_{10} alkyl chains. This SDA was used for hydrothermal synthesis in an aluminosilicate precursor medium. The material resulting from the hydrothermal zeolite growth using this SDA was characterized in detail by TEM, SEM, XRD, N_2 physisorption, FT-IR, solid-state NMR, UV/Vis spectroscopy and thermogravimetric analysis (TGA). These characterizations provided insights into the morphology and zeolitic character of the material, as well as the crystallization process.

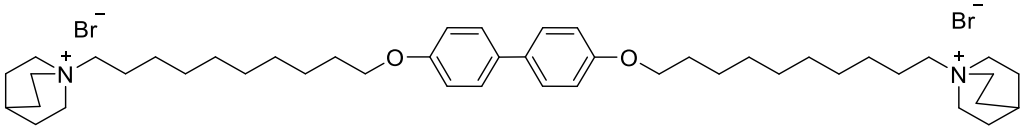

Figure 4.1. Molecular structure of SDA BCPh10Qui

4.2 Experimental Methods

4.2.1 Synthesis of SDA (BCPh10Qui)

The SDA BCPh10Qui was synthesized via a two-step reaction. The first reaction was carried out as reported by Che et al.[12] where 1.6 g of 4,4'-biphenol (Sigma-Aldrich), 1 g of potassium hydroxide (Sigma-Aldrich) and 12.5 g of 1,10-dibromodecane (Sigma-Aldrich) was added to 100 mL of ethanol (200 proof, Koptec) and refluxed overnight under a nitrogen atmosphere. The resultant solid after cooling the reaction was filtered and washed with copious hot ethanol and water to obtain the intermediate, BCPh10Br. 0.5 g of this intermediate product and 0.35 g of quinuclidine (Alfa-Aesar) was added to 25 mL of acetonitrile and refluxed overnight. After cooling the reaction mixture, diethyl ether was added to precipitate the product, BCPh10Qui, which was then filtered and washed with diethyl ether to remove the unreacted reactants. For the scale-up of the SDA synthesis, running the reaction for longer duration with a lower excess of the 1,10-dibromodecane can be considered.

4.2.2 Synthesis of zeolite nanotubes

0.113 g of the SDA BCPh10Qui was added to 4.45 g of DI H_2O in a 30 mL polypropylene bottle with a cap while stirring. After the mixture homogenized, 0.067 g of sodium hydroxide (Sigma-Aldrich) was added and allowed to dissolve. This was followed

by sequential addition of 0.027 g of Aluminum sulfate hydrate ($Al_2(SO_4)_3.14\text{-}18H_2O$, Sigma-Aldrich) and 0.5 g of Ludox HS-30 colloidal silica (Sigma-Aldrich), dropwise. The resulting gel composition of the mixture was 1.875 SiO_2 : 0.03 Al_2O_3 : 1 SDA : 0.63 Na_2O : 205 H_2O. The gel was aged at room temperature while stirring for 3 h with the cap of the polypropylene bottle closed, followed by a static hydrothermal reaction at 423 K for 7 days in Teflon-lined autoclaves. The resulting solid product was collected and washed with DI H_2O by centrifuging 3 times followed by drying in an oven at 348 K. The material was calcined at 823 K for 6 h in air under static conditions with a ramp rate of 2 K/min.

4.2.3 Characterization

XRD patterns were measured on powder samples using a PANalytical X'Pert Pro MPD diffractometer with CuK_α radiation (45 kV, 40 mA). SEM images were obtained using a Hitachi SU8010 electron microscope operating at 3 kV and 10 μA while TEM images were obtained using a FEI Tecnai G^2 F30 operating at 300 kV. Nitrogen physisorption isotherms were obtained using ASAP 2020 (Micromeritics) at 77 K. Prior to the isotherm measurement, the material was activated at 423 K under high vacuum for 12 h. The BET surface area was calculated using the adsorption data obtained at P/P_o between 0.1 and 0.3. The micropore size distribution was calculated using the Horvath-Kawazoe equations while the mesopore size distribution was calculated using the BJH method. FT-IR spectra were obtained on a Thermo Scientific Nicolet 6700 spectrometer equipped with a diamond Smart Orbit ATR accessory. UV-Vis diffuse reflectance spectra were obtained using a Cary 5000 UV-Vis/NIR spectrophotometer. The diffuse reflectance spectra were converted into absorbance spectra using a Kubelka-Munk transformation. Thermogravimetric analyses were carried out on a Netzsch STA 409 PG. The sample mass

loss was recorded while it was heated from room temperature to 1123 K at a ramp rate of 10 K/min. CHN and Si, Al, Na elemental analyses were performed by Galbraith Laboratories Inc. using the combustion method and ICP-OES respectively. Solid state NMR spectra were measured on a Bruker Avance III 400 spectrometer.

4.3 Results and Discussion

The formation of nanotubes is apparent from the TEM images shown in Figure 4.2. While Figures 4.2a-4.2b show individual strands of the as-made 1D material at low magnifications, Figures 4.2c-4.2d clearly show cross-sections of the calcined nanotube bundles at higher magnifications. The latter images also indicate that the central channel is mesoporous with a ~3 nm pore size while the outer diameter of the nanotube is ~5 nm (*i.e.*, the wall of the nanotube is ~ 1 nm thick). The presence of other materials such as 3D or 2D zeolites was not observed in the samples. Figure 4.3 summarizes the textural properties of the calcined nanotubes as studied by high-resolution N_2 physisorption at 77 K, with the properties of a conventional medium pore-size MFI zeolite also shown for comparison. The isotherm (Figure 4.3a) of the nanotube material clearly shows the presence of both micropores and mesopores, indicating the nanotube walls are microporous. The sharp increase in the quantity adsorbed for $P/P_o < 0.1$ is characteristic of micropore adsorption while the increase in the $0.3 < P/P_o < 0.6$ is due to the condensation of N_2 in the mesopores of the nanotubes. This contrasts with the Type I isotherm obtained for a purely microporous MFI zeolite. The nanotubes also possess a very high BET surface area of 980 m^2/g as compared to only 410 m^2/g for conventional MFI. The pore size of the nanotube channel is estimated by the mesopore size distribution, calculated using the BJH method from the adsorption branch of the isotherm (Figure 4.3b). The mesopore size distribution has a

narrow peak at 2.5 nm, which suggests the presence of channels of uniform pore size in the nanotube material. The slight deviation from the value measured in the TEM images (~3 nm) may be attributed to the underestimation of mesopore sizes by the BJH method.[25] The micropore size distribution of the nanotubes is calculated using the Horvath-Kawazoe method, and compared with that of conventional MFI calculated using the same method (Figure 4.3c). Both micropore size distributions show a peak at 0.51 nm, indicating that the nanotube walls have a medium pore size zeolitic structure.

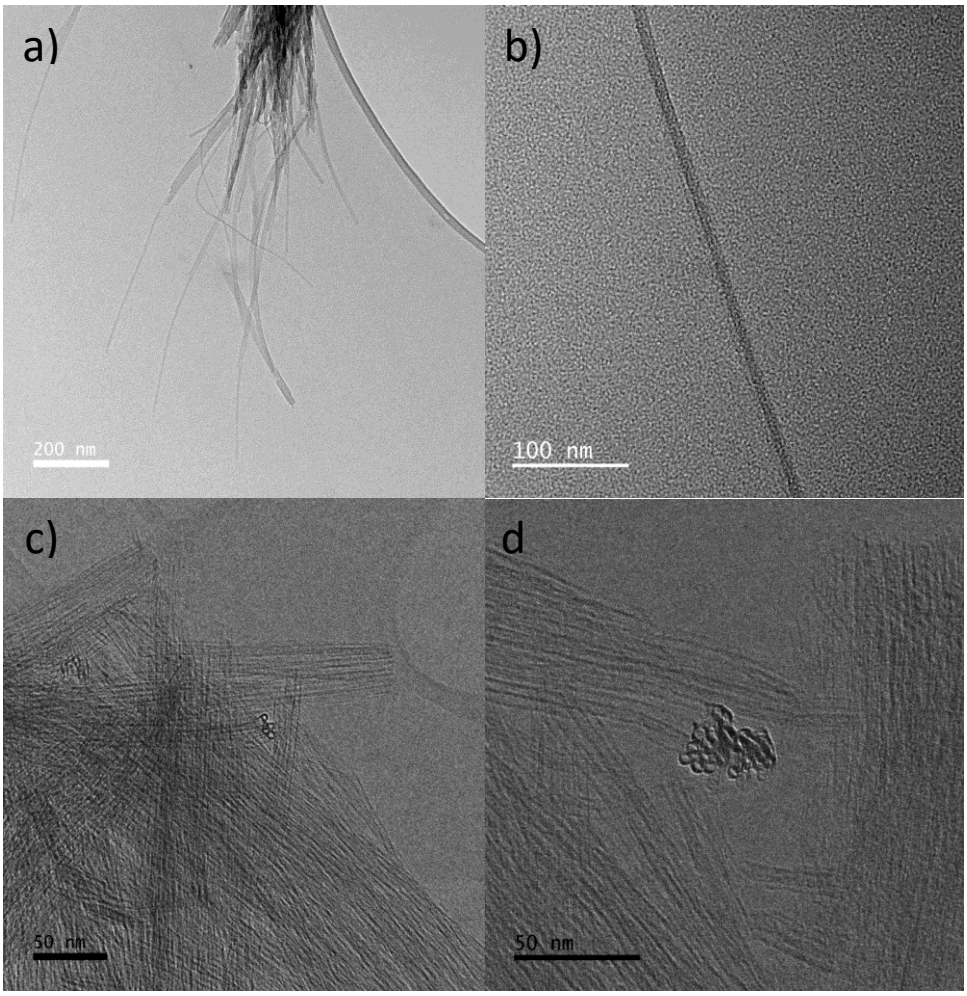

Figure 4.2. TEM images of the nanotube material: (a)-(b) as-made nanotube strands at low magnification, and (c)-(d) calcined nanotube bundle cross-sections.

a)

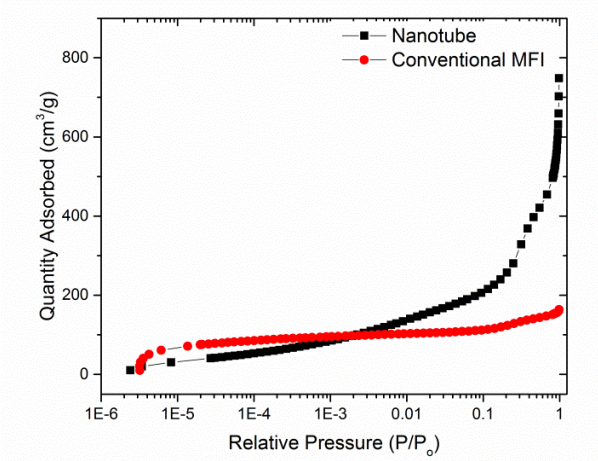

b)

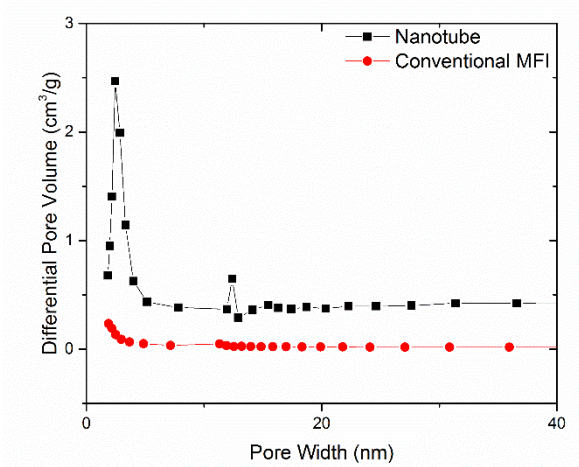

c)

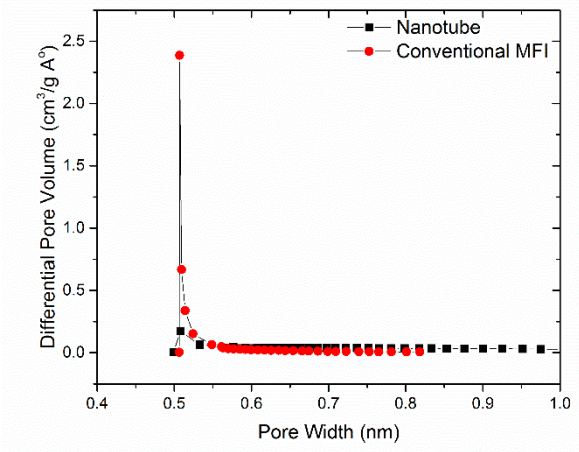

Figure 4.3. a) Nitrogen physisorption isotherms, b) Mesopore and c) micropore size distributions of nanotubes and conventional MFI zeolite (for comparison)

Figure 4.4 shows the low-angle and wide-angle XRD patterns of the calcined nanotube material. As shown by Kang et al.[26,27] for imogolite nanotubes, the low-angle XRD patterns of nanotube powder samples are usually dominated by scattering from individual nanotubes and bundles of nanotubes. The XRD pattern of the material can be attributed to the product of the form factor of the nanotubes by the structure factor of their bundling. The first peak position is approximately equal to the outer diameter of the individual nanotubes, and there are subsequent higher-order peaks. The first peak position of 4.2 nm observed in Figure 4.4a is quite consistent with the TEM and N_2 physisorption observations. The peaks in the wide-angle XRD pattern (Figure 4.4b) indicate atomic-scale ordering in the nanotube walls and show that they are crystalline. However, the thin (~ 1 nm) nanotube walls, and their surface curvature into a cylinder, will lead to XRD patterns that cannot be reliably compared to those of 3D bulk (and 2D nanosheet) zeolites even if the nanotube wall structure matches any known structure.[28–30] This makes it challenging to determine the structure of nanotubes from powder x-ray crystallography alone.

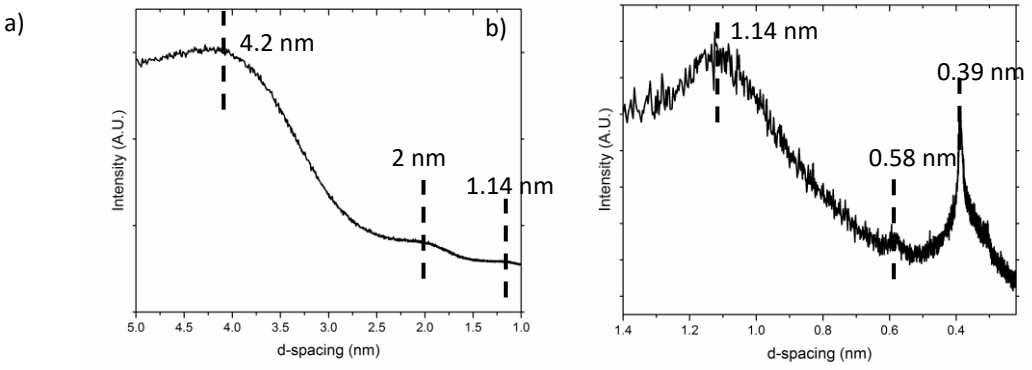

Figure 4.4. a) Low-angle and b) Wide-angle XRD patterns for the calcined nanotubes.

Figure 4.5a shows the FT-IR spectra obtained for the as-made as well as calcined nanotubes and the pure SDA, while Figure 4.5b shows the comparison of the FT-IR spectra of several other 3D and 2D zeolites with different pore sizes (BEA, 3D conventional MFI, 2D MFI and CHA). In Figure 4.5a, the peaks from the SDA are visible in the spectrum of the as-made nanotubes, and disappear upon calcination. Peaks at ~1225 cm^{-1} and ~ 550 cm^{-1} are clearly present in the as-made nanotubes. These peaks somewhat broaden in the calcined sample, but are nevertheless clearly visible. On comparing the FT-IR spectrum of the calcined nanotubes with other frameworks (Figure 4.5b), it can be seen that these peaks are present in zeolites containing five-membered rings (5 MR). The MFI framework (conventional 3D MFI as well as 2D MFI nanosheets) shows distinct peaks at ~1225 cm^{-1} and ~550 cm^{-1} arising from the five-membered pentasil units.[31–34] Similarly, the BEA framework has FT-IR stretches at ~1225 cm^{-1} and 524 cm^{-1} as well as 577 cm^{-1}. The peak around 550 cm^{-1} (550 cm^{-1} for MFI, 524 cm^{-1} and 577 cm^{-1} for BEA) is attributed to the double five-membered rings, while the peak at ~1225 cm^{-1} is a result of the external asymmetric stretching vibration of five-membered ring chains.[31–35] Figure 4.5b also shows that the zeolite framework of the nanotubes is very distinct from that of CHA, and consequently, the building units of CHA, since the FT-IR peaks are quite distinct. Thus, it can be concluded with reasonable certainty that the framework of the zeolite nanotubes is constructed, at least in part, from 5 MR units.

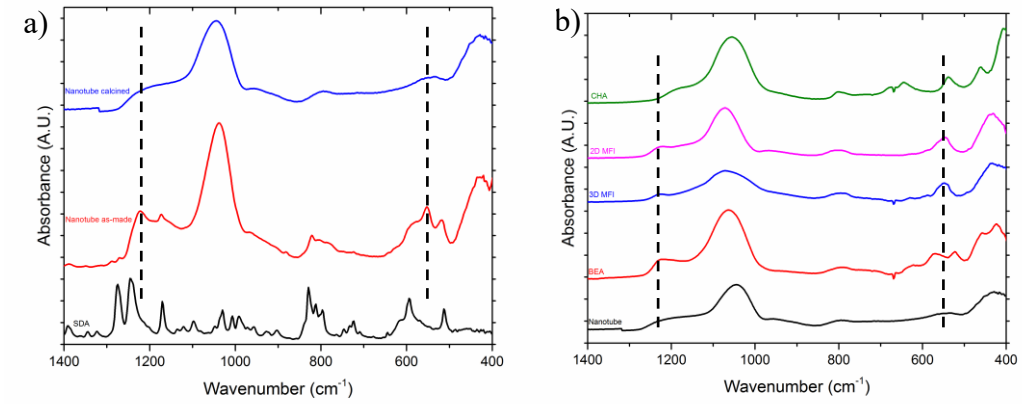

Figure 4.5. a) FT-IR spectra of the solid SDA, the as-made and calcined nanotubes. b) Comparison of FT-IR spectra of several zeolite materials.

The ^{29}Si NMR spectra of the as-made and calcined nanotubes are shown in Figure 4.6. The spectrum of the as-made nanotubes shows three peaks at -99 ppm (Q^3), -106.6 ppm (Q^4 3Si,1Al) and -113.3 ppm (Q^4 4Si). The Q^3 signals are from the Si atoms on the wall surfaces that are presumably terminated by Si-OH groups, and the Q^4 signals are from Si atoms in the interior of the wall. Based on the peak areas, the Si/Al ratio calculated using the method proposed by Klinowski et al.[36] is about 16. The fraction of Q^3 Si atoms is calculated to be 0.15, which is similar to that of 2D zeolite sheets with nearly single-unit-cell thicknesses.[37,38] The calcined nanotubes show peaks at -102 ppm (Q^3) and -110 ppm (Q^4), which leads to a Q^3 fraction of 0.17 based on the peak areas. This value is similar to that of the as-made nanotubes, indicating that there is no significant condensation of surface silanols after calcination. The bonding environment of aluminum in the nanotubes was studied using ^{27}Al NMR (Figure 4.7). Both the as-made and calcined nanotubes show a single peak at 54 ppm that corresponds to tetrahedral aluminum. There was no evidence of octahedral or extra-framework aluminum.

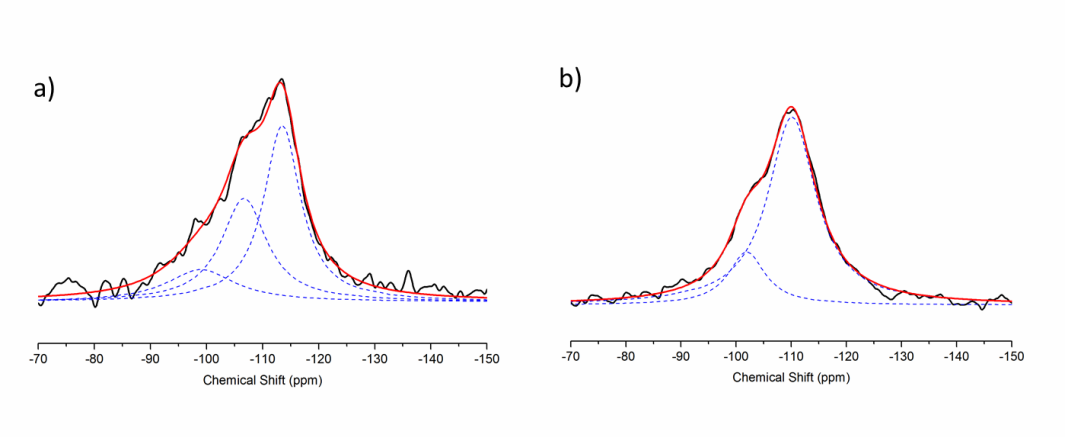

Figure 4.6. ^{29}Si MAS NMR spectra of the a) as-made and b) calcined nanotubes. Black curve is the acquired signal. Blue dotted curves are the fitted deconvoluted peaks (Lorentzians) and the red curve is the overall fit based on the deconvolution.

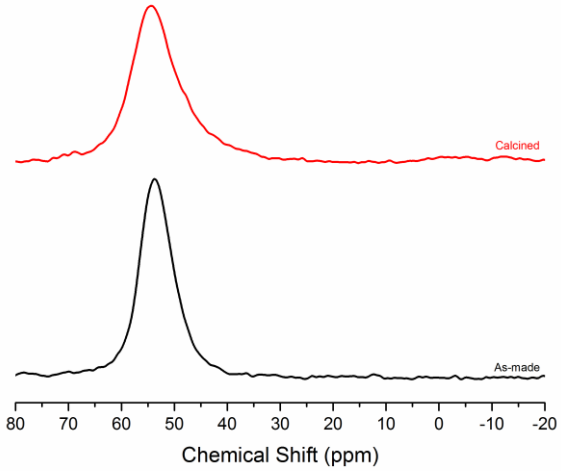

Figure 4.7. ^{27}Al MAS NMR spectra of the as-made and calcined nanotubes.

In order to better understand the formation process of the nanotubes, the duration of the synthesis was varied and the as-made material in each case was analyzed through XRD for crystallinity and through TEM to visualize the growth process. The same gel composition was used for the synthesis with the hydrothermal growth being carried out at 150^{o}C with the only difference being that the hydrothermal growth was stopped after 1

day, 3 days, 5 days and 7 days. Figure 4.8 shows the XRD patterns for the material collected at these times, whereas Figure 4.9 shows corresponding TEM images. The low-angle XRD patterns show early development of mesopore domains which does not change significantly with time. The wide-angle XRD patterns show the evolution of the nanotube wall structure from amorphous to an ordered zeolitic stucture. These observations are consistent with the TEM images, where the mesoporosity of the material is clearly visible at an early stage. The emergence of a few proto-nanotubes is also visible at 3 days (Figure 4.9b), and the nanotubes are fully crystallized by 7 days. Thus, the overall mechanism of growth of the zeolite nanotubes appears to occur in a manner similar to 2D zeolite nanosheets, *i.e.*, initial formation of a mesophase followed by transformation to an ordered zeolitic mature.[39] However, a key difference is in the morphology-directing effect of the SDA, which creates a unique 1D nanotubular material in the present case rather than a 2D nanosheet material.

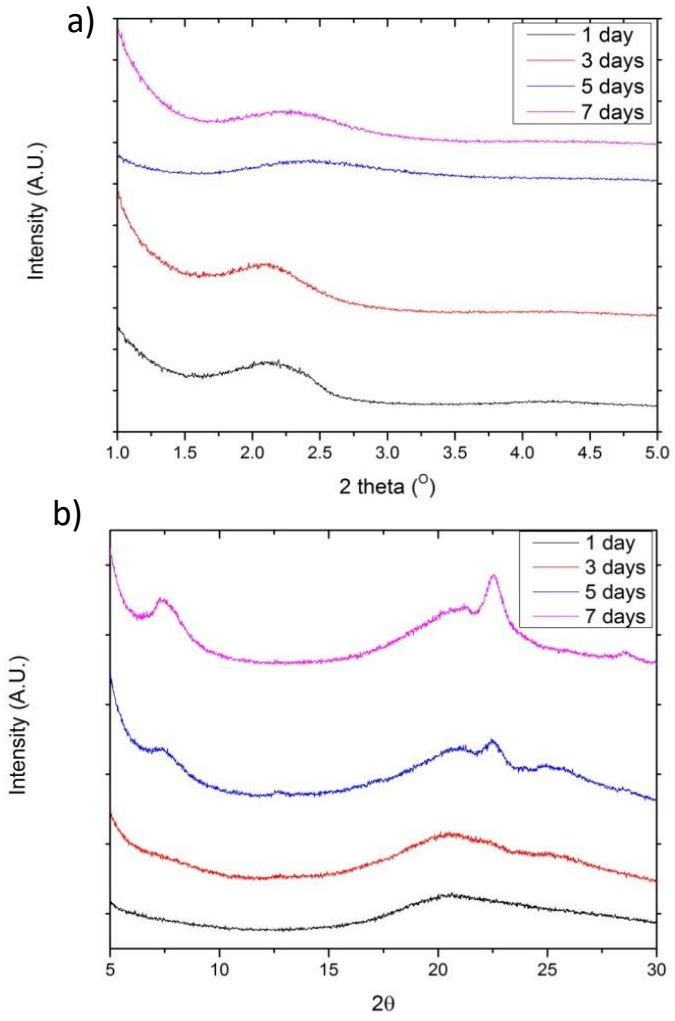

Figure 4.8. a) Low-angle and b) Wide-angle XRD pattern of as-made material with varying durations of hydrothermal treatment.

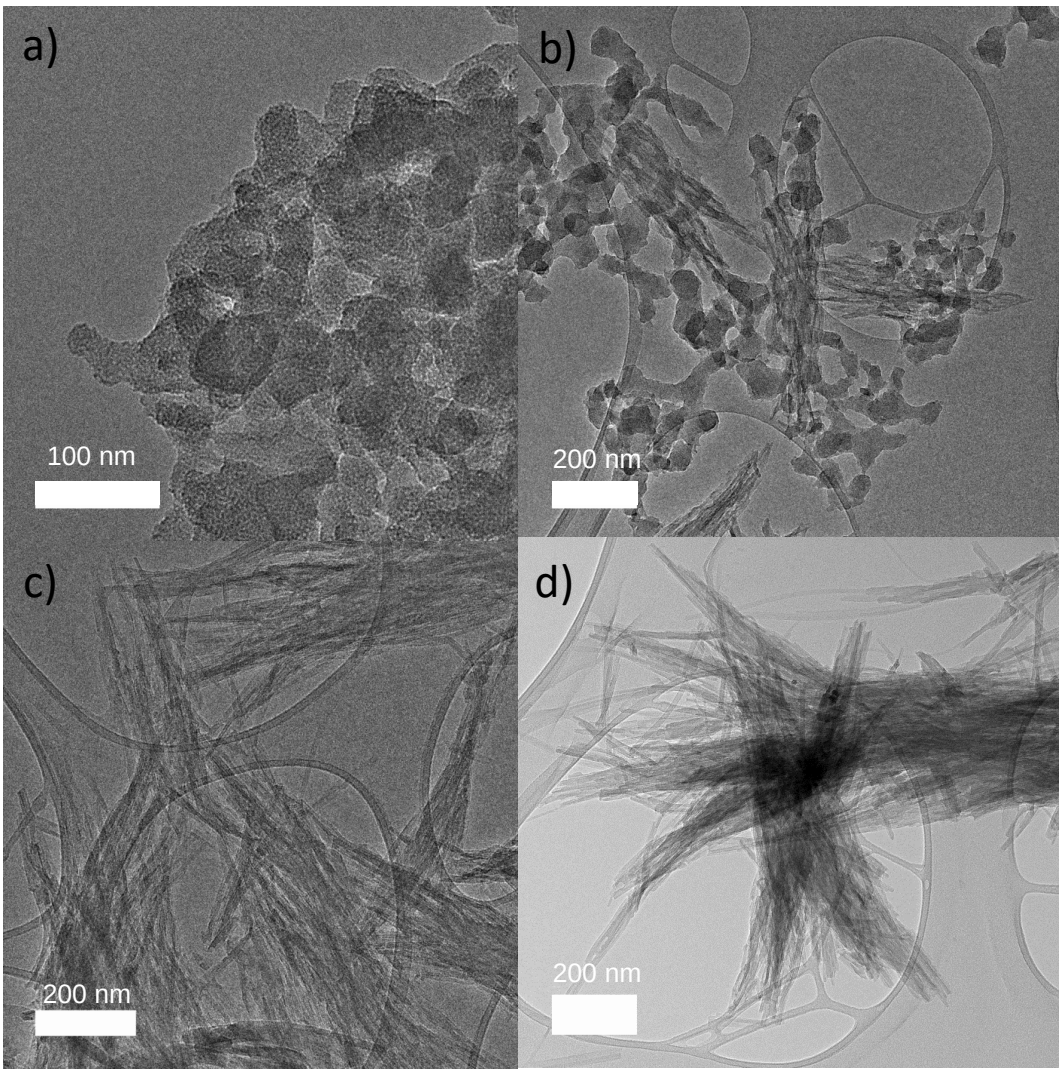

Figure 4.9. TEM images of materials obtained after a) 1 day, b) 3 days, c) 5 days and d) 7 days of hydrothermal growth.

The unique nanotubular morphology of the material reported here can be attributed to the templating action of the bolaform SDA used in this work. Several other bolaform molecules with aromatic rings in the hydrophobic core of the molecule are known to π-stack and form stable cylindrical or rod-like micellar assemblies as observed in TEM and AFM studies.[40] Thus, we hypothesized that the bolaform SDA (BCPh10Qui) used to crystallize the zeolite nanotubes can form a cylindrical or rod-like assembly in solution as

well. The results shown above strongly support this hypothesis and explain the unique nanotube morphology of the material. To study the structure of the SDA embedded in the nanotubes after synthesis, the as-made material was studied by ^{13}C CPMAS NMR and compared to the ^{13}C NMR spectrum of the pure SDA (Figure 4.10). Comparison of the two spectra clearly shows that the SDA is intact in the pores of the nanotubes. This is also confirmed from the elemental analysis of the as-made nanotubes (Table 4.1). The C/N ratio of the as-made nanotubes is ~25, which is close to the C/N ratio of 23 in the SDA. Furthermore, the Si/Al ratio of 15 obtained from Table 4.1 is in agreement that the Si/Al ratio of 16 from NMR spectroscopy as discussed earlier. Based on previous reports of hierarchical zeolite synthesis using SDAs with aromatic rings[12,13,19–21], it can be hypothesized that the SDA self-assembles through a π-π stacking of the aromatic rings. Figure 4.11 shows UV-Vis diffuse reflectance absorption spectra of the as-made nanotubes, the solid SDA, and aqueous SDA solution. In a dilute solution of the SDA in water, where it can be expected that the SDA molecules are isolated from each other, a single absorption peak is observed at 265 nm. In the case of the solid SDA with significant π stacking, the energy for the transition from π-HOMO to π*-LUMO decreases as evident from the red shift in the absorption band to ~314 nm. A similar situation arises in the as-made nanotubes where the absorption band occurs at ~297 nm, indicating significant π-π stacking.

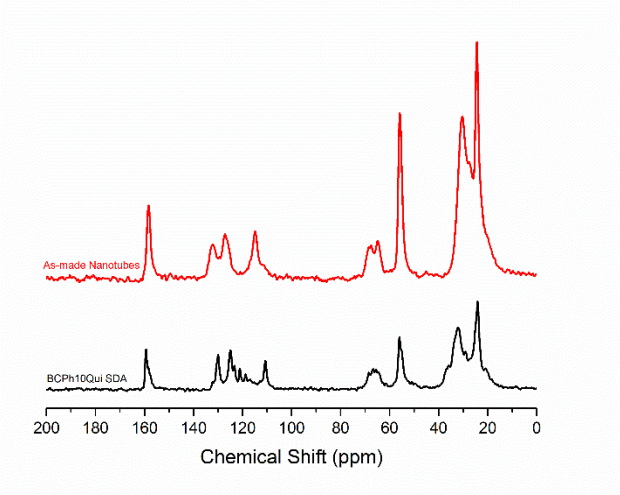

Figure 4.10. ^{13}C CPS MAS NMR spectra of the pure BCPh10Qui SDA (black) and the as-made nanotubes (red)

Table 4.1. Elemental Analysis of the as-made and calcined nanotubes (weight percent)[a]

Sample	Si	Al	Na	C	H	N	O[b]
As-made	19.1	1.29	0.8	39.87	6.12	1.84	30.98
Calcined	38.8	2.63	1.44	-	-	-	57.13

[a]ICP-OES analysis done at Galbraith Laboratories

[b]Determined by attributing the remaining mass to oxygen

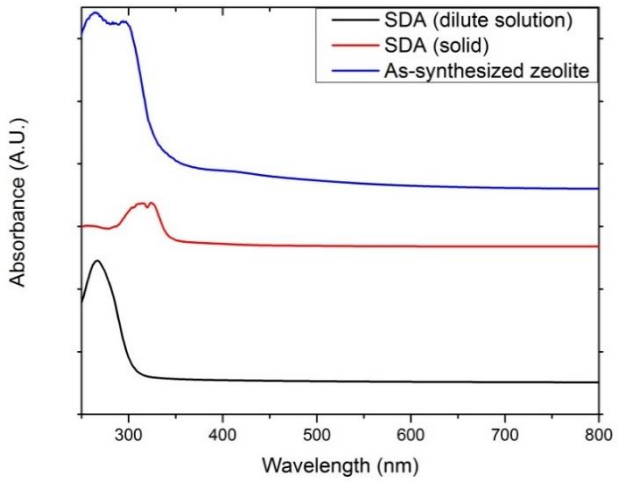

Figure 4.11. UV-Vis spectra of the dilute SDA solution, solid SDA, and as-synthesized nanotubes.

Thermogravimetric analysis of the as-made nanotubes shows that the SDA accounts for 51% of the mass (Figure 4.12), in agreement with elemental analysis (Table 4.1) wherein (C, H, N) make up 48% of the mass of as-made nanotubes. This high organic loading is very typical for several of hierarchical zeolite structures reported in literature.[11,12,20,22] The hydrophobic core of the SDA, which constitutes a significant fraction of its molecular weight, is the main contributor to this high organic loading. This is because the hydrophobic part of the SDA does not really participate in the zeolite framework crystallization and is merely a space-filling portion that helps in the formation of the hierarchical mesopore system. The precise reason for the high organic loading, in terms of the exact arrangement of the SDA molecules, in the as-made nanotubes is not currently understood. However, the formation of a stable cylindrical or rod-like micellar structure would require a specific number of BCPh10Qui molecules to stack, and it may not be necessary for all the molecules to also be involved in templating the microporous zeolitic structure.

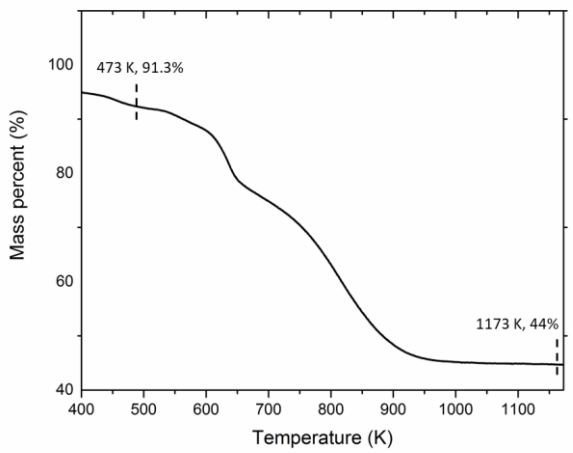

Figure 4.12. TGA mass loss profile with temperature of the as-made nanotubes

Based on these considerations, a preliminary model for arrangement of the SDA molecules in the nanotube is proposed in Figure 4.13. The biphenyl rings of the SDA form a stable hydrophobic core along the axis of the nanotubes, while the flexible alkyl chains with the quinuclidinium groups stretch out along the radius of the nanotube in different directions, reaching out into the microporous walls that are crystallized by the hydrophilic headgroups. However, this proposed arrangement is speculative and obtaining further insights would require rigorous study of the stable SDA conformations in a porous nanotubular structure as well in micellar solutions of the SDA. In addition to the challenge of incorporating suitable interactions for the SDA with the zeolite framework and also with other SDA molecules, proposing an accurate model of the nanotube structure itself requires further high-resolution structure determination by HR-TEM and electron diffraction.

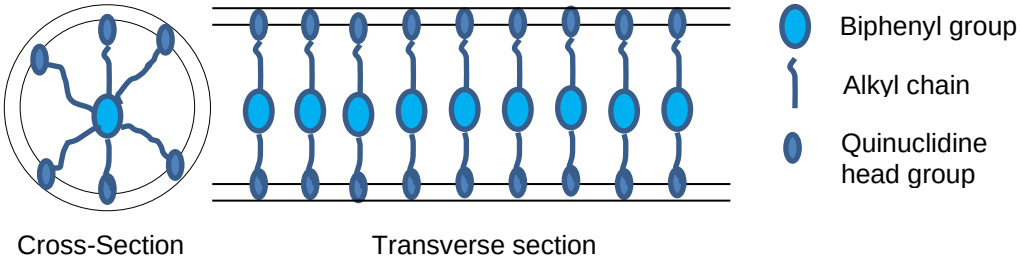

Figure 4.13. Schematic of the templating action by the SDA to crystallize the nanotubes.

4.4 Conclusions

This work is the first demonstration of the crystallization of nanotubes with zeolitic microporous walls. This was achieved using a bolaform SDA that is capable of π-stacking through the biphenyl groups, thus forming a stable, cylindrical/rod-like micellar structure while the quinuclidinium groups in the SDA direct the crystallization of a thin, porous, zeolitic tubular wall that is ~ 1 nm thick. The nanotubes have an inner diameter of ~ 3 nm as determined from TEM and N_2 physisorption while the outer diameter determined from TEM is ~ 5 nm. The nanotube walls appear to be composed of a medium-pore size zeolite structure and likely possesses 5-membered rings based on the FT-IR results. UV-Vis spectroscopy provides evidence for π-stacking of the SDA in the nanotube structure, and a preliminary model for the SDA arrangement was proposed. With the nanotubes possessing micropores and a relatively low Si/Al ratio, they can be useful in catalysis and adsorption related applications. Further studies are being directed at obtaining the detailed structure of the nanotubes and studying the applications of the nanotubes.

4.5 References

(1) Cundy, C. S.; Cox, P. A. The Hydrothermal Synthesis of Zeolites: History and

Development from the Earliest Days to the Present Time. *Chem. Rev.* **2003**, *103* (3), 663–701.

(2) Corma, A. State of the Art and Future Challenges of Zeolites as Catalysts. In *Journal of Catalysis*; 2003.

(3) Davis, M. E. Ordered Porous Materials for Emerging Applications. *Nature* **2002**, *417* (6891), 813–821.

(4) Tao, Y.; Kanoh, H.; Abrams, L.; Kaneko, K. Mesopore-Modified Zeolites: Preparation, Characterization, and Applications. *Chem. Rev.* **2006**, *106* (3), 896–910.

(5) Čejka, J.; Mintova, S. Perspectives of Micro/Mesoporous Composites in Catalysis. *Catal. Rev. - Sci. Eng.* **2007**, *49* (4), 457–509.

(6) Möller, K.; Bein, T. Mesoporosity--a New Dimension for Zeolites. *Chem. Soc. Rev.* **2013**, *42* (9), 3689–3707.

(7) Verboekend, D.; Pérez-Ramírez, J. Design of Hierarchical Zeolite Catalysts by Desilication. *Catal. Sci. Technol.* **2011**, *1* (6), 879–890.

(8) Beyerlein, R. A.; Choi-feng, C.; Hall, J. B.; Huggins, B. J.; Ray, G. J. Effect of Steaming on the Defect Structure and Acid Catalysis of Protonated Zeolites. *Top. Catal.* **1997**, *4*, 27–42.

(9) Feliczak-Guzik, A. Hierarchical Zeolites: Synthesis and Catalytic Properties. *Microporous Mesoporous Mater.* **2018**, *259*, 33–45.

(10) Fan, W.; Snyder, M. A.; Kumar, S.; Lee, P. S.; Yoo, W. C.; McCormick, A. V.; Lee Penn, R.; Stein, A.; Tsapatsis, M. Hierarchical Nanofabrication of Microporous Crystals with Ordered Mesoporosity. *Nat. Mater.* **2008**, *7* (12), 984–991.

(11) Choi, M.; Na, K.; Kim, J.; Sakamoto, Y.; Terasaki, O.; Ryoo, R. Stable Single-Unit-Cell Nanosheets of Zeolite MFI as Active and Long-Lived Catalysts. *Nature* **2009**, *461* (7261), 246–249.

(12) Xu, D.; Ma, Y.; Jing, Z.; Han, L.; Singh, B.; Feng, J.; Shen, X.; Cao, F.; Oleynikov, P.; Sun, H.; Terasaki, O.; Che, S. Π-Π Interaction of Aromatic Groups in Amphiphilic Molecules Directing for Single-Crystalline Mesostructured Zeolite Nanosheets. *Nat. Commun.* **2014**, *5* (May), 4262.

(13) Xu, D.; Jing, Z.; Cao, F.; Sun, H.; Che, S. Surfactants with Aromatic-Group Tail and Single Quaternary Ammonium Head for Directing Single-Crystalline Mesostructured Zeolite Nanosheets. *Chem. Mater.* **2014**, *26* (15), 4612–4619.

(14) Zhang, X.; Liu, D.; Xu, D.; Asahina, S.; Cychosz, K. a.; Agrawal, K. V.; Al Wahedi, Y.; Bhan, a.; Al Hashimi, S.; Terasaki, O.; Thommes, M.; Tsapatsis, M. Synthesis

of Self-Pillared Zeolite Nanosheets by Repetitive Branching. *Science (80-.).* **2012**, *336* (6089), 1684–1687.

(15) Na, K.; Jo, C.; Kim, J.; Cho, K.; Jung, J.; Seo, Y.; Messinger, R. J.; Chmelka, B. F.; Ryoo, R. Directing Zeolite Structures into Hierarchically Nanoporous Architectures. *Science (80-.).* **2011**, *333* (6040), 328–332.

(16) Margarit, V. J.; Mart??nez-Armero, M. E.; Navarro, M. T.; Mart??nez, C.; Corma, A. Direct Dual-Template Synthesis of MWW Zeolite Monolayers. *Angew. Chemie - Int. Ed.* **2015**, *54* (46), 13724–13728.

(17) Serrano, D. P.; Escola, J. M.; Pizarro, P. Synthesis Strategies in the Search for Hierarchical Zeolites. *Chem. Soc. Rev.* **2013**, *42* (9), 4004–4035.

(18) Luo, H. Y.; Michaelis, V. K.; Hodges, S.; Griffin, R. G.; Román-Leshkov, Y. One-Pot Synthesis of MWW Zeolite Nanosheets Using a Rationally Designed Organic Structure-Directing Agent. *Chem. Sci.* **2015**, *6* (11), 6320–6324.

(19) Singh, B. K.; Xu, D.; Han, L.; Ding, J.; Wang, Y.; Che, S. Synthesis of Single-Crystalline Mesoporous ZSM-5 with Three-Dimensional Pores via the Self-Assembly of a Designed Triply Branched Cationic Surfactant. *Chem. Mater.* **2014**, 141203182238007.

(20) Shen, X.; Mao, W.; Ma, Y.; Xu, D.; Wu, P.; Terasaki, O.; Han, L.; Che, S. A Hierarchical MFI Zeolite with a Two-Dimensional Square Mesostructure. *Angew. Chemie - Int. Ed.* **2018**, *57* (3), 724–728.

(21) Zhang, Y.; Shen, X.; Gong, Z.; Han, L.; Sun, H.; Che, S. Single-Crystalline MFI Zeolite with Sheet-Like Mesopores Layered along the a Axis. *Chem. - A Eur. J.* **2019**, *25* (3), 738–742.

(22) Zhang, Y.; Ma, Y.; Che, S. Synthesis of Lamellar Mesostructured ZSM-48 Nanosheets. *Chem. Mater.* **2018**, *30* (6), 1839–1843.

(23) Zhang, Y.; Che, S. π–π Interactions Between Aromatic Groups in Amphiphilic Molecules: Directing Hierarchical Growth of Porous Zeolites. *Angew. Chemie - Int. Ed.* **2020**, *59* (1), 50–60.

(24) Seo, Y.; Lee, S.; Jo, C.; Ryoo, R. Microporous Aluminophosphate Nanosheets and Their Nanomorphic Zeolite Analogues Tailored by Hierarchical Structure-Directing Amines. *J. Am. Chem. Soc.* **2013**, *135* (24), 8806–8809.

(25) Ravikovitch, P. I.; O'Domhnaill, S. C.; Neimark, A. V.; Schiith, F.; Unger, K. K. Capillary Hysteresis in Nanopores: Theoretical and Experimental Studies of Nitrogen Adsorption on MCM-41. *Langmuir* **1995**, *11* (12), 4765–4772.

(26) Kang, D. Y.; Brunelli, N. A.; Yucelen, G. I.; Venkatasubramanian, A.; Zang, J.; Leisen, J.; Hesketh, P. J.; Jones, C. W.; Nair, S. Direct Synthesis of Single-Walled

Aminoaluminosilicate Nanotubes with Enhanced Molecular Adsorption Selectivity. *Nat. Commun.* **2014**, *5*.

(27) Kang, D. Y.; Zang, J.; Wright, E. R.; McCanna, A. L.; Jones, C. W.; Nair, S. Dehydration, Dehydroxylation, and Rehydroxylation of Single - Walled Aluminosilicate Nanotubes. *ACS Nano* **2010**, *4* (8), 4897–4907.

(28) http://www.iza-structure.org/databases/.

(29) Pophale, R.; Cheeseman, P. A.; Deem, M. W. A Database of New Zeolite-like Materials. *Phys. Chem. Chem. Phys.* **2011**, *13* (27), 12407–12412.

(30) Knio, O.; Medford, A. J.; Nair, S.; Sholl, D. S. Database of Computation-Ready 2D Zeolitic Slabs. *Chem. Mater.* **2019**, *31* (2), 353–364.

(31) Jansen, J. C.; van der Gaag, F. J.; van Bekkum, H. Identification of ZSM-Type and Other 5-Ring Containing Zeolites by i.r. Spectroscopy. *Zeolites* **1984**, *4* (4), 369–372.

(32) Coudurier, G.; Naccache, C.; Vedrine, J. C. Uses of I.R.Spectroscopy in Identifying ZSM Zeolite Structures. *J. Chem. Soc., Chem. Commun.* **1982**, No. 24, 1413–1415.

(33) Jacobs, P. A.; Beyer, H. K.; Valyon, J. Properties of the End Members in the Pentasil-Family of Zeolites: Characterization as Adsorbents. *Zeolites* **1981**, *1* (3), 161–168.

(34) Lesthaeghe, D.; Vansteenkiste, P.; Verstraelen, T.; Ghysels, A.; Kirschhock, C. E. A.; Martens, J. A.; Van Speybroeck, V.; Waroquier, M. MFI Fingerprint: How Pentasil-Induced IR Bands Shift during Zeolite Nanogrowth. *J. Phys. Chem. C* **2008**, *112* (25), 9186–9191.

(35) Tomlinson, S. R.; McGown, T.; Schlup, J. R.; Anthony, J. L. Infrared Spectroscopic Characterization of CIT-6 and a Family of *BEA Zeolites. *Int. J. Spectrosc.* **2013**, *2013*, 1–7.

(36) Klinowski, J.; Ramdas, S.; Thomas, J. M.; Fyfe, C. A.; Hartman, J. S. A Re-Examination of Si, Al Ordering in Zeolites NaX and NaY. *J. Chem. Soc. Faraday Trans. 2 Mol. Chem. Phys.* **1982**, *78* (7), 1025–1050.

(37) Zhang, H.; Xiao, Q.; Guo, X.; Li, N.; Kumar, P.; Rangnekar, N.; Jeon, Y.; Al-thabaiti, S.; Narasimharao, K.; Basahel, S. N.; Topuz, B.; Onorato, F. J.; Macosko, C. W.; Mkhoyan, K. A.; Tsapatsis, M. Open-Pore Two-Dimensional MFI Zeolite Nanosheets for the Fabri- Cation of Hydrocarbon-Isomer-Selective Membranes on Porous Poly- Mer Supports. **2016**, 1–5.

(38) Schmidt, J. E.; Xie, D.; Davis, M. E. Synthesis of the RTH-Type Layer: The First Small-Pore, Two Dimensional Layered Zeolite Precursor. *Chem. Sci.* **2015**, *6* (10), 5955–5963.

(39) Na, K.; Chol, M.; Park, W.; Sakamoto, Y.; Terasakl, O.; Ryoo, R. Pillared MFI Zeolite Nanosheets of a Single-Unit-Cell Thickness. *J. Am. Chem. Soc.* **2010**, *132* (12), 4169–4177.

(40) Wang, C.; Wang, Z.; Zhang, X. Amphiphilic Building Blocks for Self-Assembly: From Amphiphiles to Supra-Amphiphiles. *Acc. Chem. Res.* **2012**, *45* (4), 608–618.

CHAPTER 5. SUMMARY AND FUTURE WORK

A chapter wise summary of the dissertation is presented below followed by possible future directions.

5.1 Summary

5.1.1 Chapter 1

Zeolite nanosheets offer an alternative to improve the performance of conventional zeolites for both catalysis and membrane separation applications. The high external surface area of the nanosheets exposes a large fraction of the active sites and this allows for a higher catalytic activity as compared to conventional zeolite catalysts for conversion of bulky reactants. Similarly, the single unit-cell thickness can be exploited for the fabrication of ultra-thin membranes that display enhanced permeation flux because of the short diffusion length through the crystal, while maintaining selectivity. Therefore, it is important to further explore the fundamental aspects and enhancement in performance that can be obtained with these zeolite nanosheets in catalysis and membrane separation applications. For catalysis, we chose to study the effect of the Si/Al ratio on the catalytic activity of 2D MFI nanosheets using Friedel-Crafts alkylation of mesitylene with benzyl alcohol as a model reaction. In case of membrane separations, AEL nanosheets were chosen because of their limiting pore size of 4 Å, for fabricating a composite membrane with poly(amide) on α-alumina hollow fibers to study their performance for desalination of water. Lastly, given the exceptional performance enhancements obtained with 2D zeolite nanosheets, it was

determined that extending their synthesis methodology to lower dimensional microporous materials would of fundamental research interest as well.

5.1.2 Chapter 2

2D MFI nanosheet catalysts with varying Si/Al ratio were synthesized by control of synthesis conditions. Based on several morphological and textural characterizations, it was concluded that the acid site density was the sole property that varied between these catalysts. Use of these catalysts in the Friedel-Crafts alkylation of mesitylene with benzyl alcohol showed that the turnover frequency (TOF) decreased with decreasing Si/Al ratio as expected. Deconvoluting the TOF for the alkylation and self-etherification showed that the self-etherification reaction was mainly responsible for the trend of overall TOF decreasing with decreasing Si/Al ratio. Carrying out the same reaction by poisoning the external acid sites with DTBP (2,6 – di-*tert*-butylpyridine) completely stopped the alkylation reaction and only the self-etherification of benzyl alcohol proceeded in the micropores of the 2D MFI catalysts. This allowed for the calculation of the effectiveness factor, which decreased with decreasing Si/Al ratio, demonstrating that some internal mass transfer limitations were responsible for the observed catalytic activity trend and it was only the self-etherification reaction that could be affected by this, since the alkylation cannot occur in the micropores. This study enables a fundamental understanding of the effect of Si/Al ratio on the catalytic activity of 2D MFI nanosheets.

5.1.3 Chapter 3

Exfoliation of multilamellar AEL nanosheets was carried out using polymer melt blending with poly(styrene) in a twin-screw extruder. The exfoliated AEL nanosheets were

then coated on the shell side of α-alumina hollow fibers. This coating smoothed the surface of the alumina hollow fiber and formed a uniform coating that was 300-350 nm thick. A poly(amide) (PA) film was then formed via interfacial polymerization of *m*-phenylenediamine (MPD) in water and trimesoyl chloride (TMC) in hexane. This poly(amide) film partially encapsulated the AEL nanosheets, while mostly growing over the film, with the composite membrane being less than 550 nm thick. The AEL nanosheet/PA composite membrane demonstrated a high water flux and salt rejection, along with long-term stability for 150 h of testing in the pervaporative desalination of brackish water. The membrane was also effective in the pervaporative desalination of seawater. This work was the first demonstration of the successful exfoliation of AEL nanosheets and using them to smoothen the surface of alumina hollow fibers to form a PA membrane on it. Thus, it provides a strong motivation to study the use of zeolite nanosheets for fabricating scalable and high flux PA membranes for desalination..

5.1.4 Chapter 4

A bolaform OSDA with quinuclidinum groups was used to direct the crystallization of an aluminosilicate nanotube with microporous zeolitic walls. Based on previous studies on the micellar assembly of similar organic molecules, it was hypothesized that the OSDA could form a cylindrical/rod-like micellar structure due to the π-stacking of the aromatic rings, which templated the mesopore of the nanotube. On the other hand, the quinuclidinium groups was hypothesized to direct the crystallization of the microporous walls of the nanotubes. The nanotube had an outer diameter of 5 nm with an inner mesopore of 3 nm. The micropore size was 5 Å, which closely resembles that of a 10 member-ring zeolite framework. The morphology, textural characteristics and bonding environment of

the atoms were studied in detail through several techniques. Through our collaboration with Dr. Tom Willhammar and Dr. Xiaodong Zou at Stockholm University, the microporous zeolitic material comprising the walls of the nanotube was determined to have the *BEA framework. This is the first instance of the crystallization of a microporous zeolitic nanotube, to the best of our knowledge. These zeolite nanotubes can have potential applications in catalysis as well as separations due to their unique morphology with the presence of micropores along the radial direction and a high external surface area.

5.2 Future Work

5.2.1 Rigorous optimization of membrane fabrication parameters for the AEL nanosheet/PA composite membranes

In chapter 3, the development and performance of AEL nanosheet/PA composite membranes on α-alumina hollow fibers for pervaporative desalination of water was demonstrated. This was mainly a proof-of-concept study and the coating thickness of the AEL nanosheet as well as the parameters of the interfacial polymerization reaction were not optimized. The thickness of the intermediate AEL nanosheet layer can affect the permeation flux as well as characteristics of the poly(amide) layer since it acts as a reservoir for the diamine molecules and ensures their controlled release. On the other hand, the interfacial polymerization process and the performance of the PA membrane is known to be affected by the monomers used and their concentrations, the solvents used to dissolve the monomers, the dip-coating durations, the curing temperature and duration as well as post-treatment activation methods.[1,2] With several of these factors affecting the performance of the PA membrane in tandem, there are ample opportunities to fine-tune the

PA film structure in conjunction with an optimal AEL nanosheet coating thickness. A rigorous parametric study is thus important to further improve the performance of the composite membrane. Furthermore, PA membranes have also been applied to other separations including the dehydration of alcohols. Hence, it is also worthwhile to test the performance of the AEL nanosheet/PA composite membranes for this separation.

5.2.2 Use of other zeolite nanosheets as the smoothing layer on α-alumina hollow fibers for fabricating composite poly(amide) membranes

Chapter 3 demonstrated a proof-of-concept PA membrane on the shell side of alumina hollow fibers with a AEL nanosheet intermediate layer. The central idea of this work was to fabricate the PA membranes on scalable alumina hollow fibers and this necessitated the use of a smoothing layer, as reported in previous works.[3–5] At the same time, the use of intermediate layers between the support and the PA film is known to drastically enhance the permeance while maintaining solute rejections.[6–9] AEL nanosheets were chosen to form a coating on the hollow fiber and serve the dual purpose of smoothing the fiber surface while acting as an intermediate layer and releasing the diamine molecules in a controlled manner during the interfacial polymerization.

However, the idea of exfoliating the multilamellar AEL nanosheets was inspired from a similar process carried out on MFI nanosheets.[10] It has been reported in literature that pure silica as well as aluminosilicate MFI membranes have demonstrated successful desalination of water with high salt rejections and water flux.[11] Additionally, zeolite membranes made using directly synthesized aluminosilicate MFI nanosheets have shown exceptional stability for highly concentrated salt solutions, along with high water flux and

salt rejections.[12] Thus, exploring the use of exfoliated MFI nanosheets as a smoothing and intermediate layer on alumina hollow fibers for fabricating PA membranes is warranted. While the exfoliation of multilamellar MFI nanosheets has only been reported for the pure silicate form, extending this process to aluminosilicates and using them for the PA composite membrane fabrication would also ensure improvement in hydrophilicity of the resultant membrane. This could have potential implications in enhancing the pure water flux of the membrane. However, the interaction and adhesion of the PA film on the MFI nanosheet intermediate layer would be an important consideration in the fabrication of these membranes.

5.2.3 Scale-up of AEL nanosheet/PA composite membranes

Scale-up of the membrane fabrication process would encompass 2 aspects –

- Increasing the length of the composite hollow fiber membrane.
- Increasing the number of composite hollow fiber membranes tested in a single module.

The AEL nanosheet/PA composite membranes described in this work were fabricated on α-alumina hollow fibers that were 9 cm in length, and they were ultimately mounted in a module that reduced their length to 5 cm. Theoretically, both of the major steps involved in the membrane fabrication process – coating of the AEL nanosheets and interfacial polymerization reaction – are scalable to hollow fiber supports that are longer in length. On a longer hollow fiber support, the desired AEL nanosheet coating thickness can be obtained by scaling up the volume of the exfoliated nanosheet suspension that needs to be filtered through the support, whereas the interfacial polymerization reaction is merely

dependent on the duration of reaction and is not affected by the length of the hollow fiber. Making a defect-free multi-fiber membrane module, on the other hand, would rely on the reproducibility of the membrane fabrication process. The data presented in chapter 3 were gathered from 3 independently made membrane samples. However, a rigorous analysis of the success rate of making defect-free membranes was not carried out and would be important in this regard.

5.2.4 Spatial arrangement of the OSDA during the crystallization of zeolite nanotubes

To the best of our knowledge, there have been no prior reports of a nanotube morphology for a microporous zeolitic material. The newly reported *BEA microporous material was crystallized using a bolaform OSDA with quinuclidinium groups on the ends. While there is evidence of π-stacking of the amphiphilic OSDA based on UV-Vis spectroscopy and an arrangement for the OSDA molecules, as proposed in chapter 4, the precise arrangement of the OSDA in the mesopore of the nanotube and its templating configuration remains unresolved. To support the hypothesized OSDA arrangement, further work is needed. Rigorous characterization based on a combination of 2D NMR, HR-TEM, electron diffraction and electron difference maps along with simulations of the XRD pattern for the uncalcined nanotube with the OSDA arranged in different combinations, could potentially aid in uncovering the arrangement of the OSDA.[13,14] This would help in designing new OSDA that can help to tune the dimensions or framework of the zeolite nanotube.

5.2.5 Zeolite nanotubes as a support for aminopolymers – application to CO_2 capture

Solid supported amine sorbents are advantageous for CO_2 capture from air and flue gas because of their low heat capacities and ease of regeneration.[15,16] Mesoporous silica supports such as SBA-15 and MCM-41, impregnated with aminopolymers such as poly(ethyleneimine) (PEI), have been widely studied in this regard. These aminopolymers are physically impregnated into the mesopores of the silica support via wet impregnation and have relatively weak, non-covalent interactions with the support. Both SBA-15 and MCM-41 have long, cylindrical mesopores that are approximately 3-10 nm in diameter. The walls of the supports are not highly porous and the primary way for the CO_2 molecules to adsorb onto the PEI molecules impregnated in the support pores is to diffuse through the pore openings on either end of the support particle. In this regard, the zeolite nanotubes reported in chapter 5 could potentially be used as a support for impregnating PEI and used for CO_2 capture. The central hypothesis is that the zeolite nanotubes present an advantage over conventional silica supports with regards to enhancing diffusion because of the presence of a multitude of micropores on the nanotube walls. Instead of having to diffuse through mesopore openings on the particle ends as would be the case for conventional silica supports, CO_2 molecules can diffuse through the radial micropores on the nanotube walls and it is hypothesized that this would lead to enhancements in diffusion kinetics, amine efficiency and CO_2 capture capacity. The exact nature of the enhancement would need to be studied via detailed comparisons of amine loadings, CO_2 concentrations and mesopore size of the support.

5.2.6 Zeolite nanotubes for catalysis applications

Hierarchical zeolites with single unit-cell crystal thickness have shown exceptional catalytic activities as compared to conventional zeolites.[17–19] The aluminosilicate zeolite nanotubes reported in chapter 5 can also act as catalysts because they possess a low Si/Al and thus can be ion-exchanged to create a high density of acid-sites. The high external surface area and thin walls of the nanotube would also improve diffusion limitations and thus the zeolite nanotubes can be expected to show high catalytic activity as well. This needs to be studied in greater detail with several test reactions.

Pt nanoparticles supported on MFI nanosheets showed high conversion and selectivity towards branched isomers in the hydroisomerization of n-heptane.[20] Along similar lines, the mesopore of the nanotube can be impregnated with Pt metal nanoparticles and the composite material can be used as hydroisomerization catalyst for linear alkanes. The hypothesis is that the radial micropores on the nanotube walls would facilitate the diffusion of the linear alkane molecules, which would then be isomerized by the Pt nanoparticles impregnated in the central mesopore. The isomerized products would have side chains and this would result in an increase in their kinetic diameter. Thus, in certain cases, these molecules would not diffuse out through the radial micropores and instead will diffuse out through the central mesopore. Hence, each nanotube can act as a unidirectional reactor with reactant molecules diffusing in through the radial micropores and product molecules diffusing out through the central mesopore. A similar reaction process, but in the opposite direction, can be hypothesized for a depolymerization reaction if the zeolite nanotubes are applied to these reactions.

5.3 References

(1) Gohil, J. M.; Ray, P. A Review on Semi-Aromatic Polyamide TFC Membranes Prepared by Interfacial Polymerization: Potential for Water Treatment and Desalination. *Sep. Purif. Technol.* **2017**, *181*, 159–182.

(2) Liu, F.; Wang, L.; Li, D.; Liu, Q.; Deng, B. A Review: The Effect of the Microporous Support during Interfacial Polymerization on the Morphology and Performances of a Thin Film Composite Membrane for Liquid Purification. *RSC Adv.* **2019**, *9* (61), 35417–35428.

(3) Maaskant, E.; Wit, P. De; Benes, N. E. Direct Interfacial Polymerization onto Thin Ceramic Hollow Fi Bers. *J. Membr. Sci.* **2018**, *550* (January), 296–301.

(4) Li, Y. X.; Cao, Y.; Wang, M.; Xu, Z. L.; Zhang, H. Z.; Liu, X. W.; Li, Z. Novel High-Flux Polyamide/TiO2 Composite Nanofiltration Membranes on Ceramic Hollow Fibre Substrates. *J. Membr. Sci.* **2018**, *565* (November 2017), 322–330.

(5) Liu, X.; Cao, Y.; Li, Y.; Xu, Z.; Li, Z.; Wang, M.; Ma, X. High-Performance Polyamide / Ceramic Hollow Fiber TFC Membranes with TiO2 Interlayer for Pervaporation Dehydration of Isopropanol Solution. *J. Membr. Sci.* **2019**, *576* (January), 26–35.

(6) Karan, S.; Jiang, Z.; Livingston, A. G. Sub-10 Nm Polyamide Nanofilms with Ultrafast Solvent Transport for Molecular Separation. *Science (80-.).* **2015**, *348* (6241), 1347–1351.

(7) Gong, G.; Wang, P.; Zhou, Z.; Hu, Y. New Insights into the Role of an Interlayer for the Fabrication of Highly Selective and Permeable Thin-Film Composite Nanofiltration Membrane. *ACS Appl. Mater. Interfaces* **2019**, *11* (7), 7349–7356.

(8) Zhang, Z.; Shi, X.; Wang, R.; Xiao, A.; Wang, Y. Ultra-Permeable Polyamide Membranes Harvested by Covalent Organic Framework Nanofiber Scaffolds: A Two-in-One Strategy. *Chem. Sci.* **2019**, *10* (39), 9077–9083.

(9) Wang, Z.; Wang, Z.; Lin, S.; Jin, H.; Gao, S.; Zhu, Y.; Jin, J. Nanoparticle-Templated Nanofiltration Membranes for Ultrahigh Performance Desalination. *Nat. Commun.* **2018**, *9* (1).

(10) Kumar Varoon,* Xueyi Zhang,* Bahman Elyassi, Damien D. Brewer, M. G.; Sandeep Kumar,‡ J. Alex Lee,§ Sudeep Maheshwari,‖ Anudha Mittal, C.-Y. S.; Matteo Cococcioni, Lorraine F. Francis, Alon V. McCormick, K. Andre Mkhoyan, M. T. Dispersible Exfoliated Zeolite Nanosheets and Their Application as a Selective Membrane. *Science (80-.).* **2011**, *734* (October), 72–76.

(11) Wang, Q.; Li, N.; Bolto, B.; Hoang, M.; Xie, Z. Desalination by Pervaporation: A Review. *Desalination* **2016**, *387*, 46–60.

(12) Cao, Z.; Zeng, S.; Xu, Z.; Arvanitis, A.; Yang, S.; Gu, X.; Dong, J. Ultrathin ZSM-5 Zeolite Nanosheet Laminated Membrane for High-Flux Desalination of Concentrated Brines. *Sci. Adv.* **2018**, *4* (11), 1–11.

(13) Messinger, R. J.; Na, K.; Seo, Y.; Ryoo, R.; Chmelka, B. F. Co-Development of Crystalline and Mesoscopic Order in Mesostructured Zeolite Nanosheets. *Angew. Chemie - Int. Ed.* **2015**, *54* (3), 927–931.

(14) Mccusker, L. B.; Baerlocher, C. 4.6. Zeolites. In *International Tables for Crystallography*; 2019; pp 452–464.

(15) Sanz-Pérez, E. S.; Murdock, C. R.; Didas, S. A.; Jones, C. W. Direct Capture of CO2 from Ambient Air. *Chem. Rev.* **2016**, *116* (19), 11840–11876.

(16) Didas, S. A.; Choi, S.; Chaikittisilp, W.; Jones, C. W. Amine-Oxide Hybrid Materials for CO2 Capture from Ambient Air. *Acc. Chem. Res.* **2015**, *48* (10), 2680–2687.

(17) Na, K.; Jo, C.; Kim, J.; Cho, K.; Jung, J.; Seo, Y.; Messinger, R. J.; Chmelka, B. F.; Ryoo, R. Directing Zeolite Structures into Hierarchically Nanoporous Architectures. *Science (80-.).* **2011**, *333* (6040), 328–332.

(18) Choi, M.; Na, K.; Kim, J.; Sakamoto, Y.; Terasaki, O.; Ryoo, R. Stable Single-Unit-Cell Nanosheets of Zeolite MFI as Active and Long-Lived Catalysts. *Nature* **2009**, *461* (7261), 246–249.

(19) Zhang, X.; Liu, D.; Xu, D.; Asahina, S.; Cychosz, K. a.; Agrawal, K. V.; Al Wahedi, Y.; Bhan, a.; Al Hashimi, S.; Terasaki, O.; Thommes, M.; Tsapatsis, M. Synthesis of Self-Pillared Zeolite Nanosheets by Repetitive Branching. *Science (80-.).* **2012**, *336* (6089), 1684–1687.

(20) Kim, J. C.; Kim, W.; Seo, Y.; Kim, J. C.; Ryoo, R.; Verheyen, E.; Jo, C.; Kurttepeli, M.; Vanbutsele, G.; Gobechiya, E.; Kor??nyi, T. I.; Bals, S.; Van Tendeloo, G.; Ryoo, R.; Kirschhock, C. E. A.; Martens, J. A. N-Heptane Hydroisomerization over Pt/MFI Zeolite Nanosheets: Effects of Zeolite Crystal Thickness and Platinum Location. *J. Catal.* **2013**, *300*, 70–80.

APPENDIX A. SUPPORTING INFORMATION FOR CHAPTER 2

Table A.1. Screening conditions of the 2D MFI synthesis

Screen	Si/Al	Na/Si	ROH/Si	SDA/(Si+Al)	H_2O/Si	H_2SO_4/Si	Time (days)	Temp. (K)	pH	Products
1	1	1.5	1.5	0.05	80.00	0	5	373	11.7	LTA
2	5	0.90	0.90	0.08	80.00	0	15	423	11.2	Amorphous
3	5	1.20	1.20	0.08	80.00	0	15	423	11.9	2D layered MFI overgrown on GIS/ANA
4	5	2.40	2.40	0.08	80.00	0	5	423	13.2	ANA
5	10	0.60	0.60	0.09	80.00	0	15	423	11	Amorphous
6	10	1.20	1.20	0.09	80.00	0	15	423	11.8	ANA
7	15	0.60	0.60	0.09	80.00	18	5	423	-	Amorphous
8	15	0.60	0.60	0.09	80.00	12	5	423	8.8	Amorphous
9	15	0.60	0.60	0.09	80.00	12	12	423	8.8	Amorphous
10	15	0.60	0.60	0.09	80.00	0	5	423	11.2	Amorphous
11	15	0.60	0.60	0.09	80.00	0	12	423	11.5	MFI nanocrystals
12	15	0.60	0.60	0.09	80.00	0	12	433	11.6	MFI nanocrystals
13	15	0.60	0.60	0.09	80.00	6	12	423	10.8	2D Layered MFI
14	15	0.60	0.60	0.09	40.00	0	12	423	11.3	2D Layered-3D MFI hybrid
15	25	0.60	0.60	0.10	80.00	18	5	423	-	Partially amorphous, 2D layered MFI
16	25	0.60	0.60	0.10	80.00	12	12	423	10.5	2D layered MFI
17	25	0.60	0.60	0.10	40.00	6	12	423	11.3	2D Layered-3D MFI hybrid
18	50	0.60	0.60	0.10	80.00	18	5	423	10.0	2D layered MFI
19	100	0.60	0.60	0.10	80.00	18	5	423	10.5	2D layered MFI
20	151	0.60	0.60	0.10	80.00	18	5	423	10.8	2D layered MFI

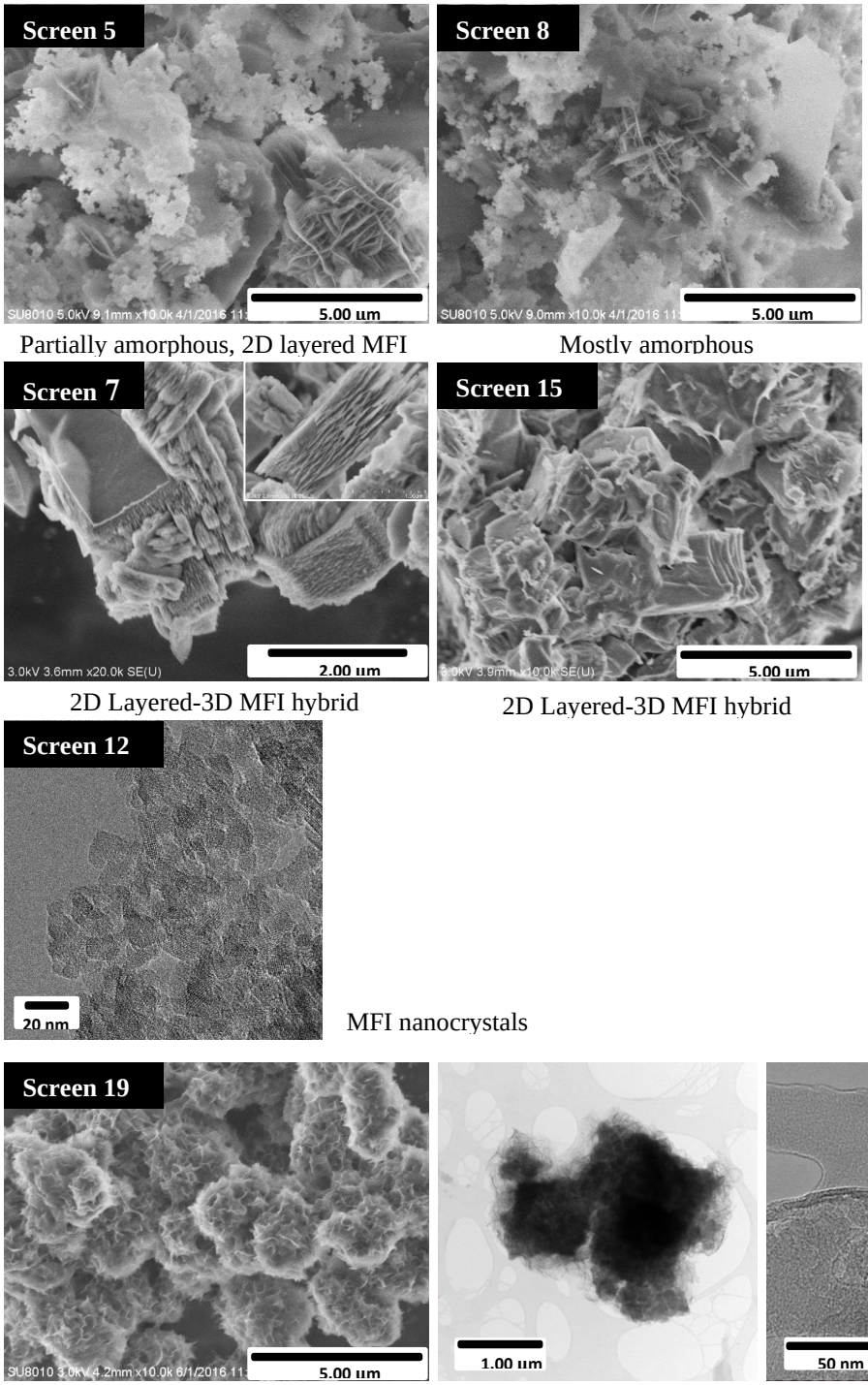

Figure A.1. SEM and TEM images of the products resulting from different synthesis conditions.

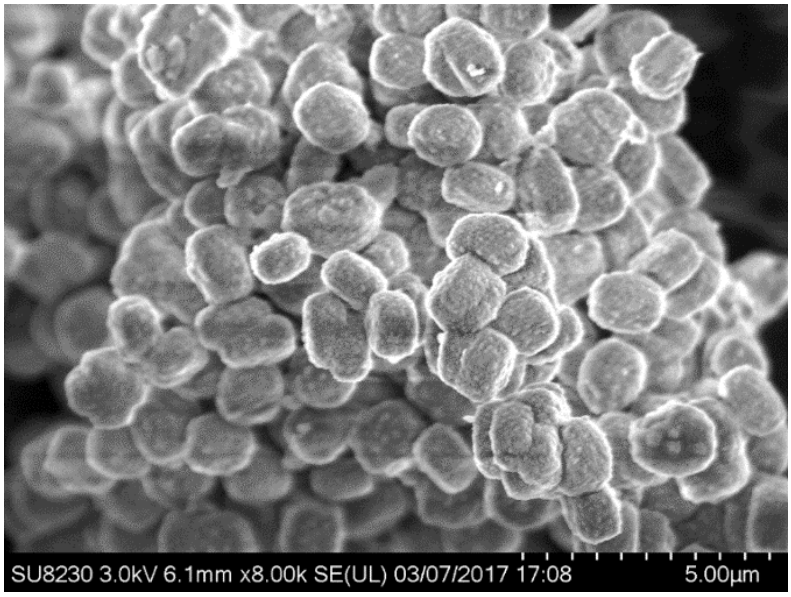

Figure A.2. SEM image of 3D MFI (21).

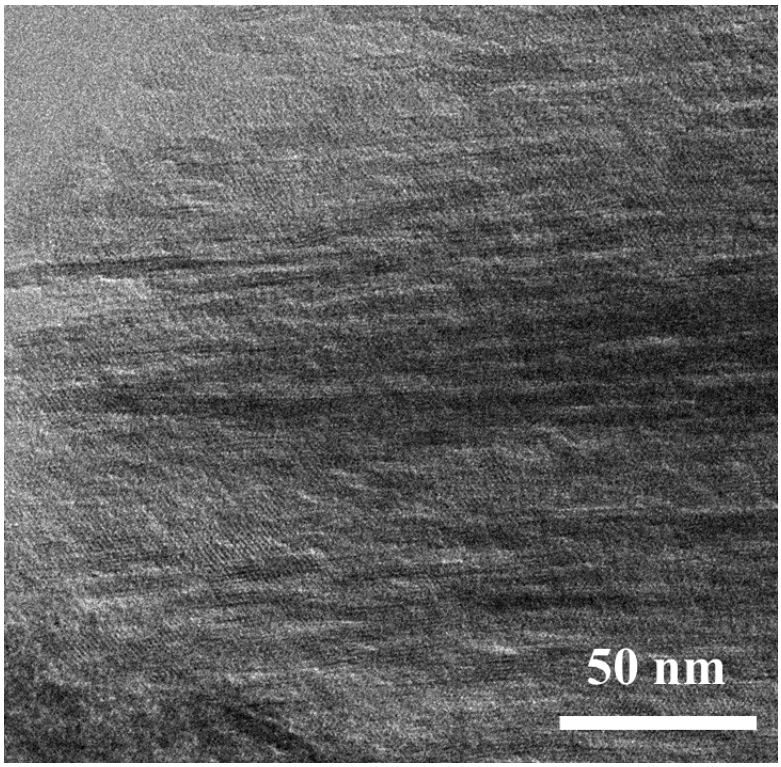

Figure A.3. HRTEM image of the 2D MFI after calcination, showing that interlayer mesopore spaces (brighter area between the 2D MFI nanosheets) are intact.

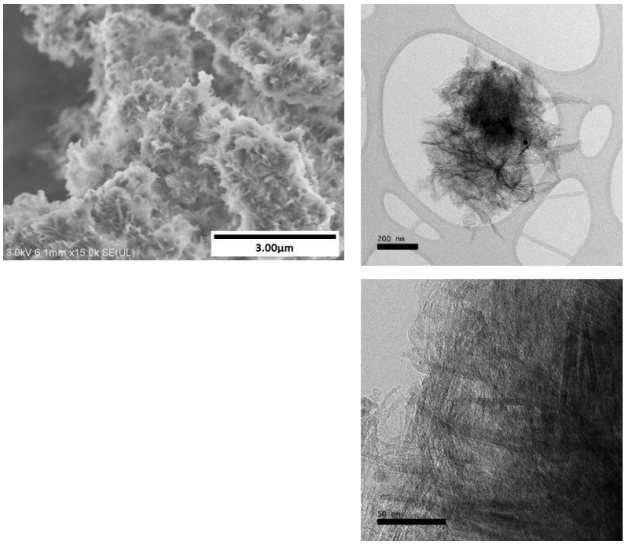

Si/Al	16
S_{BET}[a] (m^2/g)	463
S_{micro} (m^2/g)	175
S_{ext} (m^2/g)	288
V_{micro}[b] (cm^3/g)	0.07
V_{total}[c] (cm^3/g)	0.38
V_{meso}[d] (cm^3/g)	0.31
V_{meso}/V_{total}	0.82
S_{ext}/S_{BET}	0.622

[a]Determined from BET method, [b]Determined from t-plot method, [c]Determined from absorbed volume at P/P_0=0.97, [d]Determined by V_{total}-V_{micro}

Figure A.4. SEM and TEM images, along with textural properties measured by N2 physisorption, of 2D MFI (16).

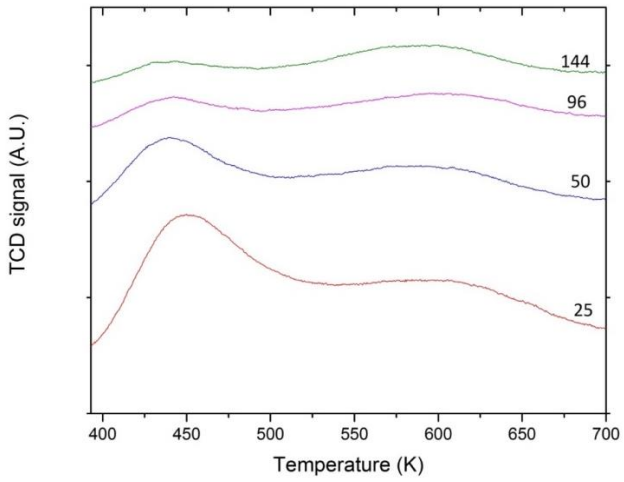

Figure A.5. NH3 TPD profiles for each of the 2D MFI catalysts.

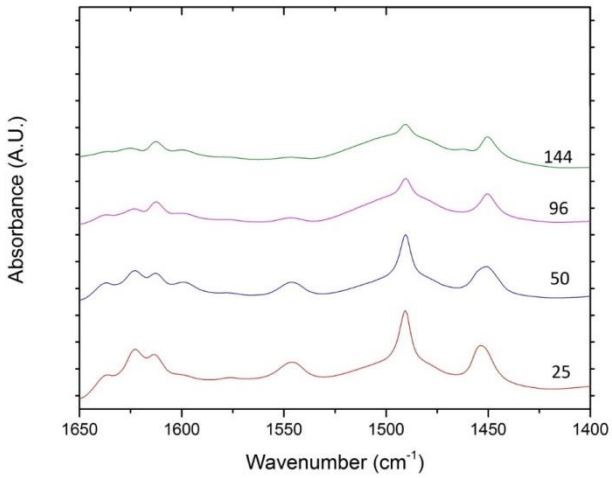

Figure A.6. FTIR spectra of adsorbed pyridine for each of the 2D MFI catalysts.

Table A.2. Selectivity to dibenzyl ether during the catalytic conversion of benzyl alcohol in mesitylene.

Si/Al ratio	Selectivity to DBE[a]
25	0.45
50	0.45
96	0.42
144	0.36

[a]Calculated as a ratio of moles of DBE formed to the total moles of benzyl alcohol consumed

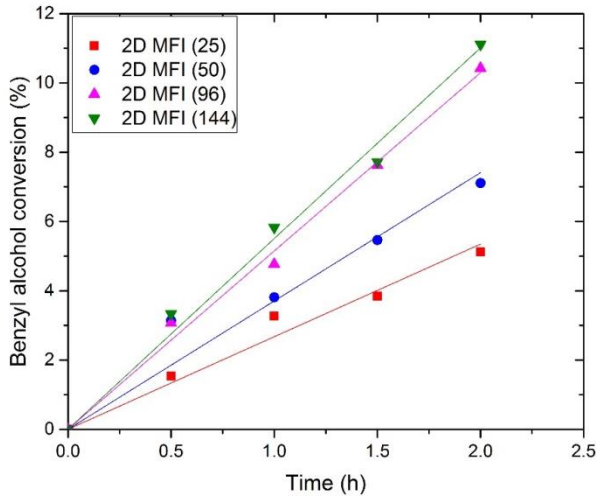

Figure A.7. Conversion of benzyl alcohol as a function of time for Friedel-Crafts alkylation of benzene with benzyl alcohol & self-etherification of benzyl alcohol carried out over 2D MFI (n) catalysts.

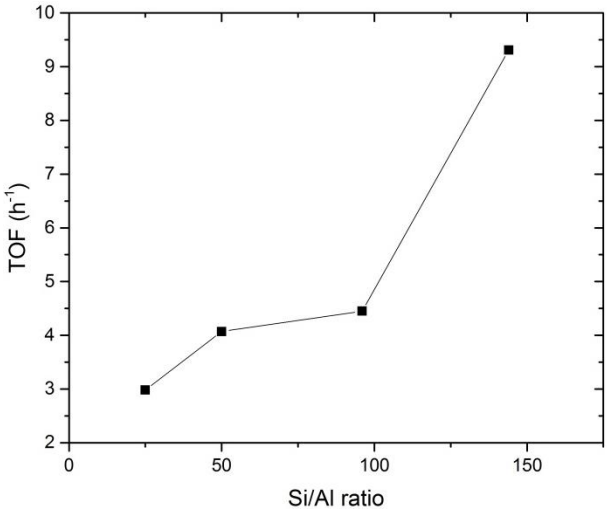

Figure A.8. TOF for the combined Friedel-Crafts alkylation of benzene with benzyl alcohol & self-etherification of benzyl alcohol.

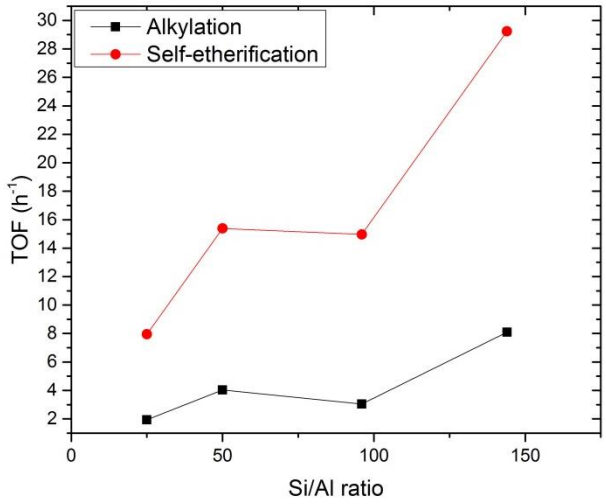

Figure A.9. TOF for the alkylation and self-etherification reactions in benzene for the 2D MFI (n) catalysts with different Si/Al ratios (n = 25, 50, 96, 144).

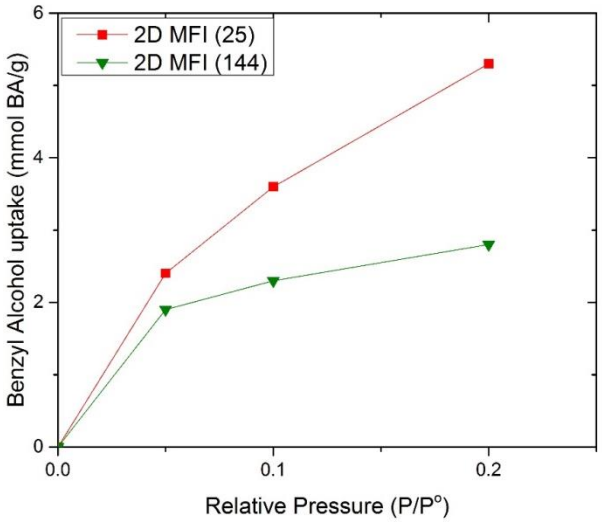

Figure A.10. Benzyl alcohol adsorption isotherms for the extreme Si/Al ratio catalysts

A.1 Effectiveness Factor for self-etherification of benzyl alcohol

The effectiveness factor for the self-etherification of benzyl alcohol was calculated using the same model as reported by Zhang et al.[1] The rate of self-etherification of benzyl alcohol when the 2D MFI nanosheet catalyst is poisoned with DTBP is assumed to be

proportional to the adsorbed benzyl alcohol and the Brønsted acid site concentration inside the micropores. At steady state, the diffusion of and reaction of benzyl alcohol can be described using the following differential equation -

$$D_A \frac{d^2 \bar{C}_A}{dx^2} - k_{eth} C_{H^+} \bar{C}_A = 0 \quad \text{(A.1)}$$

Where $\bar{C}_A$ (mol L^{-1}) is the concentration of benzyl alcohol adsorbed on the catalyst, C_{H^+} ([mol H^+] L^{-1}) is the concentration of Brønsted acid sites in the catalyst, D_A is the effective diffusivity of benzyl alcohol in the catalyst (m^2 s^{-1}) and k_{eth} ([mol H^+] L s^{-1}) is the second order rate constant for the self-etherification of benzyl alcohol.

The 2 boundary conditions used to solve the above differential equation are –

1) On the external surface of the catalyst, $x = x_P, \bar{C}_A = \bar{C}_{AS}$ &
2) At the center of catalyst particle, $x = 0, \frac{d\bar{C}_A}{dx} = 0$

The concentration profile of benzyl alcohol after solving the differential equations with the boundary conditions is expressed as

$$\bar{C}_A = \frac{\bar{C}_{AS}}{\cosh \varphi} \cosh\left(\varphi \frac{x}{x_P}\right) \quad \text{(A.2)}$$

where φ is the Thiele modulus. Assuming a quasi-steady reaction-diffusion model,

$$\frac{S_{cat}}{V_{sol}} D_A \left.\frac{d\bar{C}_A}{dx}\right|_{x = x_P} = -\frac{dC_A}{dt} \quad \text{(A.3)}$$

Where S_{cat} and V_{sol} are the total external surface area of the catalyst and the total volume of the solution respectively. The concentration of benzyl alcohol on the catalyst surface is approximated by a Langmuir isotherm as reported by Zhang et al.[1]

$$\bar{C}_{AS} = \frac{KC_A}{1 + KC_A}\bar{C}_A^{max} \tag{A.4}$$

Integrating the reaction-diffusion model by substituting for the Langmuir isotherm,

$$\frac{V_{sol}}{C_{H^+}V_{cat}}\left[ln\frac{C_A^o}{C_A} + K(C_A^o - C_A)\right] = k_{eth,app}K\bar{C}_A^{max}t \tag{A.5}$$

Here, the apparent rate constant for etherification is defined as $k_{eth,app} = \eta k_{eth}$ where η is the effectiveness factor. Zhang et al.(ref) reported the value of k_{eth} = 1.11 x 10^{-3} [mol H^+] L s^{-1} and D_A = 6.15 x 10^{-20} m^2s^{-1}. Based on the $k_{eth,app}$ obtained from the conversion vs. time profile, the effectiveness factor was calculated for each catalyst.

A.2 References

(1) Zhang, X.; Liu, D.; Xu, D.; Asahina, S.; Cychosz, K. a.; Agrawal, K. V.; Al Wahedi, Y.; Bhan, a.; Al Hashimi, S.; Terasaki, O.; Thommes, M.; Tsapatsis, M. Synthesis of Self-Pillared Zeolite Nanosheets by Repetitive Branching. *Science (80-.).* **2012**, *336* (6089), 1684–1687.

APPENDIX B. SUPPORTING INFORMATION FOR CHAPTER 3

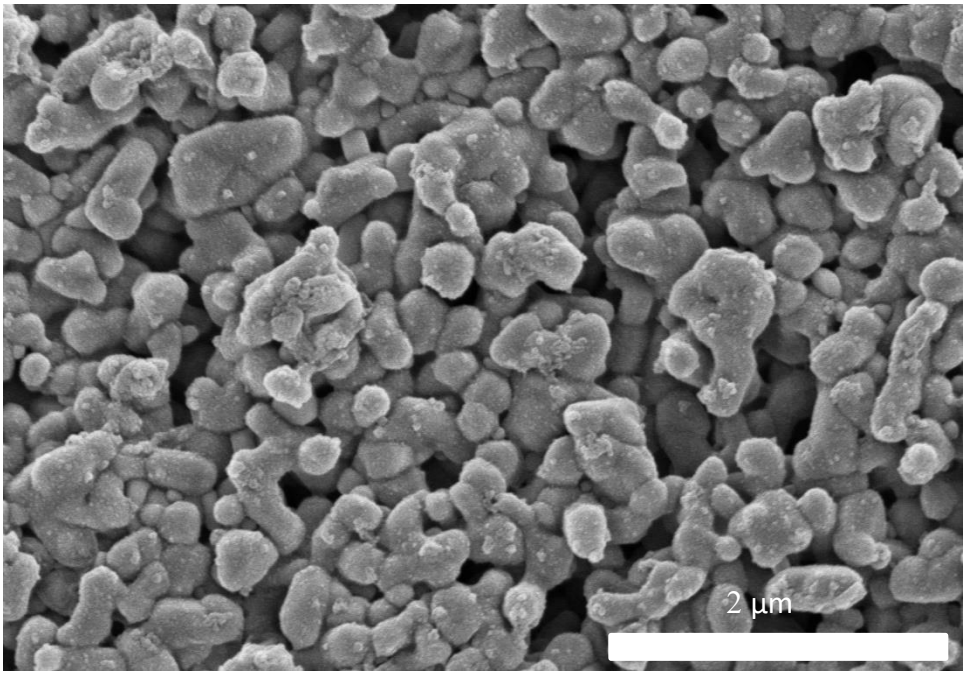

Figure B.1. SEM image of the alumina hollow fiber surface after interfacial polymerization without the AEL zeolite nanosheet coating.

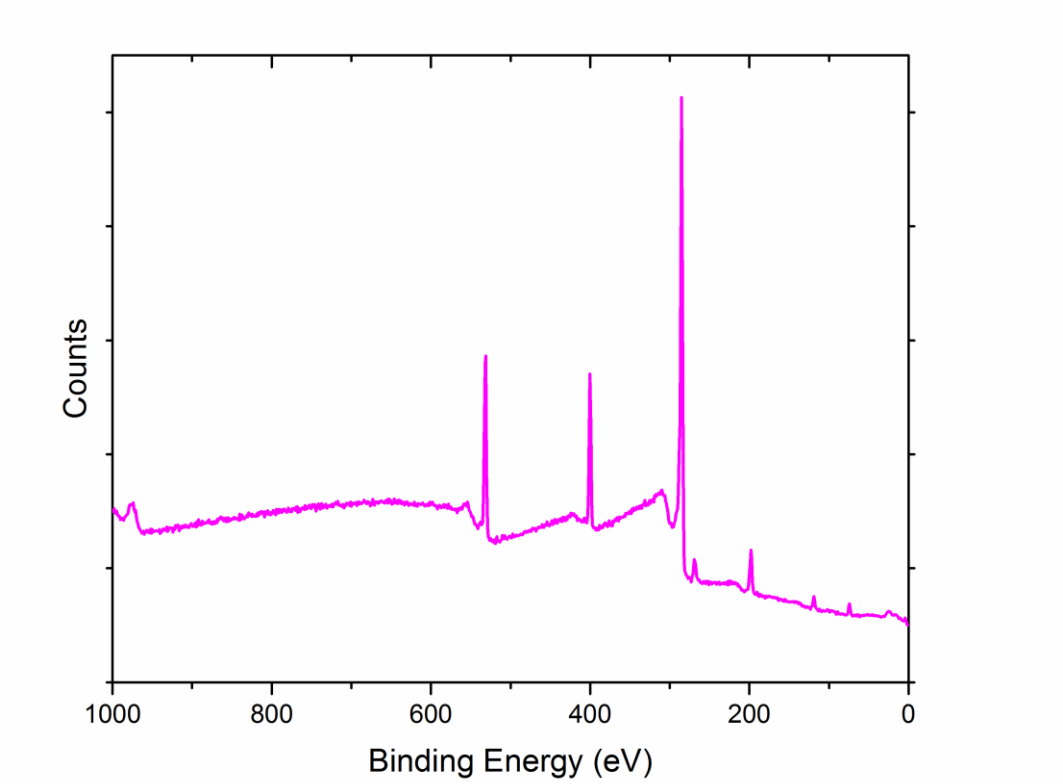

Figure B.2. XPS spectrum of the sample formed with the interfacial polymerization carried out on a bare alumina hollow fiber.

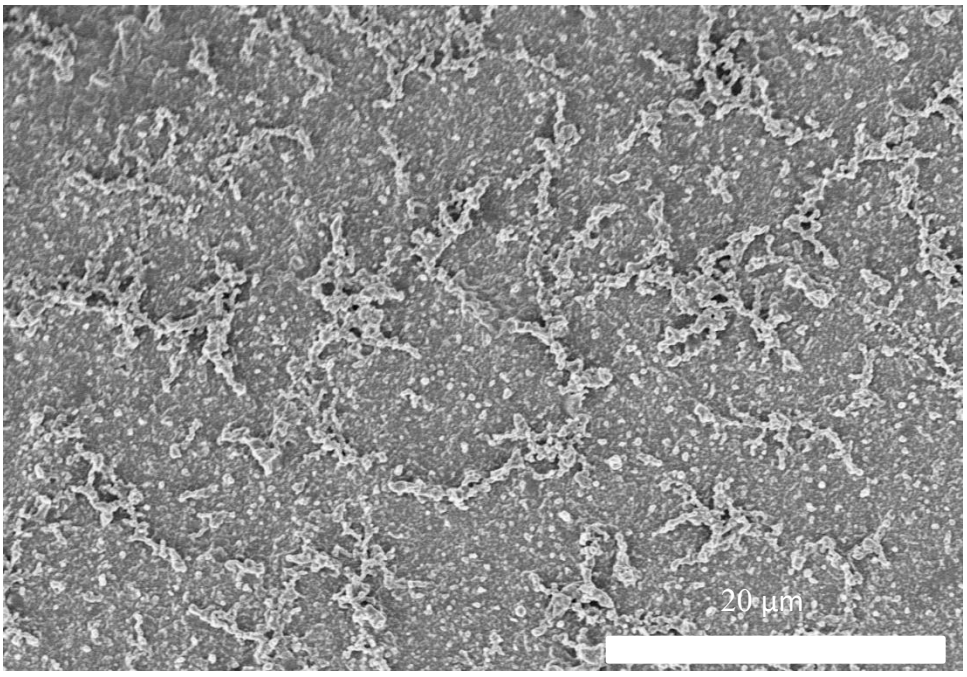

Figure B.3. SEM image of the surface of AEL nanosheet/PA composite membrane

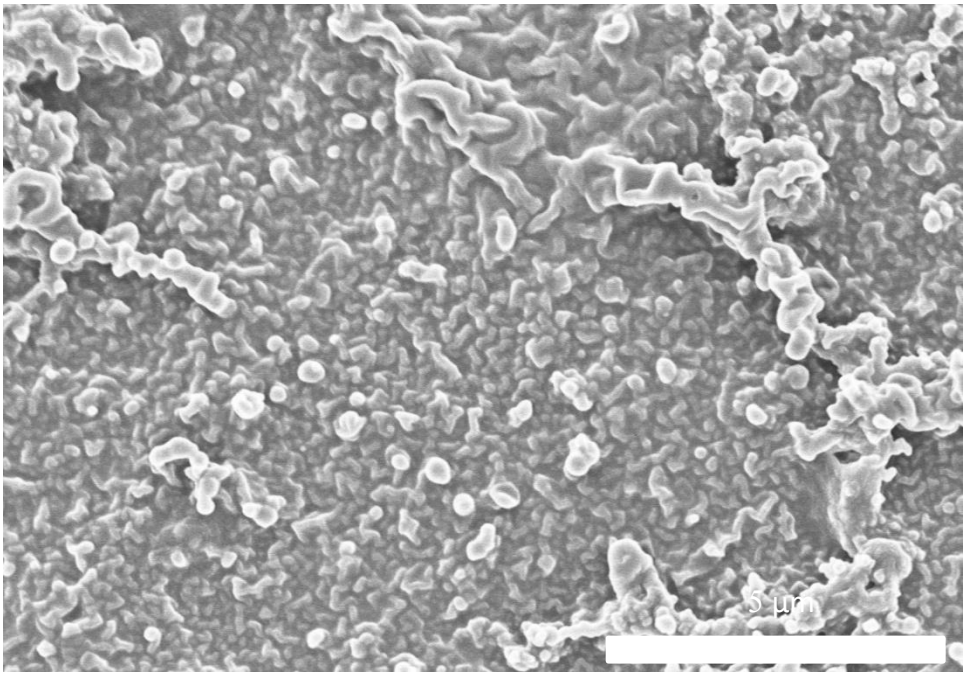

Figure B.4. SEM image of the surface of AEL nanosheet/PA composite membrane